2009

Studies of states and state transitions in low mass X-ray binaries

Charles Bradley
Louisiana State University and Agricultural and Mechanical College, cbrad11@lsu.edu

STUDIES OF STATES AND STATE TRANSITIONS IN LOW MASS X-RAY BINARIES

A Dissertation

Submitted to the Graduate Faculty of the
Louisiana State University and
Agricultural and Mechanical College
in partial fulfillment of the
requirements for the degree of
Doctor of Philosophy

in

The Department of Physics and Astronomy

by
Charles Bradley
B.S., Clemson University, 2003
M.S., Lousiana State University, 2008
August, 2009

Dedication

For my grandfather...

Acknowledgements

I would like to thank my two thesis advisors, Juhan Frank and Robert Hynes, for their wonderful support and patience on days where I sometimes forgot how to think properly. I would also like to thank Joel Tohline for probing questions at each stage of the final project that went into this thesis.

I would like to thank my colleagues, in particular Wes Even, Robert Beaird, and Jay Call, without whom my time as a graduate student would have been quite difficult, and I may not be here today. I would also like to thank faculty members Brad Schaeffer, Geoff Clayton and Arlo Landolt.

I would also like to thank my professors with whom I had the privilege of working before I came to LSU. In particular, Mark Leising of Clemson University, who tolerated my insistence on working with accretion physics instead of his own preference for nuclear astrophysics.

I would like to thank my closest friends in this world, Jodi Stepp and Kevin Patton, whose encouragement and counsel have kept me sane during my years at LSU. I would like to thank my mother, who drove me to become a better person and without whom I could not function. Finally, I would like to thank my grandfather, Charles Pridgeon, who introduced me to science fiction as a little boy, and started me on the path that led here. I wish he could be and my grandmother could be here in person to see me finish, but I know they are watching from Heaven above.

Table of Contents

List of Tables

List of Figures

Abstract

We investigate the model of a disk/coronal accretion flow into a black hole. We build a numerical code to ascertain whether the inner regions of an accretion disk in X-ray binaries can transform from a cool standard disk to an advection-dominated flow through the known properties of Coulomb interaction in a two-temperature plasma, taking into account viscous heating, standard radiation processes, and thermal conduction. A hot, diffuse corona covering the whole disk is powered by accretion, but it exchanges energy with the underlying cool disk through radiative interactions and conduction. If the accretion rate is low enough, at some intermediate radius the corona begins to evaporate the cool disk away, leaving an advective coronal flow to continue towards the hole as consistent with X-ray observations that I have studied using *XMM-Newton* and *Chandra*. We show that if the accretion rate increases sufficiently, complete evaporation does not occur and the cool inner disk remains, proceeding inward to the innermost stable orbit. During spectral transitions an intermediate state has been observed whose nature is unclear, but which shows the presence of cold matter near an X-ray emitting source, along with an additional component that could come from an advective coronal flow. We build a steady-state model that includes these effects and mass exchange between the two flows through evaporation and recondensation during the soft/hard transition and create a "hysteresis" similar to that observed, along with representative spectra for each X-ray state.

1. Introduction

The extraction of gravitational potential energy from material which falls onto the surface of another gravitational body (a star or black hole) is called accretion. It is now believed to be the prime source of energy powering some of the most energetic sources in the Universe such as Active Galactic Nuclei (AGN) and quasars. This material is heated by viscous friction and releases energy in the form of radiation, which our telescopes can see, as it falls inwards down the gravitational potential of the object of interest.

However, the realization of accretion as an important power source was first made in the context of quasars (Zeldovich & Novikov 1964) which approach the Eddington limit, a theoretical limit to the rate at which matter can be accreted (see Ch. 4, Section 1). Quasars and AGN harbor supermassive black holes that have masses over a million times the mass of our Sun. Only later was accretion theory applied to binary systems. These systems make up a majority of all star systems in our galaxy, and since many will, at some stage, undergo some type of accretion event, they are a prime subject of research.

There are several types of binary systems. The intuitive one that comes to mind is simply two stars revolving around their center of mass, called a *detached* system. *Semi-detached* systems are those that undergo Roche lobe overflow (see following section), where generally one star fills a region of gravitational influence, called a Roche lobe, and can transfer matter to a companion star. In the case of study in this dissertation, it involves one star that no longer undergoes core hydrogen burning, and its outer layers expand to fill its Roche lobe. Systems known as Algol binaries are one possible exception, where the stars approach one another through loss of angular momentum over their lifetimes. Orbital periods for these two types can range from hours to years. The third type is called a *contact* binary, in which the surfaces of both stars are touching, with orbital periods of a few hours, called W UMa systems (after the first system identified).

Detailed studies of the interactions of binary systems show the importance of the concept of angular momentum in accretion. Since each star is spinning on its own axis, and also making revolutions about the center of mass of the system, the material on the surface of each star will have some angular momentum. In general, there are two types of accretion in these binary systems that will be introduced here: Roche lobe overflow and stellar wind accretion. The second case is thought to be the primary form for High-Mass X-ray Binaries (HMXBs, where 'high-mass' refers to the star thats donating mass, that will have a mass higher than the Sun) but is less understood. The first applies directly to the systems of interest in this dissertation and so more time will be spent discussing those.

Many accreting binaries are discovered in wavebands other than optical (the wavelengths our eyes can see). Since the launch of X-ray telescopes, many more have been discovered while in outburst. Some go through a multitude of emission states, with their luminosity and/or spectral properties changing very rapidly and drastically. As one would expect then, their lightcurves are highly variable, but we do not know why these transitions occur or why they are so variable. The focus of this thesis is to study the spectral states and state transitions in X-ray binaries and to build a model of accretion that applies to the transition from a thermally-dominated X-ray spectrum to a hard spectrum, and give us insight into their variability as well.

1.1 Types of Accretion

From now on, I will refer to the star that is losing mass (the donor) as the secondary, M_2, and the star onto which the material accretes (the accretor) as the primary, M_1. Generally the primary star is a white dwarf, neutron star, or black hole. However the secondary can be anything, with possibilities ranging from stars far older and smaller than our Sun to stars ten to twenty times its mass and at any stage of evolution. The process of mass transfer will change the binary's mass ratio, $q = M_2/M_1$ throughout the lifetime of the system, and this

ratio is a key parameter in understanding the physics that occurs in these systems, which will be elaborated on in the forthcoming sections and chapters.

1.1.1 Stellar Wind Accretion

All stars, including the Sun, have a persistent outflow from their surface, which consists of charged protons and electrons that become unbound through various processes on the surface. However, some stars have outer layers that are easily ejected in this wind loss, and some could even lose a significant fraction of their mass. At some stage of evolution, they may even lose more mass than at others. The exact amount a star will lose in its lifetime is a continuing subject of research, but the primary contributing factors are its surface temperature, surface gravity, magnetic field instabilities, and the wind outflow could be driven by emission lines of heavy elements.

If the star is in a binary system, this wind outflow could fall into the potential well of the other star and be accreted (Blondin et al. 1990). This is usually the case for HMXB systems, where the primary is a neutron star or black hole. Cyg X-1 is probably the best known example of a HMXB, which harbors a black hole roughly ten times the mass of the Sun.

Accretion in the stellar wind case usually occurs because the donor star is generally a young, massive star with an intense stellar wind whose velocity ($\sim$ 1000 km/s) exceeds the local sound speed ($\sim$ 10 km/s). The accretor is typically a neutron star or black hole. Since the gas flow relative to a neutron star is so highly supersonic, we can treat the flow as a collection of test particles. In that case, any particles which pass close enough to the secondary so that their kinetic energy is less than their gravitational potential energy will get captured and accreted. However, because the flow is supersonic, a bow shock will form around the critical radius where this energy imbalance occurs. Of most concern in current research is how much of this wind ultimately gets captured, and whether it has enough angular momentum to form an accretion disk.

If we neglect completely the orbital motion of the primary, the accreted momentum would be zero by symmetry. However, since the primary itself rotates and revolves around its companion, there is some angular momentum in the wind. Still, the specific angular momentum is so low that the accretion disk is expected to be much smaller and the chances of its initial formation are much lower in this case.

For parameters typical of X-ray binaries, accretion rates are estimated to be a thousandth of the wind-loss rate from the secondary, making this form of accretion very inefficient compared to Roche Lobe overflow (where most of the mass is accreted), so it is only because the wind-loss rates are so extreme that we can observe these systems.

1.1.2 Roche Lobe Overflow

Inevitably the more massive star in a binary system will begin to evolve off the main sequence before its companion does. As it ages, it will begin to swell up in size, and will eventually reach the point where the pull of the other star will be able to strip off the outer layers and pull them onto itself. This type of system is called semi-detached (see, e.g., Patterson 1984). Also, if angular momentum is lost from the system through gravitational radiation, or stellar wind mass loss (as pointed out previously, all stars have an outflow from their surface to varying degrees), the distance between the two stars may decrease, making it even easier for the other star to strip off material. The best way to study this is through a three-body problem.

The three-body problem was first studied by French mathematician Edouard Roche, in the context of planets and moons, and is now associated with his name. The restricted three-body problem is as follows: we take two massive, centrally-condensed, stars orbiting about one another and a small test particle which is assumed to have a mass so negligible as to not disturb the motions of the two stars. These two stars will then execute simple Keplerian orbits in a plane, assumed to be circular. These assumptions turn out to be pretty good, as tidal effects act to make the orbits circular over the lifetime of the system, although

there are cases where this is not true (see Frank, King & Raine 2002). We then have an energy configuration like Fig. 1.1. These two stars are assumed to execute orbits according

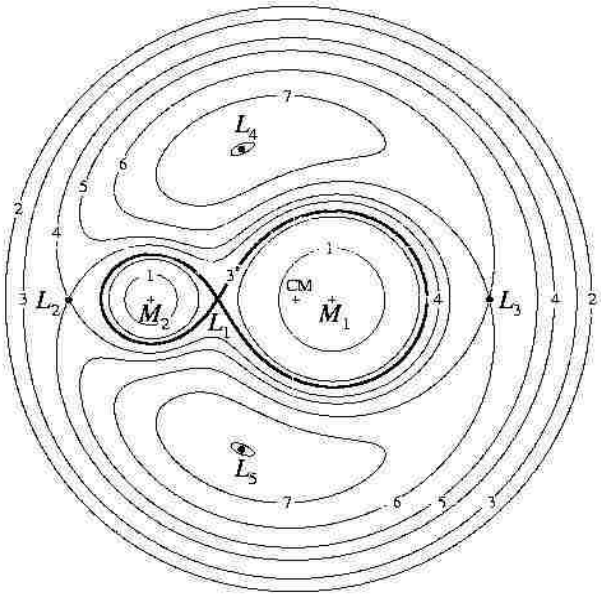

Figure 1.1: Roche problem, the points are numbered in order of increasing energy. M_1 is the more massive star, and this picture is drawn for a system with q=0.25. Drawn on this plot are equipotential surfaces, also numbered with increasing energy, with the Roche lobe surface in bold. L_4 and L_5 are local maxima of the potential. Figure reproduced from Frank, King, & Raine 2002, provided by Juhan Frank.

to Kepler's law:

$$4\pi^2 a^3 = GMP_{\rm orb}^2 \tag{1.1}$$

where a is the distance between the two stars, G is Newton's gravitational constant, M is the sum of the masses of both stars, and the orbital period $P_{\rm orb}$ is the time the binary takes for one orbit.

Around each star is a potential well, or area of gravitational influence, where material can be easily captured. The shape of this is shown in Figs. 1.1-1.2. Around each star is a critical surface, called the Roche lobe, which demarcates this area of greatest gravitational influence. The lobes of the two stars join at the inner Lagrange point, L_1, a saddle point in

the potential (Fig. 1.2), where material can easily pass from one star to the next due to it being an unstable equilibrium point.

The mathematical formulation of the Roche potential is the following:

$$\Phi_R(r) = -\frac{GM_1}{\mid r - r_1 \mid} - \frac{GM_2}{\mid r - r_2 \mid} - \frac{1}{2}\Omega^2 r^2 \tag{1.2}$$

where r_1, r_2 are the position vectors of the centers of the two stars, and Ω is the angular velocity relative to an inertial frame. Note that the Coriolis force is not included in this scalar function, and it is the presence of this force that makes the points L_4 and L_5 stable equilibrium positions in Fig. 1.1. Now, suppose that one star begins to swell up for some

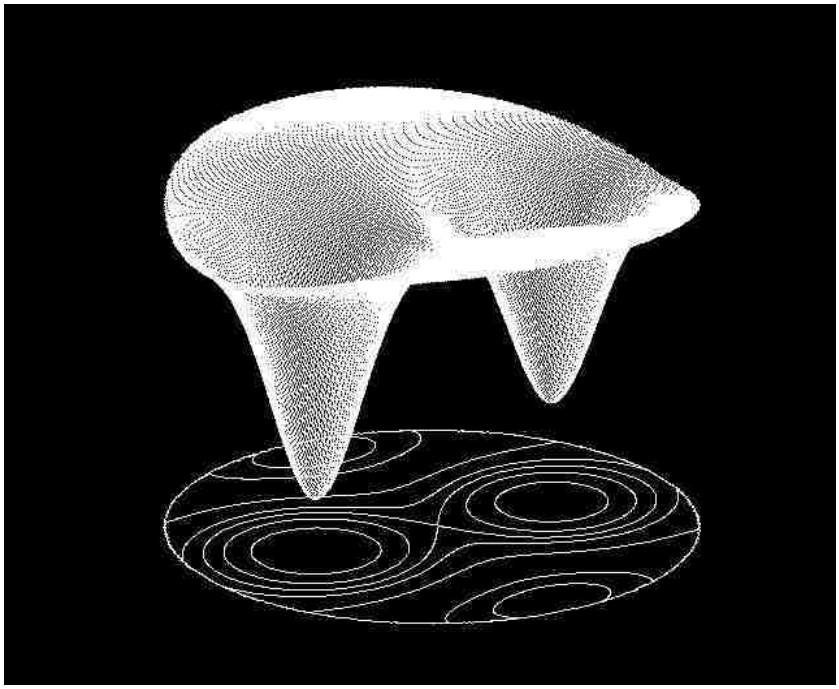

Figure 1.2: Schematic of potential surfaces, the larger pit is around the more massive star. Figure provided by P. Motl.

reason, and that it swells up to the point where its surface coincides with its Roche lobe surface (since the surface of a body must lie on an equipotential). Any perturbation, from things like pressure forces, will cause the material to fall through the inner Lagrange point, and then it can be captured by the primary star. These perturbations are always present,

so it will always happen this way. As long as the secondary star is filling up its Roche lobe, due to expansion of the star or shrinkage of the binary due to angular momentum loss, material will fall through the L_1 point and be captured by the primary. Since mass is easily removed when the lobe is filled, the secondary star will not be significantly larger than its lobe. However, the process of mass transfer will change the binary's mass ratio, $q = M_2/M_1$. The binary separation and period will be altered by the same process due to redistribution of angular momentum. Since the Roche geometry depends on a and q, the radius of the Roche lobe can change over the lifetime of the system. This is illustrated by the Pacynski formula (1971):

$$\frac{R_2}{a} = \frac{2}{3^{4/3}}(\frac{q}{1+q})^{1/3} \tag{1.3}$$

where R_2 refers to the Roche lobe radius of the secondary star. This equation only holds for a range of mass ratios from $0.1 \lessapprox q \lessapprox 0.8$. An approximate analytic formula was found by Eggleton (1983) that covers a wider range in q:

$$\frac{R_2}{a} = \frac{0.49q^{2/3}}{0.6q^{2/3} + \ln(1+q^{1/3})} \tag{1.4}$$

The overflow process will be sustained for some time, and in some cases can run away; so some process is required to increase the radius of the secondary star at a sufficient rate to keep it on the Roche surface or it will fall inside, halting accretion. This is determined by the total angular momentum of the system. In *conservative* mass transfer, we assume binary mass and angular momentum is constant. In this case the secondary is losing mass, and to conserve momentum the binary separation increases when the less massive star donates to the more massive star. Since more matter is placed near the center of mass, the secondary moves in a wider orbit, increasing a (King 2001). This is the case of interest for the systems discussed here. Conversely, transfer from the more massive star to the less massive would shrink the separation. The expansion of the secondary due to nuclear evolution is more relevant to systems with secondaries of intermediate type, and while it also happens for low mass secondaries, they are more likely to change their orbital separation due to angular

momentum redistribution or losses from magnetic braking or gravitational radiation (Frank, King, & Raine, 2002).

In the event that angular momentum is lost, or the binary is unable to conserve mass (due to losses from stellar winds, outflows from unbound material from the accretion disk, or jets expelled from the compact object) then unstable mass transfer will eventually result. For example, if the radius R_2 of the Roche lobe decreases faster than the radius of the donor star, violent overflow will occur, proceeding on a dynamical (i.e., free-fall) or thermal timescale depending on whether the star has a convective or radiative envelope (see Kippenhahn & Weigert 1990). The rapid transfer will stop once the donor has given enough mass to the primary so that it's radius can fall below R_2. All interacting binaries will go through this stage of evolution once the more massive star evolves off the main sequence, but it is short-lived and as such hard to observe. Other episodes could also occur, e.g., a binary may reach contact because of orbital shrinkage through momentum loss before the more massive star has evolved off the main sequence (as in Algols or supersoft X-ray binaries). If for some reason R_2 increases relative to the donor radius, the accretion rate is modulated on nuclear or angular momentum-loss timescales. A complete review of X-ray binary systems and accretion is given in Lewin, van Paradijs & van den Heuvel (1995) and Psaltis (2006).

1.2 Formation of an Accretion Disk

The gas in these systems has angular momentum, whether it is bound to the surface of one star or not. As material falls through the L_1 point, it continues on its own trajectory into the Roche lobe of the primary star, and will not be directly accreted (in most cases) onto the surface of the primary. A continuous stream of particles will be sent through the Lagrange point and the stream will eventually intersect itself resulting in dissipation of energy. The material will still have approximately the angular momentum it had upon leaving the secondary, and to rid itself of this, it will try to achieve the lowest state of energy, a circular orbit. We then expect the gas to orbit the primary initially, in the binary plane,

at a radius R_{circ} such that the Kepler orbit at this radius has the same specific angular momentum as the gas had at L_1. In terms of q this radius is expressed, for Roche overflow:

$$\frac{R_{circ}}{a} = (1+q)[0.500 - 0.227 \log q]^4 \tag{1.5}$$

It will form a ring of material around the primary star at this circularization radius, which viscosity will cause to spread inwards and outwards in radial distance, also heating the gas. So the net result is that the bulk gravitational energy of the gas will be converted into heat by viscous friction, which will then be radiated away. As it radiates, the gas loses energy and so will fall deeper into the gravitational well of the primary star, orbiting the primary more closely, requiring it to transfer its angular momentum outwards. Since circular orbits have the least amount of energy for a given amount of angular momentum, you can visualize the gas slowly spiraling in like a whirlpool (Fig. 1.3), radiating away as much energy as it can, until it hits the primary star. The inward spiral of gas forces the angular momentum to be transferred outwards, further away from the primary, as a given parcel falls inwards. This momentum transfer causes the outer parts of the disk to move further away from the primary. Our initial ring of gas has spread both inwards and outwards from its original radius until a pancake-like shape is formed, with a large amount of angular momentum being stored in very little gas on the outer edges of the disk. The outer edges of the disk do not extend beyond the Roche lobe radius of the primary, however; tidal effects act to cut the outer edge of the disk at a radius less than the lobe radius (usually 80-90% of the lobe radius) and angular momentum is transferred back to the orbit. This is the basis of the Shakura & Sunyaev accretion disk model (Shakura & Sunyaev 1973). A description of how viscosity works is given in Ch. 4, Section 2.1.

1.3 Radiation Processes

As the gas spirals into the black hole, or any other compact object, the ions are principally heated by viscous friction and the electrons in the gas try to radiate all the added heat away.

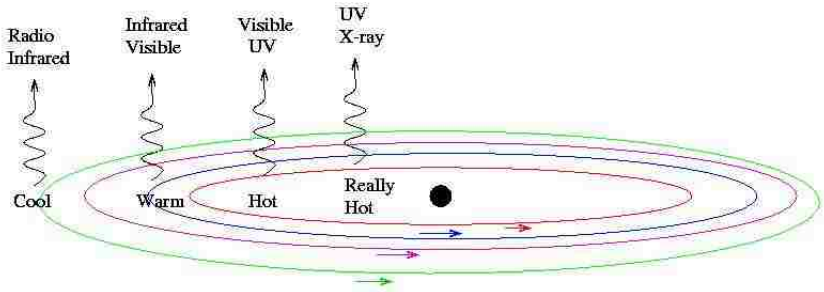

Figure 1.3: Schematic rendering of an accretion disk; here you can see how material heats up and emits shorter wavelengths of radiation as it moves inwards to the compact object.

However, based on the temperatures and densities of the infalling gas, as well as a source of hot photons bombarding the gas from near the central object (by either gas closer to the object itself, or the central object in the case of a white dwarf or neutron star, for example), different radiative processes take place that produce a peculiar spectrum, which observers analyze to determine what physics is actually taking place in the disk.

In the rest of this text I refer to processes such as Comptonization, bremsstrahlung emission, and blackbody radiation, which indicate certain physical reactions are occuring in the accretion disk. Here is a short overview of the most important forms of emission.

Bremsstrahlung emission: "Braking" radiation. When an free electron approaches a proton or an ion, the electromagnetic force between them causes the electron to accelerate (or decelerate as it passes by) and its path changes. The law of conservation of energy tells us that this energy cannot be lost and must be absorbed by the atom or converted to another form of energy. Electrons in this case are accelerating charges, and must radiate since we cannot balance energy and momentum without the photon emission. The energy used to slow the electron is excessive to the atom and the energy difference will be radiated as an X-ray photon (usually) of equal energy. In a given statistical distribution of gas at a high temperature, this produces a particular spectrum that is commonly seen in X-ray binaries and AGN, for example. In some cases this is approximated by a power-law.

Thermal emission: In general, this is emission from any body or gas that is in thermal

equilibrium. In general, thermal emission can apply to any radiation originating from a thermal electron distribution, such as thermal bremsstrahlung, or thermal synchotron. In this document and most publications, the term is used interchangeably with blackbody emission, in which the radiation itself is in thermal equilibrium. To approximate this spectrum, its common to use the integrated Planck function. This is the function used later to mimic the spectrum of the accretion disk.

Synchrotron emission: Radiation that is generated by the acceleration of ultrarelativistic (i.e., moving near the speed of light) charged particles through magnetic fields. The magnetic field interacts with the charged particles to give them a particular polarization that can be measured, which is how this type of radiation is usually identified. The planar acceleration geometry makes the radiation linearly polarized when observed in the orbital plane, and circularly polarized when observed at a small angle to that plane. Cyclotron radiation is the same, but produced by sub-relativisitic particles. Both are present in observations, and most astrophysical jets emit synchotron radiation. Observations of this type of radiation can tell us certain things about the strengths of the magnetic fields in these systems. For example, cyclotron radiation has a spectrum with its main spike at the same fundamental frequency as the particle's orbit, and harmonics at higher integral factors. These harmonics are the result of inhomogeneities in the actual emission environment, which also create a broadening of the spectral lines. The most obvious source of line broadening is non-uniformities in the magnetic field; as an electron passes from one area of the field to another, its emission frequency will change with the strength of the field.

Compton emission: Compton scattering or the Compton effect is the decrease in energy (increase in wavelength) of an X-ray or gamma ray photon, when it interacts with matter. Inverse Compton scattering also exists, where the photon gains energy (decreasing in wavelength) upon interaction with matter, and the matter cools. In the context of this work, blackbody photons from the disk are emitted into a hot corona above, that then hit those hotter electrons above, the blackbody photon gains energy, usually bumping it to a UV or

X-ray photon, while the gas in the corona cools. This produces a particular spectrum based on the thermal temperature of the blackbody source below, that is usually approximated by a power-law.

Synchoton Self-Compton (SSC): In general a distribution of electrons at some temperature and in the presence of magnetic fields which create synchotron photons, and those photons are them scattered by electrons in that distribution. In our context, low energy synchotron photons, from a jet or the corona, in the form of radio waves, are upscattered by inverse Compton to optical or ultraviolet photons. If the process occurs twice, the original photon is pushed into the X-ray range, and the process produces two distinct bumps in the total spectrum, which in some bands are approximated by a power-law. In most studies of X-ray binaries, this emission process is thought to occur in the corona, but modeling is extremely difficult.

Power-law spectrum: This is a catch-all term, used whenever the number density of particles with a certain energy, $(N(E))$, can be expressed in this way, $N(E) = CE^{-\Gamma}$, where C and Γ are numerical constants that are fitted to the observed spectra. Unfortunately, because of interstellar absorption (i.e., we cannot see in the UV or X-ray below ~ 0.5 keV) or the waveband coverage of a particular telescope or instrument, many of the radiation processes above appear to us simply as power-law distributions, and an independent study of one part of the spectrum usually cannot distinguish the emission process from Comptonization or bremsstrahlung or synchotron, and its likely that in nearly every case all processes are going on. Only precise theoretical modeling can predict the values for C and Γ, which after fitting to the spectra in each energy range (e.g., radio, UV, X-ray) give us clues about what is going on in the accretion disk.

1.4 Low Mass X-ray Binaries

The remainder of this dissertation will be focused on Low Mass X-ray binaries (LMXB). These are systems where we have either a neutron star or black hole being orbited by a

low mass, late-type main sequence or slightly evolved companion. LMXBs are all Roche lobe overlow fed into an accretion disk, which radiates like any other blackbody of multiple temperatures like most accreting systems. There is also a substantial component in the spectrum from X-rays, which cannot always be explained simply as blackbody flux extending into the soft X-ray band, and additional components are usually needed. Actually, the shape of the X-ray continuum is sometimes consistent with radiation from an optically-thin source such as Comptonized or bremsstrahlung (free-free) emission. They can, at certain times, contain a jet of highly relativistic material being ejected along the spin axis of the black hole which is inferred from radio emission. Closely related are the systems called microquasars, that are distinguished by their more active relativistic jets. They are highly variable in X-rays and systems are seen to go through a multitude of different observational states, where one component of the spectrum, (e.g., blackbody) changes in flux in relation to another (e.g., bremsstrahlung, Compton) over a period of time and sometimes from one observation to the next. These transitions, along with a specific study of the system V404 Cyg, are the subject of this work.

All of these systems are discovered in X-rays and usually during an outburst state, where the flux is considerably higher compared to the quiet ("quiescent") state. Following the discovery and the decay to quiescence, optical observations will see flux from the secondary and attempt to measure the parameters of the binary such as the type of secondary star (which tells us its mass, roughly), their orbital velocities and separations from the lightcurves, and if the mass function is determined (see Ch.2, Eq. 2.1), whether the primary is either a black hole or neutron star. For further background on X-ray and in particular black hole binaries, see McClintock & Remillard (2006) and Psaltis (2006).

1.4.1 Origins of the Primary Compact Object

A star that begins its life with a mass at least 8-10 times the mass of our own Sun will end its life in a far different way to how our Sun will die. As nuclear fusion progresses in their cores,

more and more layers of heavier elements are created in their interiors, from helium in its initial stage of life up to iron at the very end. Thermal pressure can support the star against its own weight until a sizeable iron core is created. When iron is created by fusion, it can no longer be fused into heavier elements to release energy to power the star, because iron has the highest binding energy per nucleon on the periodic table. Thus, when the energy generation stops, the pressure support in the center of the star disappears, and gravity begins to squeeze the core. Initially, after the thermal pressure support disappears, the iron core is supported by electron degeneracy pressure (basically that no two electrons can have the same set of quantum numbers), but eventually it grows too massive for this, and the core implodes. The core contracts until it reaches a point where the nucleons are squeezed together (protons and electrons are squeezed together into neutrons, releasing neutrinos) and can only barely hold themselves up against their own weight (neutron degeneracy pressure), if the mass of the core is not too great. Exactly what happens next is a debated area of research. We currently believe when the core stops contracting that a 'bounce' back outwards occurs along with an expulsion of neutrinos, which eventually leads to a supernova event. The rest of the star explodes outwards in a huge fireball capable of outshining all the other stars in a galaxy (see Woosley et al. 2002 for an excellent review of current supernova theory). We are finally left with a neutron star, with the mass of up to three times our Sun, in a package roughly the size of a city.

If the core is too massive, however, it can continue to collapse into a point of almost infinite density and infinitesimally small size. Around this point, called the singularity, an event horizon forms, whose radius depends on the mass of the singularity. The radius of the event horizon is generally expressed in units of Schwarzchild (or gravitational) radii, which is found simply from setting the kinetic energy equal to the gravitational potential energy:

$$R_g = \frac{2GM}{c^2} \tag{1.6}$$

At the event horizon, the escape velocity equals the speed of light, and not even light can

escape the gravitational pull. Material can fall in, but can never get back out. This is called a black hole. What this does to the material that once was the outer layers of the star is unclear (how much, if any is expelled, or if it falls into the hole), but the formation of a black hole may be linked to the hypernovae believed to power gamma ray bursts (Israelian et al. 1999; Brown et al. 2000; Orosz et al. 2001).

The properties of black holes are discussed in many textbooks, e.g., Shapiro & Teukolsky (1983). Two very important properties are the spin parameter, and the existence of an innermost stable circular orbit (ISCO). The three quantities which completely describe a black hole are its mass, its spin, and its charge. Since any appreciable charge will be quickly neutralized, this leaves us with mass and spin. The spin parameter is defined as

$$j = \frac{Jc}{M^2 G} \tag{1.7}$$

where J is its angular momentum, c the speed of light, and G is Newton's gravitational constant (note: I have used the letter j to describe the spin parameter, but nearly all authors use the letter a, this I have changed because of the numerous uses of this letter in the text). The spin parameter is defined in a range between 0-1, where zero corresponds to a Schwarzchild (non-spinning) hole, and one (maximally-spinning) is generically denoted as a Kerr black hole. Relativistic effects make maintaining a circular orbit in the vicinity of strong gravitational sources unstable, so there exists an innermost stable circular orbit, in contrast to classical mechanics. This lies at a radius of $R_{\rm ISCO} = 3R_g$ for a nonspinning black hole, while for a spinning hole it moves inwards as the value of j increases, until for maximal spin it coincides with the horizon. Within the ISCO, no circular orbit is possible.

The first strong evidence of the existence of a black hole was from the observations of the X-ray binary Cygnus X-1 (Bolton 1972; Webster & Murdin 1972). Today roughly two dozen similar X-ray binaries are known that contain compact objects believed to be too massive to be a neutron star (i.e., $M > 3M_\odot$). These systems, which I will call black hole binaries (BHBs), are the focus of this research.

The following chapters will first present the relevant background on observations of these systems, and the motivation for the research herein. Chapter 3 is devoted to my own X-ray observational studies of V404 Cyg. Chapter 4 will discuss the basics of accretion physics from a purely theoretical perspective, and then the characterization of the states as we currently understand them. Chapter 5 discusses the development of a theoretical model to attempt to explain the state changes observed. Relevant derivations for this work are attached for the interested reader in the Appendix.

2. Observational Background on Black Hole Binaries

2.1 A Review of Known Black Hole Binaries

The first two black hole binaries (BHBs) to be identified were Cyg X-1 (Bolton 1972; Webster & Murdin 1972) and LMC X-3 (Cowley et al. 1983). They were persistently bright in X-rays and their secondaries are massive early-type stars (White et al. 1995). These two systems are in the class of High Mass X-ray Binaries (HMXBs) and they accrete by stellar wind outflows. The third BHB identified, however, is very different from these two. A0620-00 was first seen in 1975 when it suddenly brightened to become the brightest X-ray source ever observed outside the solar system at the time (Elvis et al. 1975; see also Kuulkers 1998). Over the next year it decayed back to quiescence and became a rather feeble source in comparison (McClintock et al. 1995). Its optical counterpart similarly decayed, eventually revealing the secondary companion to be a K-type dwarf.

As of now, there are nearly two dozen confirmed BHBs, and nearly all of them are transient X-ray sources like A0620-00. Table 2.1 is adapted from Remillard & McClintock (2006), where they are listed by right ascension. Figure 2.1 shows scale drawings of 16 BHBs in our Galaxy, and an estimation of binary inclination is indicated by the tilt in the accretion disks.

The diversity in Table 2.1 shows that there are long and short period systems, systems with hot and cool giants (Cyg X-1 and GRS 1915+105) and many with small K-type companions. Three of them (Cyg X-1, LMC X-1, LMC X-3) are persistently luminous sources. The rest are transient sources with two exceptions, GRS 1915+105 and GX 339-4. The first has been in outburst for nearly 15 years since its first eruption in August 1992. GX 339-4 is an unusually active transient, and may be different in every observation, as it frequently goes

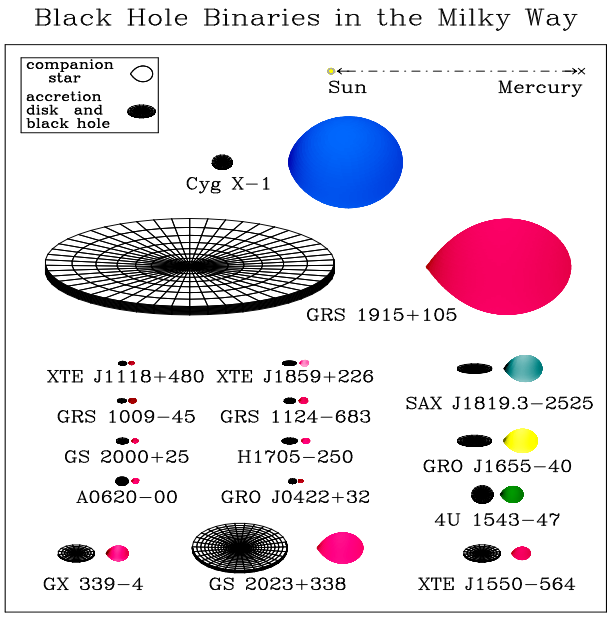

Figure 2.1: Scale drawings of 16 black-hole binaries in the Milky Way (courtesy of J. Orosz). The Sun–Mercury distance (0.4 AU) is shown at the top. The estimated binary inclination is indicated by the tilt of the accretion disk. The color of the companion star roughly indicates its surface temperature. Image reproduced from Remillard & McClintock (2006).

into outburst and then falls to a quiet state, but may not have ever reached true quiescence (Belloni et al. 2005; Shahbaz, Fender, & Charles 2001). In determining the mass of the black hole, the main observational quantity of interest is the mass function, derived from Kepler's Third Law (Eq. 1.1):

$$f(M) = \frac{P_{\rm orb} K_2^3}{2\pi G} = \frac{M_1 \sin^3 i}{(1+q)^2} \tag{2.1}$$

On the left hand side of this equation are the observable quantities, the orbital period P and the semi-amplitude of the velocity curve of the secondary star K_2. On the right hand side is the inclination angle i, the mass ratio $q = M_2/M_1$ (where M_2 refers to the secondary mass), and the black hole mass M_1. A value for $f(M)$ is determined by measuring the radial motion of the companion star, and then constitutes the minimum mass of the compact object, since $\sin^3 i < 1$ and $(1+q)^2 > 1$. Looking at Table 2.1, we can see many of the sources have a mass function value that requires a compact object mass greater than 3 $M_\odot$. This is generally

Table 2.1: Twenty confirmed black holes[a]

Coordinate Name	Common[b] Name/Prefix	Year[c]	Spec.	P_{orb} (hr)	f(M) ($M_\odot$)	M_1 ($M_\odot$)
0422+32	(GRO J)	1992/1	M2V	5.1	1.19±0.02	3.7–5.0
0538–641	LMC X–3	–	B3V	40.9	2.3±0.3	5.9–9.2
0540–697	LMC X–1	–	O7III	93.8[d]	0.13±0.05[d]	4.0–10.0:[e]
0620–003	(A)	1975/1[f]	K4V	7.8	2.72±0.06	8.7–12.9
1009–45	(GRS)	1993/1	K7/M0V	6.8	3.17±0.12	3.6–4.7:[e]
1118+480	(XTE J)	2000/2	K5/M0V	4.1	6.1±0.3	6.5–7.2
1124–684	Nova Mus 91	1991/1	K3/K5V	10.4	3.01±0.15	6.5–8.2
1354–64[g]	(GS)	1987/2	GIV	61.1[g]	5.75±0.30	–
1543–475	(4U)	1971/4	A2V	26.8	0.25±0.01	8.4–10.4
1550–564	(XTE J)	1998/5	G8/K8IV	37.0	6.86±0.71	8.4–10.8
1650–500[h]	(XTE J)	2001/1	K4V	7.7	2.73±0.56	–
1655–40	(GRO J)	1994/3	F3/F5IV	62.9	2.73±0.09	6.0–6.6
1659–487	GX 339–4	1972/10[i]	–	42.1[j,k]	5.8±0.5	–
1705–250	Nova Oph 77	1977/1	K3/7V	12.5	4.86±0.13	5.6–8.3
1819.3–2525	V4641 Sgr	1999/4	B9III	67.6	3.13±0.13	6.8–7.4
1859+226	(XTE J)	1999/1	–	9.2:[e]	7.4±1.1:[e]	7.6–12.0:[e]
1915+105	(GRS)	1992/Q[l]	K/MIII	804.0	9.5±3.0	10.0–18.0
1956+350	Cyg X–1	–	O9.7Iab	134.4	0.244±0.005	6.8–13.3
2000+251	(GS)	1988/1	K3/K7V	8.3	5.01±0.12	7.1–7.8
2023+338	V404 Cyg	1989/1[f]	K0III	155.3	6.08±0.06	10.1–13.4

[a]See McClintock & Remillard (2006) for columns 3–5, Orosz (2003) for columns 6–7 plus additional references given below.
[b]A prefix to a coordinate name is enclosed in parentheses. The presence/absence of a "J"indicates that the epoch of the coordinates is J2000/B1950.
[c]Year of initial X-ray outburst/total number of X-ray outbursts.
[d]Period and f(M) corrections by AM Levine and D Lin, private communication.
[e]Colon denotes uncertain value or range.
[f]Additional outbursts in optical archives: A 0620 (1917) and V404 Cyg (1938, 1956).
[g]Casares et al. 2004; possible alias period of 61.5 hr.
[h]Orosz et al. 2004.
[i]Estimated by Kong et al. 2002.
[j]Hynes et al. 2003.
[k]Period confirmed by A.M. Levine and D. Lin, private communication.
[l]"Q" denotes quasi-persistent intervals (e.g., decades), rather than typical outburst.

assumed to be the upper limit of the mass of a neutron star (Kalogera & Baym 1996). For the rest, additional data are required.

To truly pin down the mass of the compact object in BHBs, we must determine the inclination and the mass ratio. The inclination is provided by measuring the ellipsoidal variations in the secondary star. Ellipsoidal variations result when the surface of the secondary star becomes rotationally and tidally distorted from spherical with contributions as well from its non-uniform brightness distribution (Wagner et al. 1992). Although the variations we see are only weakly sensitive to q, they are strongly dependent on the inclination. Limb-darkening and gravitational brightening are effects that must also be taken into account. When a star is oblate, it has a larger radius at its equator than it does at its poles. As a result, the poles have a higher surface gravity, and thus temperaure and brightness. Thus, the poles are gravity-brightened, and the equator gravity-darkened. Limb-darkening refers to the diminishing intensity of the image of a star as one moves from the center to the edge, or limb. Fortunately we can study many systems in the infrared K band, where some uncertainties due to limb-darkening and gravity-brightening become negligible, along with contaminations from the accretion disk (Shahbaz et al. 1994b).

Under the assumption that the companion is tidally locked, spherically symmetric, and filling its Roche lobe, the rotational broadening of absorption lines (the approaching and receding sides of a star have blue- and red-shifted line profiles, and the observer sees a combination that is broader than the line itself) from the secondary star gives us a measurement of the mass ratio using the result from Wade & Horne (1988).

$$V_{rot} \sin i = 0.462 K_2 q^{1/3} (1+q)^{2/3} \tag{2.2}$$

If tidally locked, the companion appears to move like a solid body. The ratio of the left hand side of Eq. 2.2 to the semi-amplitude ($K_2 = V_{orb} \sin i$) is then just a function of the Roche radius to the semimajor axis of the system (distance of the center of mass of the companion

from that of the system), which is just the binary geometry. The geometry itself is merely a function of q (Eggleton 1983; see Eq. 1.3).

2.1.1 Review of Optical Observations of V404 Cygni

To illustrate the optical observations of LMXBs I will go over those performed for one BHB, V404 Cyg, which has been the subject of my own X-ray studies.

V404 Cyg was discovered by *Ginga* in outburst in 1989 (Makino et al. 1989) and early optical spectroscopy of the counterpart determined the orbital period to be 6.5 days (Casares, Charles & Naylor 1992). Spectroscopy also provides a lower limit on the mass of the compact object through the mass function, and the mass ratio (Casares & Charles 1994).

Casares & Charles (1994) resolved the rotationally broadened absorption features of the secondary star in V404 Cyg, using template stars that covered spectral types G8-K2 and luminosity classes III to V (corresponding to various subtypes of stars, III–giant, IV–subgiant, V-main sequence). Radial velocities are extracted through cross-correlation with template stars in the range 6212-6605Å, after removing the Hα emission and atmospheric band. The best fit template turned out to be that of a K0IV star, because it provides the lowest χ^2 sine fit. Four years of data taken on V404 Cyg helped them refine the orbital period to 6.47 days and the velocity semi-amplitude $K_2 = 208.5 \pm 0.7$ km s^{-1}. The mass function from these works was refined further to be $f(M) = 6.08 \pm 0.06$ M$_\odot$.

To determine the mass ratio of the system, Casares & Charles (1994) found the value of rotational broadening for this system using a technique from Marsh et al. (1994; there applied to A0620-00). Here they subtract different broadened versions of the K0IV spectrum from the Doppler-corrected V404 Cyg spectrum and perform χ^2 tests on the residuals. The broadened template is multiplied by a variable factor to account for any excess from the accretion disk prior to subtraction. They found that the minimum χ^2 was with a mean broadening (of the 14 templates used) of $V_{rot} \sin i = 39.1 \pm 1.2$ km s^{-1}, with an upper limit

of thirteen percent contamination due to the accretion disk. Inserting these values into Eq. 2.2 gave them a value for $q = 0.060^{+0.004}_{-0.005}$.

Closely related studies by Shahbaz et al. (1994b) fit the orbital light curve with an ellipsoidal model similar to what they applied to Cen X-4 and A0620-00 (Shahbaz et al. 1993, 1994a). After calculating the temperature of each element at the surface, the flux is calculated assuming a Kurucz (1991) solar-abundance model atmosphere spectrum, rather than a simple blackbody. The mass ratio and inclination are left as free parameters, and the surface temperature of the secondary was taken as 4360 K, close to what was previously derived by Casares et al. (1993). Using the values of rotational broadening and the velocity semi-amplitude from Casares & Charles (1994), they refined values for the mass ratio ($q = 0.058$) and inclination ($i = 56°$). Combining this with the value of the mass function for V404 Cyg, $f(M) = 6.08 \pm 0.06$ $M_\odot$, they can solve for the orbital separation and radius of the secondary of the system using Kepler's Law (Eq. 1.1) and the Pacynski formula (Eq. 1.2; 1971), and the allowed mass of the black hole as a function of secondary mass. The best fit mass of the secondary, 0.7 $M_\odot$, lends support for the evolutionary scenario of this system where the mass transfer is driven by the expansion of the secondary, which drives the systems to longer periods (Shahbaz et al. 1993, 1994a; see also Introduction) as opposed to the other situation (where the more massive star loses mass to the less massive star) where mass transfer is driven by the orbit shrinking due to angular momentum losses (see also King 1993).

The best fit for the mass of the black hole was very large (12 $M_\odot$, Shahbaz et al. 1994b), which raises the question for its formation. The classic scenario for the creation of such a system is one where we have a low mass star (roughly the mass of the Sun) in a wide orbit around the black hole progenitor that could have had 25 or more solar masses. To create such a large black hole, the progenitor must have been very massive and it is likely that a significant amount of mass was lost in the supernova event. If half of the total mass of the entire binary is expelled in the supernova, then the binary will separate, unless it is an

asymmetric explosion which gives the compact object a fortuitous velocity kick which would keep it bound (Blaauw 1961; Flanery & van den Heuvel 1975; see a review by Tauris & van den Heuvel 2003). A study of BHBs by Nelemens et al. (1999) estimated that a mass fraction of ~ 0.35 is likely lost in a (symmetric) supernova event that creates the black hole. For BHBs like V404, the survival is somehow affected by the amount of mass transfer from the progenitor to the secondary during its evolution before the supernova event. It remains an open question as to whether black holes would receive a velocity kick at birth; however, data of GRO J1655-40 seem to indicate that the explosion which created this black hole did in fact have a large velocity kick (Mirabel et al. 2002).

2.2 X-ray Observations of BHBs

2.2.1 X-ray Lightcurves

Most of the transient systems are only discovered when they go into outburst by wide-field X-ray cameras on satellites like the *Rossi X-ray Timing Explorer* (*RXTE*). Review papers (Chen et al. 1997; McClintock & Remillard 2006) show great diversity among these lightcurves, with varying timescales of rise and decay. Fig. 2.2 is an example of the original outburst of A0620-00 (Elvis et al. 1975; Kuulkers 1998). These outbursts can range from two weeks to several months in most cases (and sometimes up to 2 years, e.g., GRO J0422+322, Garcia et al. 1996) with the accepted cause being that of an instability within the accretion disk due to viscosity changes (so-called "Disk Instability model"; see Ch. 4, Section 3), or due to sudden increases of mass transfer from the donor star ("mass transfer instability"). Models developed initially for cataclysmic variables (Smak 1971; Lasota 2001) have been extended to X-ray novae to some extent (Dubus et al. 2001). They propose that the mass transfer rate from the secondary is insufficient to force a continuous viscous flow to the primary and so the gas piles up in the outer disk until a critical surface density is reached and the outburst triggers. The models predict recurrent bursts on the timescale of years, but this

does not apply to all systems. Some may become persistent sources for many years, or remain quiet for timescales far longer than predicted, so it is quite clear that the behavior of the companion star alluded to above is also playing a critical role. Study of the lightcurves continues into power spectra, and the presence of discrete timescales in the lightcurve called quasi-periodic oscillations (QPOs). This further timing analysis of lightcurves is elaborated upon in Section 2.3.

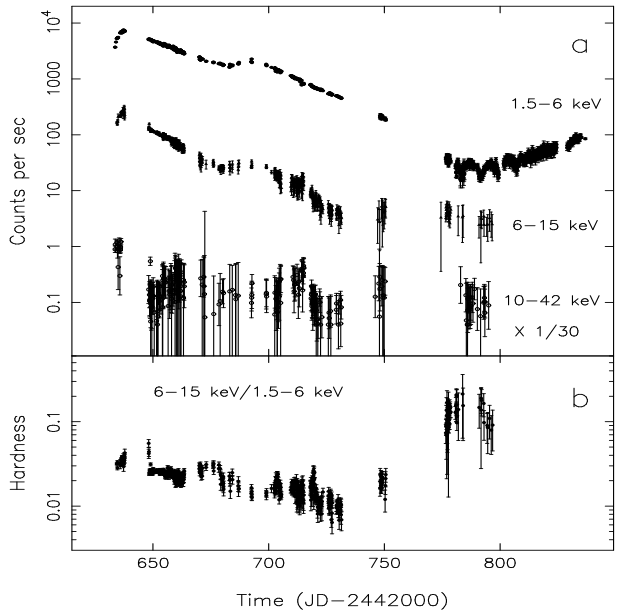

Figure 2.2: An example X-ray outburst light curve of A0620-00 as obtained with (from top to bottom) the *SAS-3* CSL-A (1.5–6 keV), CSL-B (6–15 keV) and CSL-C (10–42 keV) detectors aboard Ariel V during its first known outburst in 1975 (Elvis et al. 1975). The CSL-C light curve has been offset by a factor of 1/30 for clarity. Hardness light curve of A0620-00 is below. Hardness is defined as the ratio of the count rates from the CSL-B and the CSL-A detector. Note the clear hardening after JD 24462732. Image reproduced from Kuulkers (1998).

2.2.2 Spectra

The X-ray to gamma-ray spectra of BHBs is typically made up of two components, which vary in strength relative to one another and overall. A thermal component (attributed to an accretion disk; see 4.2.1) is modeled as a multitemperature blackbody, and often shows an

inner edge temperature of ~ 1 keV. The additional nonthermal component is usually modeled as a power law (PL) or broken power law (attributed to inverse Compton scattering in a corona or advective flow; see 4.2.2). The PL typically extends to far higher energies than the thermal component with an additional break at very high energies or an exponential cutoff. It is characterized by the photon index, Γ, where the spectrum goes as $E^{-\Gamma}$, that sometimes appears unbroken.

Some systems exhibit an additional iron Kα line that may be relativistically broadened. Also, when the disk is nearly face-on to us, spectral models require another disk reflection component known as the Compton hump (Done & Nayakshin 2001). Here the X-rays from the PL emitting material are Compton scattered by cold material in the outer disk and produce a spectral bump between 10 and 30 keV. The origin of this hump is that the low energy photons are removed by photoelectric absorption, while higher energies are downscattered into this range due to the dominance of first elastic then inelastic scattering.

2.2.3 Emission States of BHBs

Multiple spectral and timing states are seen in BHBs, the first noticable change in spectral states was in Cyg X-1 (Tananbaum et al. 1972) and the first seen in LMXBs was in A0620-00 by Coe et al.(1976). When A0620-00 was brightest, it was usually seen to have a soft thermal spectrum peaked at ~ 1 keV, which led to the identification of the state as the "high/soft state" (where high refers to the luminosity). When the source grew faint, it typically had a spectrum best described as a power law, with photon index $\Gamma \sim 1.7$, and was identified as the "low/hard state," and the thermal spectrum was not seen above 2 keV. Another state was seen in the early 1990's and was characterized by the presence of several-Hz QPOs, high luminosity, and a spectrum that was best fit with a composite of the thermal and steep power law ($\Gamma \sim 2.5$) components. This was called the "very high" state.

There were several problems with these definitions of spectral states when the number and quality of observations grew in the *RXTE* era (Remillard & McClintock 2006). Cyg X-1 was

observed to have a steep power law component in its soft state (Zhang et al. 1997), systems that were in their bright state were also seen to contain the steep power law component (McClintock & Remillard 2006), and QPOs of different types were seen in many systems over a wide range of luminosities (Morgan et al. 1997, Homan et al. 2001). This required a better delineation of the different states, which was done by McClintock & Remillard (2006).

The reclassification of states by McClintock & Remillard is motivated by the problem in the literature of proper state nomenclature. Different authors would use different criteria to delineate what they believed were different states of accretion, and the evolution was treated as a monotonic sequence of states. For example, some authors would solely use the presence or frequency of QPOs to determine the break between the hard, thermal and intermediate state, while some would only use the luminosity differences along with the changes in the spectrum (power-law domination vs. thermal dominated spectrum). For the most part, any system that was extremely bright could have been labeled as being in the "high" state, even if its spectrum was hard. In addition, a system could be in a bright thermally-dominated state, along with a strong power-law component, and simply be labeled as being in the "high/soft" state when its spectrum clearly shows the presence of several strong QPOs (which are more numerous in the "very high" state, but not the "high/soft" state). This confusion has been cleared up, and bolometric luminosity is more equal between the states, although not all authors are using their definitions, enumerated below.

The strategy utilized a spectral model consisting of a multitemperature blackbody and a PL component (with a break at 15 keV or exponential cutoff at higher energy), and, when necessary, the addition of an iron emission line or reflective component (with photoelectric absorption).

First I will define the parameters used in the model of McClintock & Remillard (2006) to make the distinctions and then describe each state in terms of them.

1. f - disk fraction, the ratio of disk flux to total flux in the range 2-20 keV (unabsorbed)

2. Γ - PL index, at energies below the break or cutoff

3. r - rms power in the Power Density Spectrum from 0.1-10 Hz, as a fraction of the mean count rate

4. A - integrated rms amplitude of any QPO seen in the range 0.1-30 Hz

(See also Table 2.2) Note also that f is used in Ch. 4 and 5 to denote the advection parameter and it will not be used to denote the disk fraction after this chapter. r is used to denote radius in units of Schwarzchild (R_g) in later chapters as well.

In the thermal state, flux is dominated by the soft thermal component from the accretion disk ($f > 75\%$). QPOs are usually absent or very weak, and the integrated aperiodic noise is faint (small r). Sometimes a second, nonthermal component is in the spectrum, but its contribution to the spectrum is weak.

In the hard state, a hard PL component ($\Gamma \sim 1.7$) makes up more than 80% of the spectrum, the aperiodic variability is strong ($r > 0.1$) and QPOs could be present. The thermal component, if seen, would make only a very small contribution to the spectrum. Correlations are observed in this state between radio and X-ray intensity (Gallo et al. 2003), and a quasi-steady and compact radio jet has been seen in this state (Fender 2006). VLBI images of sources in this state have shown compact jets (Dhawan, Mirabel, & Rodriguez 2000; Stirling et al. 2001). An end to jet activity is seen when the source changes emission states from hard to thermal and radio emission is quenched (Fender et al. 1999). The behavior of this state continues downwards in luminosity ($L_x = 10^{30} - 10^{33.5}$ erg s^{-1}) to the quiescent state (Corbel et al. 2008, Gallo et al. 2006, Yuan, Cui & Narayan 2005), with PL indices ranging from $\Gamma \sim 1.5 - 2.1$ (though generally softer than the hard state for a source) and it is assumed that the same PL mechanism is operating. In this state, dynamical measurements of the black hole mass are made since the optical component is dominated by the secondary star, and the lack of radiative efficiency from the accretion disk is a prime argument for an event horizon (Narayan & McClintock 2008).

Both the hard and thermal states appear stable and have been observed in some low-mass systems to last for months or even years (e.g., GX 339-4, which remained predominantly in the hard state from the launch of *RXTE* until 1999), while intermediate or higher luminosity observations are often associated with transitions and show stronger and faster variations in their properties (Miyamoto et al. 1994; Homan et al. 2001; Cui et al. 2000). High-mass systems like Cyg X-1 tend to alternate between long sustained periods in one state or the other for years as well.

The steep power law (SPL) state (a redefinition of the former "very high" state) contains a strong PL component with photon index $\Gamma \sim 2.5$, which may continue without a break up to energies of 1 MeV or higher. A sizeable thermal component is also present in the spectrum, and QPOs are seen. The power law component of similar index is also seen in the thermal state, but the distinction is that in the thermal state that component is weak in comparison to the thermal component and the index varies more in the thermal state. This state is typical of BHB systems approaching the Eddington limit (see Chapter 4), and violent jet ejections have been seen to occur in this state (e.g., GRS 1915+105; Rodriguez et al. 2008, Rothstein et al. 2005). Example observations of these states for the system GRO J1655–40 are depicted in Fig. 2.3, with QPOs appearing as peaks in the power spectra plotted on the right.

2.2.4 Jet Behavior in These Spectral States

The hardness-intensity diagram (HID) in Fig. 2.4, from Fender et al. (2004) and strongly influenced by observations of GX 339-4 (Belloni et al. 2005), best illustrates the activity of the jet as the transient systems follow their "hysteresis" path through the different X-ray states. However, I should point out that interpretation of the variation in the HID depends on the particular energy bands chosen to define the "hardness ratio" in any given study, e.g. if the chosen bands are above ~ 5 keV then the ratio tracks the PL component's slope, whereas if a softer band is chosen then you are seeing a possible mix of thermal

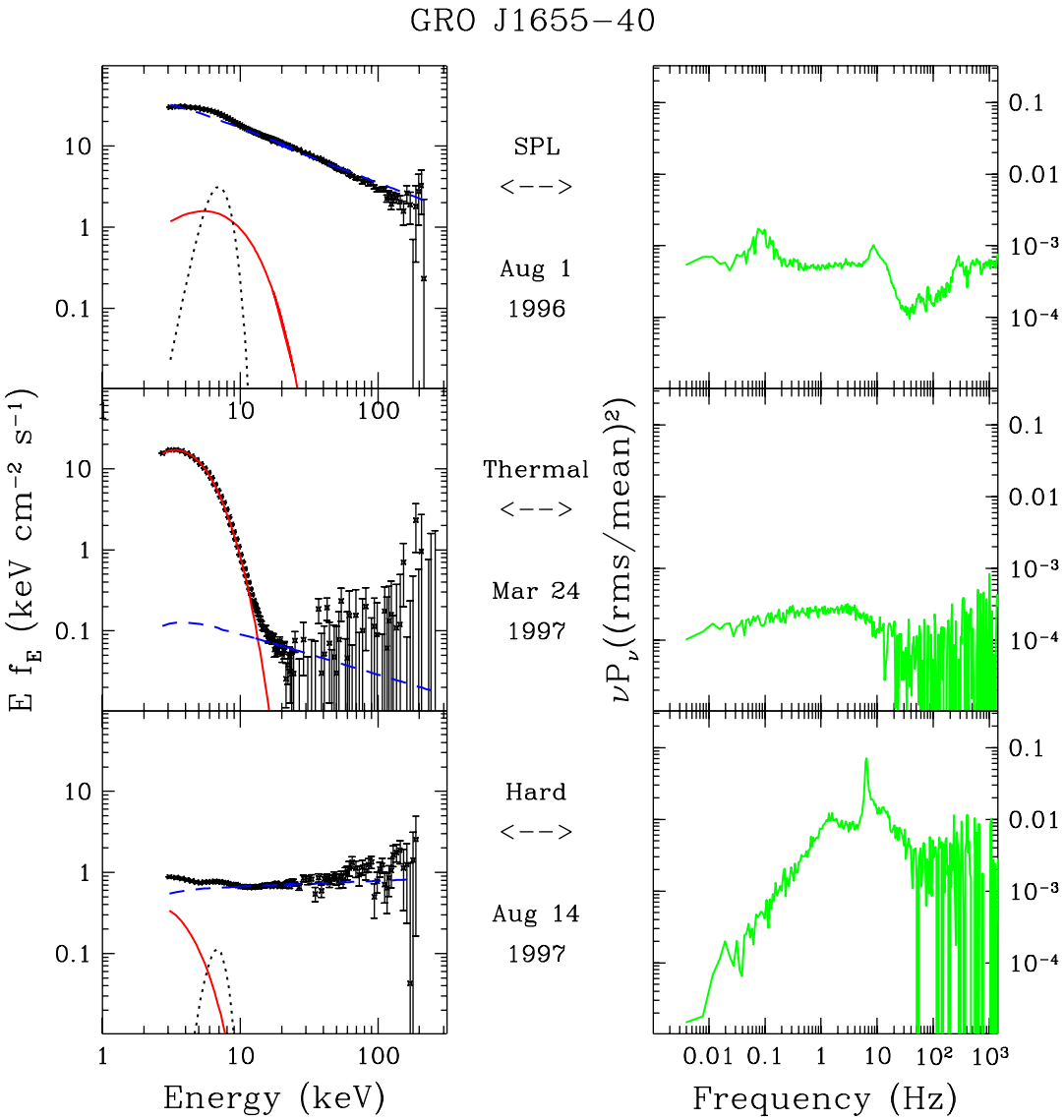

Figure 2.3: Sample spectra of black-hole binary GRO J1655–40 illustrating the three outburst states: steep power law, thermal, and hard. Each state is characterized by a pair of panels. Left panels show the spectral energy distribution decomposed into three components: thermal (*red*, *solid line*), power-law (*blue*, *dashed line*), and a relativistically broadened Fe Kα line (*black*, *dotted line*). Right panels show the PDSs plotted as $\log(\nu \times P_\nu)$ versus $\log\nu$. Figure reproduced from Remillard & McClintock (2006).

Table 2.2: Outburst states of black holes: nomenclature and definitions

New State Name (Old State Name)	Definition of X-ray State[a]
Thermal (High/Soft)	Disk fraction $f^b > 75\%$ QPOs absent or very weak: $A^c_{\rm max} < 0.005$ Power continuum level $r^d < 0.075$[e]
Hard (Low/Hard)	Disk fraction $f^b < 20\%$ (i.e., Power-law fraction $> 80\%$) $1.4^f < \Gamma < 2.1$ Power continuum level $r^d > 0.1$
Steep Power Law (SPL) (Very high)	Presence of power-law component with $\Gamma > 2.4$ Power continuum level $r^d < 0.15$ *Either* $f^b < 0.8$ and 0.1–30 Hz QPOs present with $A^c > 0.01$ *or* disk fraction $f^b < 50\%$ with no QPOs

[a]2–20 keV band.
[b]Fraction of the total 2–20 keV unabsorbed flux.
[c]QPO amplitude (rms).
[d]Total rms power integrated over 0.1–10 Hz.
[e]Formerly 0.06 in McClintock & Remillard (2006).
[f]Formerly 1.5 in McClintock & Remillard (2006).

and nonthermal components and interpretation is more complicated. The figure shows, qualitatively, how the jet's Lorentz factor, Γ, and morphology evolve with changes in the states (Note that this Γ is different from the photon index, however the Lorentz factor will not be mentioned beyond this section). The solid vertical line running through both figures is the "jet line," to the left of which jet activity disappears and marks an instability strip where violent ejections of matter can occur due to shocks in the jet.

The evolutionary track of a system is described by starting from the farthest right and lowest intensity, the quiescent state (i). Here is where a BHB will spend the majority of its life and some systems remain for years or decades in this region. Radio emission is seen and assumed to be from a jet (inferred from the characteristic flat spectrum), the X-ray spectrum is hard, and the luminosity is very low. The schematic pictures on the side show how the jet behaves as the states change. As the system leaves the quiescent state, it moves upwards in intensity along the right hand side of the graph, the jet grows slightly stronger

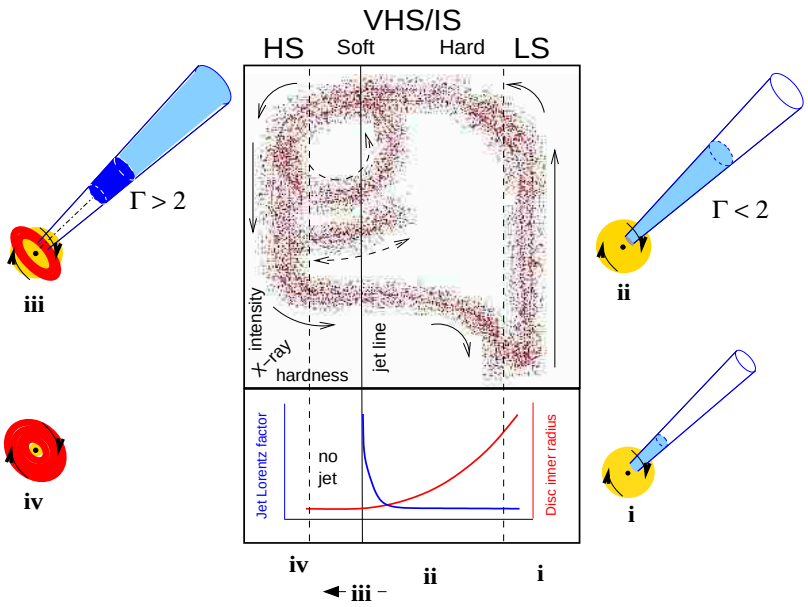

Figure 2.4: Graphical schematic of the disk-jet coupling. The top graph shows evolutionary tracks in a plot of intensity versus hardness ratio in the X-ray band (increasing up and to the right, respectively) that are explained in the text. The lower panel shows the bulk Lorentz factor of the jet as a function of hardness. X-ray states are labeled in the old nomenclature along the top. Figure reproduced from Remillard & McClintock 2006.

and the system continues to show a hard PL spectrum (ii). As the luminosity increases, some low-frequency QPOs have been seen in the hard state of a few systems (Rossi et al. 2004). At some point a thermal component begins to show (indicated by the red color in iii), QPOs are seen (dashed line) and the system moves into an intermediate state, which in this graph can overlap with the SPL state (SPL systems would also lie between the jet line and the dashed line on the right, though they may continue higher in luminosity than is depicted). The thermal component continues to strengthen, and the power law index becomes steeper as the system moves to the left. When it crosses the jet line, shocks in the jet occur and matter is ejected at high Lorentz factors (iii), and afterwards the jet is quenched. The system is now in the thermal state (iv) with a weak PL component present, and it is here that in some systems an iron line has been observed at 6.4 keV, attributed to cold material within an accretion disk close to the black hole.

In the thermal state, systems are seen to make several loops in the HID, moving back to the right, across the jet line and then coming back to the left into the thermal state. Mass ejections still occur, as the jet switches on and off again, though it has not been seen to be stronger than the initial ejection. The intensity gradually decreases while remaining thermally dominated, until the system reaches the lower left point on the graph and makes its track to the right, back to the quiescent state. It is the movement along this lower intermediate track that originally motivated the theoretical work in later chapters.

2.3 Quasi-Periodic Oscillations

Transient sources like V404 Cyg are highly variable in X-rays. Their brightness can vary by several orders on timescales as short as milliseconds. The analysis technique used to probe variability on short timescales is the power-density spectrum (PDS), which can exhibit a link between oscillations in brightness and an individual frequency component (Leahy et al. 1983). To understand what a PDS is, imagine modeling a lightcurve as a superposition of sine waves. Mathematically it is simply the Fourier transform of the lightcurve. This allows us to measure the most important timescales in the lightcurve. PDSs are interpreted under the assumption that the source variations are a locally stationary process. A good review of other techniques, such as phase lags and coherence is given in Vaughan & Nowak (1997).

Both the shape and integrated amplitude (e.g., 0-10 Hz, expressed in units of rms fluctuations scaled to the average count rate) of the continuum PDS are of prime interest. The PDS also show broadly peaked somewhat coherent intensity fluctuations, occuring approximately periodically, called quasi-periodic fluctuations (QPOs), that tend to separate in frequency space into two regions: 0.1-30 Hz (low frequency) and 40-450 Hz (High frequency) with different supposed causes for each (note that some authors may group the low and high frequency QPOs differently). These oscillations are important because they show there may be some preferred characteristic timescale, perhaps of resonant modes in the disk, or of disk truncation radii.

As an example of the types of noise seen in the PDS, refer to Fig. 2.5. There are three main types of noise seen in these figures. White noise is independent of the frequency, and is present as statistical noise seen in each figure. Red noise is stronger at low frequencies and has a power-law dependence, which can be easily seen in the examples of the HS and SIMS. Band-limited noise is red noise that appears to have a cutoff or break frequency, which defines some characteristic timescale (easily seen in the HIMS and LS figure, note the change of slope around the QPO).

Unfortunately there are several theories as to their cause, but none have been proven. Most QPOs appear to be associated with nonthermal states and state transitions (notice the absense of peaks in the HS portion of Fig. 2.5), and so could someday tell us about the physics distinguishing the different states, and possibly probing strong-field gravity. They are not strictly periodic, so their precise frequency does vary. They tend to persist during the SPL and hard states. Because it is important to cover what little we do know and understand about the cause of QPOs and because their characteristics vary during state transitions (absence/presence and frequencies), the following sections will give a short review of their types, but they are not the primary focus of the research.

2.3.1 Low-Frequency

Low-frequency QPOs (0.1-30 Hz) have been seen for at least 14 BHBs and are important for the following reasons: they can have high amplitude, they are relatively coherent, and their frequencies and amplitudes are generally correlated with the spectral parameters (Muno et al. 1999; Sobczak et al. 2000a; Revnitsev et al. 2000). This type of QPO appears whenever the SPL component makes up more than 20% of the flux between 2-20 keV (Sobczak et al. 2000) and are typical of the hard state as well. They can also vary on scales as short as minutes (Morgan et al. 1997), or can be stable and persistent for days or weeks (Muno et al. 2001). The latter would seem to suggest they are tied to the mass flow in the accretion

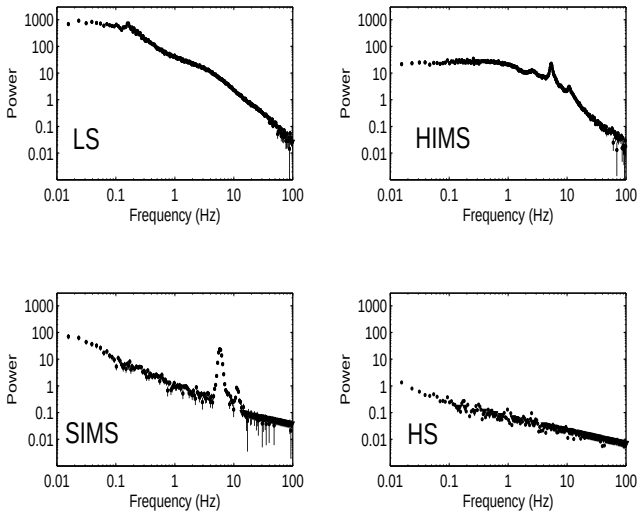

Figure 2.5: Examples for power spectra of GX 339-4 corresponding to the four states described in the text (adapted from Homan & Belloni 2005). The states pictured are in the old nomenclature. The HIMS (high intermediate) is analogous to the SPL state or the transition between the hard and thermal states, while the SIMS (soft intermediate) is primarily the thermal state at high luminosity.

disk (e.g., a 3 Hz orbital frequency around a nonspinning black hole of 10 $M_\odot$ corresponds to a radius of 100 R_g, which is plausible for a disk truncation radius in the hard state).

The rms amplitude of these QPOs peaks at or above 10 keV and have been seen at much higher energies (Rodriguez et al. 2002; Tomsick & Kaaret 2001). This suggests that they are somehow tied to the PL mechanism. However, if the PL mechanism is inverse Compton scattering of the thermal disk photons, and if the scattering geometry does not destroy the coherence of the original oscillation, the disk could be the true source of the QPO. Also, a mechanism in the disk that creates electrons for Compton scattering could be oscillatory, tying in the disk temperature or thermal energy flux to the QPO's properties.

There are three subtypes of low-frequency QPOs seen in BHBs (A, B, and C) analogous to the three QPOs of Z-type neutron star LMXBs (Casella, Belloni, & Stella 2005). These are based on studies of phase lags (a time lag between signals in different energy bands,

multiplied by the frequency) and coherence functions (measuring the relative strength of the QPO) comparing two different energy bands in the X-ray spectrum, which show positive (A), negative (B), and $\sim$ zero lags (C). The A and B types are associated with the SPL state, and the presence of high frequency QPOs. The C-type occur in the intermediate and hard states, and show a relationship between frequency versus disk flux. This type could be tied directly to both the thermal and PL components of the spectrum, and may tell us the origin of the PL spectrum. Models for low-frequency QPOs must account for the range of observed frequencies and that the oscillations are strongest for photon energies above 6 keV. Explanations range from global disk oscillations (Titarchuk & Osherovich 2000), radial oscillations of shock fronts (Chakrabarti & Manickam 2000), and oscillations between the disk and a hotter Comptonizing corona (Nobili et al. 2000). Another invoked spiral waves in a magnetized disk (Tagger & Pellat 1999) which combined magnetic instabilities with Keplerian motion.

Low-frequency QPOs are more common and can be much stronger than high frequency QPOs. If they are Keplerian frequencies, the slower QPOs relate to radii of several hundred R_g; however their energy dependence argues for them arising from closer to the black hole and would thus represent suborbital frequencies.

2.3.2 High-Frequency

High-frequency QPOs (40-450 Hz) have been seen in seven sources, and are highly transient and subtle (integrated rms amplitudes $\sim$ 0.01). Their frequencies, e.g., 150-450 Hz, are in the expected range for material at the ISCO of a black hole of roughly 15-5 $M_\odot$, which mirrors the range of observed masses in these systems.

High-frequency sources can either show single oscillations (Cui et al. 2001; Homan et al. 2003), or show a pair of peaks in a 3:2 ratio that do not appear at the same instant (Remillard et al. 1999). GRS 1915+105 has two pairs of peaks, one in a 3:2 ratio and one that are not (113, 168 Hz, Remillard 2004; 41, 67 Hz, Strohmayer 2001). They do not shift

in frequency in response to large luminosity changes (factors of 3-4, Remillard et al. 2002), though the ones in a 3:2 ratio do change a little (15%; Remillard et al. 2002). Since they are fairly stable, they are looked at as being a key property that may depend on the mass and spin of the black hole.

All of the high-frequency QPOs seen above 100 Hz occur in the SPL state. The ones which show a 3:2 ratio only exhibit the $2\nu_0$ when the PL is very strong, and the $3\nu_0$ when the PL is weaker. Theoretical explanations for high-frequency QPOs are still in their infancy and so far none include radiation mechanisms, so they do not yet explain the key spectral properties of the oscillations. Resonance mechanisms have been proposed by Abramowicz & Kluzniak (2001) and Merloni et al. (1999) using general relativity (GR) that scale in 3:1 and 3:2 ratios with simple particle orbits (e.g., a particular radius where there is a resonance between the polar and radial coordinates). Newer models use fluid flow in GR where the resonances come from a coupling between radial and polar coordinate frequencies (Abramowicz et al. 2003; Kluzniak et al. 2004), and one recent MHD simulation involves the coupling between azimuthal and radial coordinate frequencies (Kato 2004). If blobs of gas do happen to congregate at a certain radius, ray tracing calculations show that it could show up in the PDS as a QPO (Schnittman & Bertschinger 2004). If these QPOs are relativistic oscillations, it is possible that the 3 systems for which we have measured masses, XTE J1550-564 (Orosz et al. 2002), GRO J1655-40 (Shahbaz et al. 1999), and GRS 1915+105 (Fender et al. 1999) also have the similar values of the spin parameter j. This could be used as a probe of strong gravity regimes.

2.4 Iron Kα Lines as a Probe of Strong Gravity

In luminous AGNs and quasars, the Fe Kα fluorescence line was not detected often before the advent of larger effective area instruments such as *Chandra* or *XMM*. Some recent results show that a 6.4 keV line appears in half of the observed quasars, with broad lines seen in about 10% of the systems. Kα emission lines result when an electron transitions to the

innermost "K" shell (principal quantum number 1) from a 2p orbital of the second or "L" shell (with principal quantum number 2). The line is actually a doublet, with slightly different energies depending on spin-orbit interaction energy between the electron spin and the orbital momentum of the 2p orbital. Kα is typically by far the strongest X-ray spectral line for an element bombarded with energy sufficient to cause maximally intense X-ray emission. In iron, this doublet is centered at 6.4keV. In addition, the 6.7 keV line feature can be produced by the radiative recombination cascade, collisional excitation, and fluorescence of He-like Fe XXV, which can exist in a very high temperature plasma (House 1969; Makishima 1986).

Owing to their abundance and fluorescent yield, the Fe K-shell lines are the strongest emission lines in the X-ray spectra of AGN and X-ray binaries. The 6.4 keV line is thought to be generated by irradiation of a cool accretion disk by a hotter X-ray source. The external source of X-rays is required because accretion disks do not efficiently self-irradiate; their emission peaks below the energy required to remove K-shell electrons from iron. It has long been thought that the X-rays are created by a diffuse corona above the disk through inverse Comptonization. Many disk findings imply that the source must be rather compact, and recent discoveries of X-ray to radio flux correlations imply that somehow the jet could be involved (via synchotron and/or synchotron self-Compton), or at least the process which creates the jet (also suggesting its base may be only a few R_g in size). Relativistic beaming and gravitational or Doppler shifts in the inner disk cause the line profile to be asymmetric (see a review by Reynolds & Nowak 2003; Miller 2006).

X-ray spectral fitting packages such as XSPEC (Arnaud 1996) use several theoretical models to properly deduce the inner radius of the accretion disk from the line profile. The inner disk is truncated inside a radius of $R_{\rm ISCO} = 6GM/c^2$ (see Introduction Eq. 1.5) from the black hole in the absence of black hole spin. It is thought that studies of the line profile can show how fast the black hole is spinning. Because as we increase the spin, the $R_{\rm ISCO}$ moves closer to the black hole (See Fig. 2.7). Inspired by the detection of the first broad Fe K line in stellar-mass black holes from Cyg X-1 (Barr et al. 1985), models were created which

test two extreme cases: a non-spinning (Schwarzchild) black hole (Fabian et al. 1989), and a maximally spinning (Kerr) black hole (Laor 1991). Both predict a strongly asymmetric line profile with a red wing that extends much lower in energy. In 2004, new models became available that allowed for adjustable values of the spin parameter (j; see Introduction) that could be constrained by spectra (Dovciak et al. 2004; Beckwith & Done 2004). The most important parameters in these models are the inclination of the disk to the observer, the disk temperature, the ratio of incident to reflected emission (also referred to as the covering factor), and the disk ionization state.

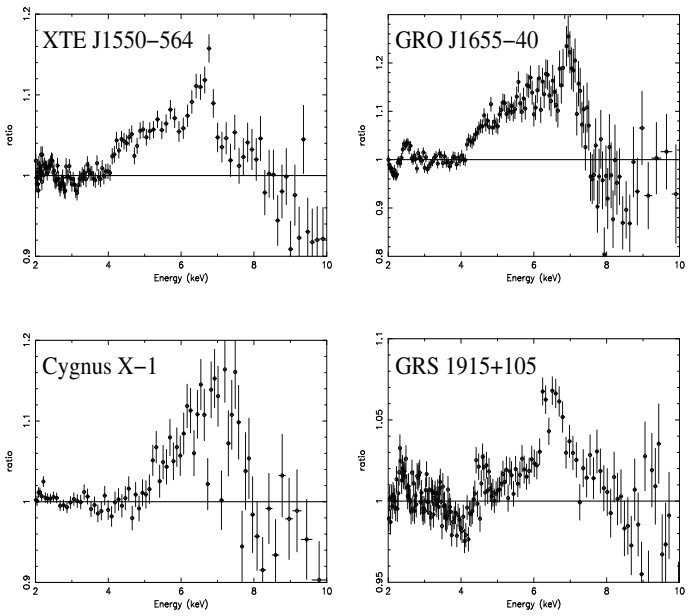

Figure 2.6: The figure above shows the relativistic disk line profiles revealed in an analysis of archival *ASCA*/GIS spectra of stellar-mass black holes that were observed in bright phases. The line profile in GRS 1915+105 is clearly not as skewed as the others, and does not strongly require black hole spin. (Adapted from Miller et al. 2005).

These black hole spin measurements depend on two principles upheld by observations and sound arguments. First, the accretion disk extends down to the ISCO for a certain value of j at all accretions rates above a certain threshold. Second, gas within the ISCO emits only weakly. Arguments suggest that the gas here should be completely ionized and so would be a negligible source of line emission (e.g., Young et al. 1998).

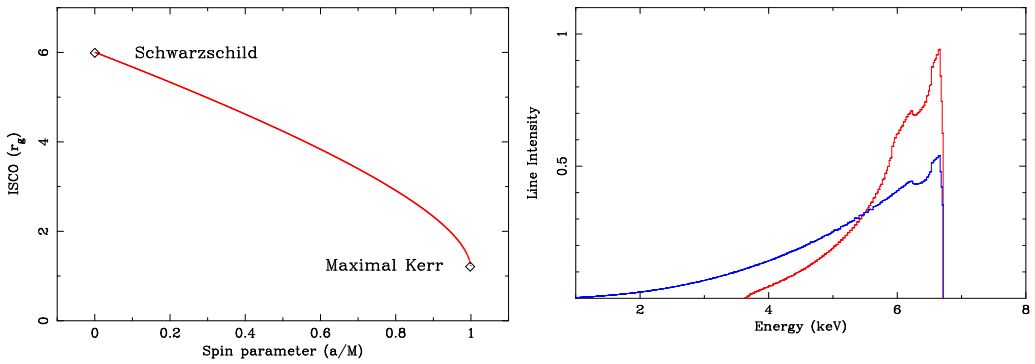

Figure 2.7: *Left*: The dependence of the innermost stable circular orbit (ISCO) on the black hole spin parameter is shown here, from Schwarzschild ($a = 0$) to maximal Kerr ($a = 0.998$) solutions. *Right*: The line profiles predicted in the case of Schwarzschild (red) and maximal Kerr (blue) black holes are shown here. It is the extent of the red wing and its importance relative to the blue wing that allow black hole spin to be determined with disk lines. (Adapted from Fabian & Miniutti 2005).

It must be stressed that detection of broad lines represents an observational challenge, mostly due to limited statistics. The lines are easy to detect if the disk is truncated at larger radii and/or the radial emissivity profile is not centrally concentrated, so that the line is not broad and can be distinguished from the continuum. On the other hand, if the black hole is rapidly spinning so that a standard cold disk can extend to small radii and the profile is centrally concentrated (as it should be in bright states), the line becomes so broad that its low contrast against the continuum makes it a challenge for detection even for *XMM-Newton* (Fabian & Miniutti 2005). In the latter case, the line would only be detected easily if the system has a super-solar abundance and/or a large reflective component. In quiescence, the disk is not expected to be close to the black hole, and thus we do not expect a broad line. However, Nayakshin & Svennson (2001) dispute that the disk truncates at all, and do not expect central concentration of the emitting region. In their model, most of the X-ray emission comes from a corona above a thin disk, at large radii. Our results, discussed in Ch. 3 point to this not being the case however.

2.5 Review of X-ray State Transitions During Outburst Decay

It is generally believed that the state transitions involve large restructuring of the accretion geometry of galactic black holes (Esin et al. 1997; Zdziarski et al. 2002). Therefore, analysis of these sources during state transitions may probe the dynamics of their accretion structure. Although the mass accretion rate is a very important parameter, it is unlikely that the states and transitions are solely determined by this parameter, and for systems that go through a hysteresis of states, a second parameter seems to be required to explain the complexity of the transitions, though it is not clear exactly what this might be. A key parameter could be the inner radius of the disk or the radial extent of the corona, but this would likely depend on the accretion rate as well.

Several results show interesting behavior as the system makes its journey from the thermal state back to quiescence. It was thought that during the transition downwards, the accretion disk would just move away from the ISCO to a more extreme radius in quiescence (100-1000 R_g; Esin et al. 1997); however, the evaporation that causes this should occur in the disk first at an intermediate radius (e.g., 50 R_g) because the accretion rate there must drop before the rate in the inner disk, as pointed out by Meyer et al. (2006). This leaves behind a residual inner disk with a gap between it and the outer disk. This inner disk should quickly disappear in a viscous timescale ($t_{visc} \sim R/v_R \sim$ a few days), but observations show that this intermediate state lasts much longer, on the order of two weeks, which implies that somehow the inner disk is being replenished and not disappearing as fast as we might expect.

Work by Kalemci et al. (2004) defines the transition in terms of timing (QPO presence/absence and study of the PDS) rather than a change in spectral properties (as many authors prefer to use, given the ambiguity in the old nomenclature). All of the sources they study show distinct changes in variability in less than 2 days, but that is not the case for spectral properties. The transitions from thermal state to hard state were marked by a very

large increase in the rms amplitude of variability and a change from a featureless Poisson noise-dominated PDS with only a few percent rms amplitude to one showing well-defined broadband variability and appearance of QPOs.

The PL component in the thermal state may be due to Comptonization of disk photons (Coppi 1999) or bulk-motion Comptonization (Laurent & Titarchuk 2001), whereas in the hard state it is thought to be thermal Comptonization. However, if the form or composition of the corona changes during the state transition, we would expect a change in the PL index and the ratio of PL flux to total flux (PLR), particularly if the type of Comptonization is what is changing. There are two ways to increase the PLR: either we increase the number of disk seed photons or increase the area of the corona that intercepts them. The former is unlikely as the corona is believed to be optically-thin, and the increase in soft flux should be observed, unless their energies are below that of X-ray telescopes. The work by Kalemci et al. (2004) indicates that when the PLR reaches a certain value, the variability greatly increases, which supports the idea that there is a second important parameter that may be the size of the corona (Homan et al. 2001).

The evolution of the disk parameters is also interesting. After the appearance of QPOs in the Kalemci et al. (2004) study, the inner disk temperature, the disk blackbody flux, PL index, and the characteristic frequencies of the variability change in a consistent way with the idea that the inner disk is retreating from the ISCO. In the basic formulation, an optically-thick disk has a temperature profile that decreases with increasing distance. So, if the inner disk is retreating as a result of evaporation, we should expect the inner disk temperature and the flux to decrease. The drop of spectral index may also be a sign of this retreat, because as the disk is close to the hole, its temperature and flux are higher, allowing the corona to cool effectively which keeps the spectral index higher (Zdziarski et al. 2002). For the sources studied in Kalemci et al. (2004), the disk component in the X-ray band was unobservable after 15 days from *RXTE*.

It is also expected that the characteristic frequency (of QPOs) decrease as the inner

disk radius increases. The shortest timescale in the disk (that we know of) is the dynamical timescale and is shorter close to the hole, which is where we think the high frequency variability is coming from. If the disk then retreats, the dynamical timescale at the inner edge will increase ($t_{dyn} \sim 1/\Omega$), and the characteristic frequencies seen in the PDS decrease (although the exact correlation between the two is not clear) (Kalemci et al. 2004).

2.5.1 GX 339-4 Case Study

GX 339-4 is the source with the best observations of hysteresis evolution, and has been observed in all canonical states since its discovery (Markert 1973). Observations of its secondary component alone are extremely difficult, because it is quite dim and the source has never been seen to fall into true quiescence, so a definitive dynamical mass has yet to be measured, and its classification as a black hole X-ray binary since its discovery was based purely on X-ray characteristics and behavior which are similar to Cyg X-1. A high mass function has been estimated however, ($f(M) = 5.8 \pm 0.5$ M$_\odot$), indicating that it should contain a black hole, but the exact distance is not known, with a lower limit of 6kpc (Hynes et al. 2003, 2004). Belloni et al. (2005) recorded its timing properties with *RXTE* during its 2002/2003 outburst, and again in 2004 (Belloni et al. 2006). Since its discovery it has remained prevalently in the hard state, although some transitions were seen (Miyamoto et al. 1991; Nowak et al. 1999; Belloni et al. 1999). In 2000 it had apparently declined into quiescence (Kong et al. 2000; Corbel et al. 2003). Another outburst began in 2002 and ended in 2003 (Nespoli et al. 2003; Belloni 2004; Buxton & Bailyn 2004). After another year in quiescence, it again went into outburst (Buxton et al. 2004; Belloni et al. 2004). A broadened iron line was detected, indicating a non-zero angular momentum in the black hole (Miller et al. 2004a,b).

It was the first system to show a radio/X-ray correlation in the hard state (Markoff et al. 2003). Radio observations in 1999 showed clear evidence of a strong decrease of core radio emission during the hard state (Fender et al. 1999b). During the later 2002/2003

outburst, near the SPL state transition (Smith et al. 2002c), a bright radio flare was seen (Fender et al. 2002), which led to the formation of a large scale jet (Gallo et al. 2004). Fig.

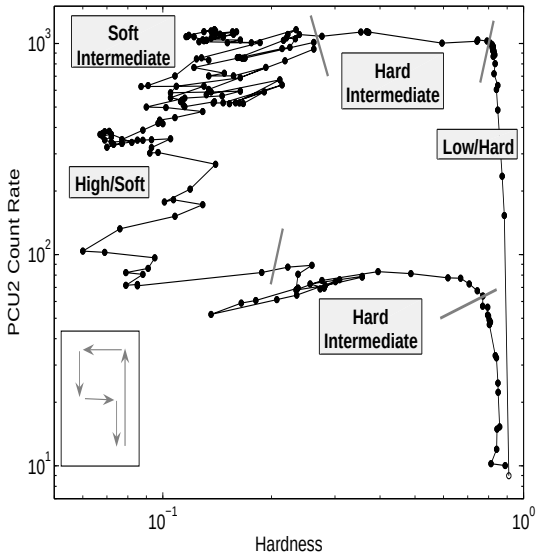

Figure 2.8: Hardness-Intensity diagram of the 2002/2003 outburst of GX 339-4 as observed by the RXTE PCA. The gray lines mark the state transitions. The inset on the lower right shows the general time evolution of the outburst along the 'q'-shaped pattern. The hard intermediate state on the lower side of the 'q'-shaped pattern is the region of interest for this proposal. From Belloni et al. (2005). State nomenclature is of the old convention.

2.8 shows the HID of the observations reported in Belloni et al. (2005) from *RXTE*, using the old state nomenclature. The track of the observations started in the lower right, in the quiescent state. The source moves up in flux steadily for 36 days, with a slight softening of the spectrum indicated by the slightly slanted line on the right side. Then it moves quickly to the left, changing spectral shape but not the count rate. Note that the constant count rate and softening spectrum show that source flux is decreasing. The transition to an intermediate state is marked by a gray line, which they determined by timing properties and the optical/IR/X-ray correlation, that showed a reversal in simultaneous observations (Homan et al. 2005a). The upper hard intermediate branch lasted about 10 days. The second transition to the thermal state (denoted soft intermediate on the graph), also determined by

timing properties, is also marked by a gray line on the left side of the top branch. Here, the system changes its hardness and luminosity wildly, making a journey back and forth across the diagram to start, before starting to decrease in luminosity and only getting slightly softer. Along the lower intermediate state (denoted again as the hard intermediate state on the graph), the hardening is almost monotonic, with the exception of a few observations of softening. During three of their observations in this region, Belloni et al. (2005) noted the hardness ratio drop back below 0.2 but with no noise in the PDS, indicating that the source was back along the left (thermal) branch (note the zigzag shape in the figure).

Now that the relevant observational information has been presented, I will attempt to explain the different states from a theoretical perspective. Plausible models currently exist for two states, hard and thermal (though the hard state is still a prime interest of study), but not for the transitions between them or for the SPL state itself. The persistence of the inner disk on the lower branch of the hysteresis curve may be indicated by the width of Fe Kα emission (if seen) and/or thermal emission, showing us that the disk may not quite truncate as it was believed to in older models (Esin et al. 1997), and that an inner disk remains on the transition to the hard state from the thermal state that eventually disappears as the accretion rate drops below a threshold value.

3. Quiescent State Observations Of V404 Cygni

Although the primary focus of this thesis is on state transitions from thermal to hard, and purely theoretical, I also include related X-ray observations of the quiescent source V404 Cyg using data from both the *Chandra* and *XMM-Newton* X-ray observatories. A first paper has been published by The Astrophysical Journal (Bradley et al. 2007) reporting the spectral results of *XMM-Newton* observations of V404 Cyg and specifically searching for spectral features in quiescence. The important parts of that paper are within this section and all the line diagnostics reported here are from this work (see Appendix I).

A second concerns reanalysis of two previous *Chandra* observations and integration of these into the total spectral energy distribution (SED), a key result that will be useful for theoretical models. This work is published as part of Hynes, Bradley et al. (2009, MNRAS, submitted). I will focus here primarily on the X-ray analysis for which I took lead responsibility. Other sections of this paper are summarized to place the X-ray observations in proper context, as the paper is part of a collaborative effort using multi-wavelength data.

3.1 Studies of the Full Spectral Energy Distribution

In Hynes et al. (2009) we present multiwavelength studies of V404 Cyg in quiescence, focusing on the SED. Radio, optical, UV, and X-ray coverage (in 2003) is simultaneous, and is supplemented by additional non-simultaneous data in the X-ray through infrared. The compiled SED in this work is the most complete available for a BHB in quiescence. The results of this work indicate that no substantial contribution from accretion light is needed from the near-UV to the near-IR, but mid-IR data indicate that a standard disk (or possibly a jet) spectrum is required. We also found no evidence of for a change in the hardness of the system (in X-rays) despite a factor of 10 difference in luminosity (between the 2000 and

2003 observations). There appeared to be no clear cut correlation between the X-ray and radio variability, pointing to the conclusion that the X-ray flux is not generated by a jet, but the break frequency of the jet (which could have been seen in the mid or far-IR) between a flat and optically-thin spectrum is not well constrained.

3.1.1 Chandra X-ray Data Reduction

The *Chandra X-ray Observatory* was launched in 1999 by NASA as a follow-on to the *Einstein Observatory*. The *Chandra* spacecraft carries a high resolution mirror, two imaging detectors, and two sets of transmission gratings. Important *Chandra* features are: an order of magnitude improvement in spatial resolution and low background (its advantages over other observatories), good sensitivity from 0.3 to 7 keV, and the capability for high spectral resolution observations over most of this range. The primary instrument we use, the Advanced CCD Imaging Spectrometer (ACIS), is an array of charged coupled devices. A two-dimensional array of these small detectors does simultaneous imaging and spectroscopy but can be vulnerable to photon pile-up. Pile-up is the arrival of more than one X-ray photon in one camera pixel or in adjacent pixels before it is read out, which affects the spectral response and the point-spread function. These are corrected for in calibration. Pictures of extended objects can be obtained along with spectral information from each element of the picture.

Data were taken from two recent *Chandra* observations of V404 Cyg, one on 2000 April 26 for 10,295 s (Garcia et al. 2001, Kong et al. 2002a), and another on 2003 July 28/29 for a total of 61,200 s (Hynes et al. 2004a). In the original set, 1587 counts were reported, while the second had 1941 counts. Both sets were reanalysed using the standard pipeline-processed level-2 data in CIAO v3.2. Source events were extracted using a 6-pixel radius aperture, with only events between 0.3–7.0 keV retained to reduce background. The background can be particularly significant for the ACIS-S3 chip, so large background regions were selected. Both data-sets utilised a 48-pixel radius circle and the background was estimated to be

Table 3.1: Best-fitting parameters for Churazov fits to *Chandra* data.

Model	N_H ($10^{22}\,\mathrm{cm}^{-2}$)	Γ	kT (keV)	χ^2/d.o.f.	0.3–7.0 keV Flux ($\mathrm{erg\,cm^{-2}\,s^{-1}}$)
2000 observation					
Power-Law	0.66 ± 0.08	1.83 ± 0.15	...	1.00	1.37×10^{-12}
Bremsstrahlung	$0.56^{+0.07}_{-0.06}$	...	$6.7^{+2.7}_{-1.6}$	1.01	1.37×10^{-12}
Raymond-Smith	0.55 ± 0.06	...	$7.3^{+2.7}_{-1.6}$	1.05	1.53×10^{-12}
2003 observation					
Power-Law	$0.75^{+0.07}_{-0.08}$	$2.17^{+0.12}_{-0.14}$	...	0.93	2.91×10^{-13}
Bremsstrahlung	0.60 ± 0.05	...	$3.97^{+0.7}_{-0.5}$	0.92	2.88×10^{-13}
Raymond-Smith	$0.65^{0.09}_{-0.07}$	...	3.29 ± 0.4	1.08	2.77×10^{-13}

approximately 4.6 counts in the source aperture for the 2003 observation, and 0.2 counts in the 2000 observation.

3.1.2 X-ray Spectra Analysis: Chandra

Spectra for both *Chandra* observations were extracted with CIAO v3.2 and were analysed with XSPEC v12.2. Response files were selected according to the CCD temperature with standard CIAO techniques. To illustrate what must be done, after selecting the source and background regions on the ACIS chip, is to create the proper response matrix file (RMF) along with the necessary effective area function file (ARF). The RMF encapsulates the mapping between the physical properties of incoming photons (such as their energy) and their detected properties (such as detector pulse heights) for a given detector. This mapping is stored in the form of a 2-D matrix, consisting of the actual energy (of the incoming photon) to detector channel mapping. Spectral fitting packages like XSPEC use this redistribution function (the matrix), plus an accompanying effective area function (the ARF, measuring the effective area of the detector vs. energy), to predict the counts per channel produced by a given spectral model for the source. In general, the response of the detector is a function of position, and the FITS file (the form delivered to the observer after NASA/ESA processing)

contains information about this embedded within it. Therefore, it is best to create our own weighted RMF and ARF files for each observation with the most up-to-date calibrations.

Data were then fitted with many spectral models within XSPEC, all with interstellar absorption, with power-law, bremsstrahlung, and Raymond-Smith models being reported in the publication (Hynes et al. 2009). Blackbody fits to the data were so poor that we neglect them for discussion. Due to the lower count rate in the 2003 observation, we were prompted to try using CASH statistics in tandem with the Churazov approximation for chi-squared statistics (Cash, 1979; Churazov, 1996). CASH statistics is a method designed to estimate the best-fit parameters using unbinned or slightly binned data, which can be particularly useful when the source yields few photons. Churazov weighting estimates the weight for a given channel by averaging the counts in surrounding channels. For each set of statistics to be used, we grouped the spectra into at least 15 counts per spectral bin; further binning results in a loss of spectral information. We also checked the consistency of CASH with unbinned data, and found the results to be equivalent.

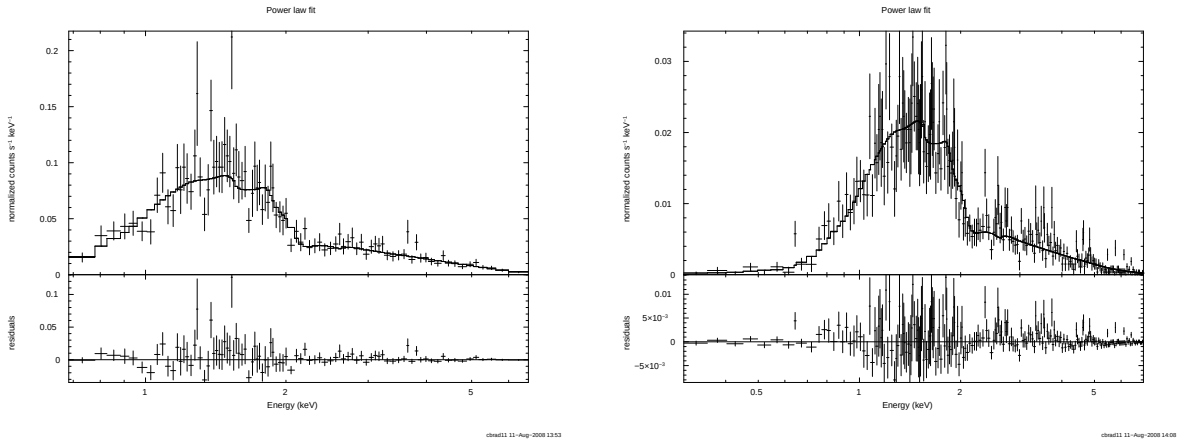

Figure 3.1: Power-law fits to *Chandra* data from 2000 (left) and 2003 (right), with residuals.

The models used for the *Chandra* reduction were models used to describe other BHB sources like V404 Cyg. Reviews of the physics of the power-law and bremsstrahlung models can be found in the introductory chapter, but essentially we do chi-square fits to the resulting

data until a minimum is found, and XSPEC reports its best parameters used in fitting. Power-law fitting gives us the N_H along the line of sight and fits the slope to the data (Γ in Table 3.1), while thermal bremsstrahlung fits a peak electron temperature. The Raymond-Smith model is that of a hot diffuse plasma in thermal equilibrium, including line emission (Raymond & Smith 1977), and it fits the temperature of the plasma to the data. The blackbody (see Ch. 1) model attempts to fit a peak disk temperature to the data, under the assumption that each concentric ring emits as a blackbody alone, without any contribution from a corona or any relativistic effects.

All models except the blackbody model give acceptable fits to both data sets with the power-law providing the best fit. Both statistical methods provide results that are equivalent to previously published results by Kong et al. (2002) for the 2000 observation. The best-fitting power-law model is shown in Fig. 3.1. For the 2003 observation, we find similar results to (Corbel et al. 2008), and a plot is also displayed in Fig. 3.1. Table 3.1 summarises the results of the spectral fitting.

3.1.3 X-ray Color-Intensity Diagram: Chandra

To see if the spectrum changes appreciably, we reran the fits with $N_{\rm H}$ fixed to a median value of the two observations with the resulting power-law indices of $\Gamma_{2000} = 1.81$ and $\Gamma_{2003} = 2.1$. To test for any variation in the spectrum with luminosity, we construct a hardness–intensity diagram. We separated the data into two bandpasses of approximately equal count rates, which were 0.3–1.75 keV (soft) and 1.75–7.0 keV (hard) for each set. To account for the reduction in sensitivity between the two epochs, we used an assumed fixed model of a photo-absorbed power-law to calculate the ratio of expected count rates in these bandpasses between the two observations and hence rescale the 2000 observations to match those from 2003. The resulting hardness–intensity diagram is shown in Fig. 3.2. We see no significant variation in hardness either within or between the two observations, the first of which had a substantially higher count rate. This indicates no detectable spectral change over a factor of ten in source

luminosity. We note that pileup was found for the 2000 observation (Corbel et al. 2008a), but this does not affect our conclusions.

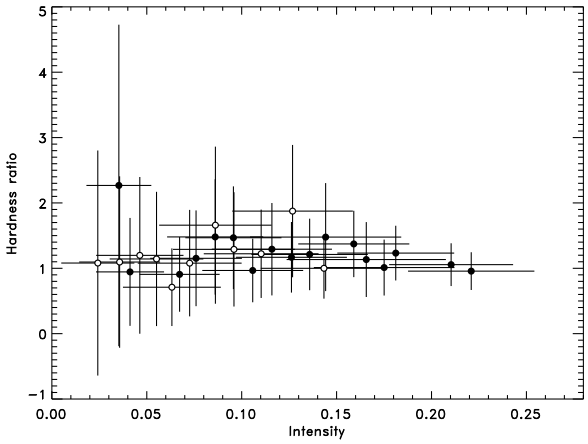

Figure 3.2: Hardness–intensity diagram from both *Chandra* observations. The two datasets were combined using the power-law model to estimate the change in sensitivity between the two epochs. Solid circles indicate 2000 data and open circles that from 2003.

3.2 Variability and Correlations

3.2.1 Radio

The VLA data presented in Hynes et al. (2009) exhibit substantial variability. Although the radio data were not within my responsibilities for this work, their connection to the X-ray data is important. We show the higher quality 8.5 GHz lightcurve together with that from *Chandra* in Fig. 3.3. The radio is clearly strongly variable and shows both large flares and dips not dissimilar to those seen by *Chandra*. The most dramatic feature rises from almost zero flux to the highest peak in about 30 min, as was also the case in the dataset presented by Miller-Jones et al.(2008a). No clear correlation between radio and X-ray is apparent to the eye, however. To further test this, Hynes et al. calculate the cross-correlation function between the X-ray and radio data and show this in Fig. 3.4. No compelling correlation (or

anti-correlation) is present, suggesting that the mechanisms for variability in the two are not connected.

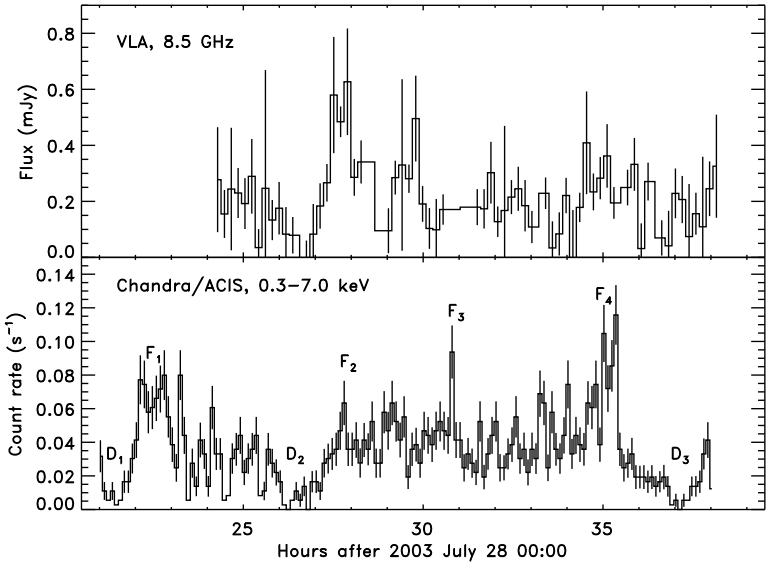

Figure 3.3: Radio and X-ray lightcurves.

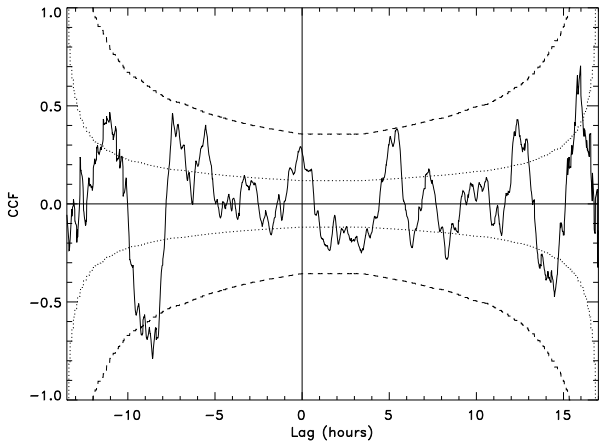

Figure 3.4: Cross correlation function of radio lightcurve with respect to the X-rays. Positive lags would indicate radio lagging behind the X-rays. Dotted and dashed lines are $1-\sigma$ and $3-\sigma$ expectations for uncorrelated variations.

Overall, the radio shows a typical flat spectrum in f_ν as is commonly seen in the hard

state of X-ray binaries (See 2.2.3 and 4.2.2). The break frequency between this flat optically-thick spectrum and the optically-thin spectrum most likely occurs in the sub-mm to far-IR area, but is not well constrained by the data. The interpretation of the radio data support the conclusion that the system has a jet that extends to 4.5 AU for an assumed distance of 3.5 kpc (Miller-Jones et al. 2008).

3.2.2 IR to UV

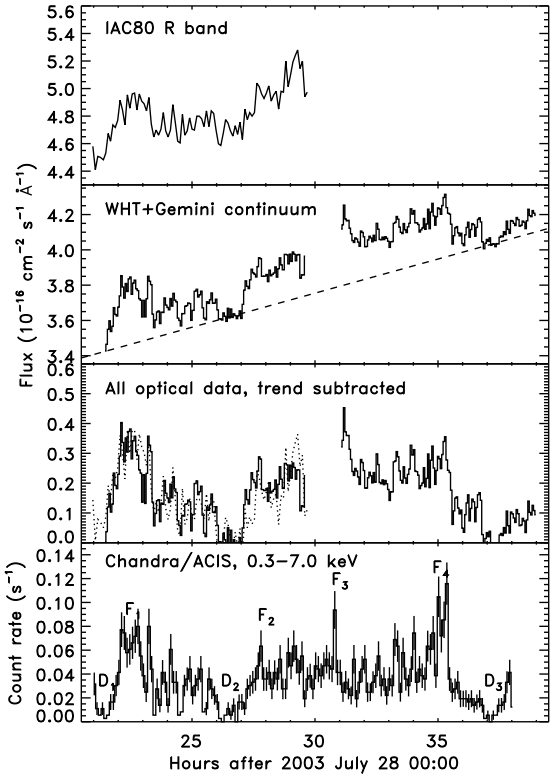

Figure 3.5: Optical and X-ray lightcurves of V404 during our simultaneous observations. The upper panels show the full flux observed by IAC80 photometry and WHT and Gemini continuum spectroscopy. The dashed line in the second panel is a linear fit to the lower-envelope. The third panel shows the WHT and Gemini continuum data after subtraction of this lower-envelope. The photometric data has been treated in the same way after re-normalising to agree with the WHT data. The fourth panel shows the X-ray data, from the 2000 observation.

The optical continuum of V404 Cyg has been seen to be significantly variable (Hynes et

al. 2004), and this variability is presumably due to disk emission. If one assumes that the lightcurve is a sum of three components: companion, and both slowly varying and flickering disk emission, then the fraction of light due to the flickering component provides a lower limit on the fraction of disk emission in the optical. Hynes et al. (2009) present simultaneous data from WHT, IAC80, and Gemini-North in Fig. 3.5. The phasing (and approximate amplitude) of ellipsoidal modulations expected are consistent with the general upward trend we observe. For a long period system such as V404, a linear approximation to ellipsoidal variations is adequate so we remove the slowly varying light by subtracting a linear fit to the lower envelope of the continuum lightcurve. We find the flickering component contributes about 4 % of the total light in both the WHT and Gemini segments of the lightcurve and correlates very well with the X-ray variations (as also found for the Hα emission by Hynes et al. 2004a). This 4 % contribution is actually not far off of estimates based on veiling near Hα. The similarity of the X-ray and continuum lightcurves, plus the fact that the flickering light alone is almost sufficient to account for spectroscopic estimates of the veiling make it plausible that flickering light source does contribute most of the disc light in the optical. Fig. 3.6 shows the UV-optical-IR SED, modeled with the stellar spectrum of a K0-III giant, which provides the best description given the observations. The view is expanded to include non-simultaneous *Spitzer* points from Muno & Mauerhan (2006) that show a mid-IR excess, and the *HST* data indicate a weak UV component is needed to properly fit the SED. The UV excess is tenuous at best, and muddled by large error bars due to uncertainties in the companion's classification, and Hynes et al. (2009) do not pursue it further.

Muno & Mauerhan (2006) interpreted the mid-IR excess seen in V404 Cyg as the tail of a Shakura-Sunyaev accretion disk (see Ch. 4, Section 2.1). This model however predicts a UV excess which is inconsistent with our *HST* observations. During quiescence instead most of the (outer) disk is expected to be in a cool state, 2000–3000 K, with a more isothermal temperature distribution (see Hynes et al. 2005 and references therein). The contamination

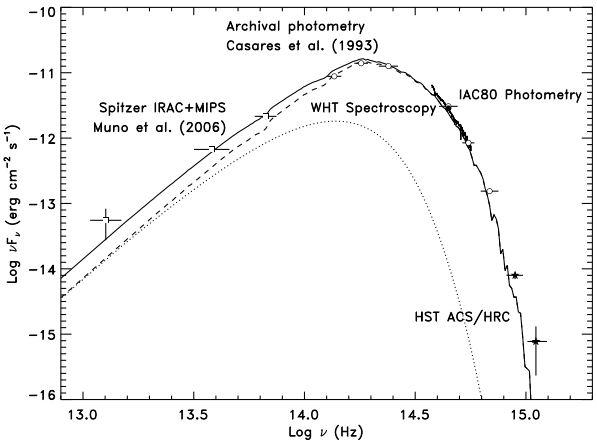

Figure 3.6: UV-Optical-IR SED. No dereddening has been applied to the data. The short solid line segment and filled symbols indicate new data, open symbols mark archival photometry. The highest frequency *HST* point has been approximately corrected for red-leak. The dashed line is a model K0 III SED reddened with $A_{\rm V} = 4.04$. The dotted line is a 2000 K blackbody component adjusted so that the sum of the two (shown with a long solid line) fits the short wavelength *Spitzer* data.

from this material will then be most pronounced in the mid-IR as it is cooler than the companion star, but no UV excess will be present.

We use a dotted line in Fig. 3.6 to show a model including a 2000 K blackbody in addition to the companion star spectrum discussed above. This can adequately fit both the near-IR to UV SED and the *Spitzer* near-IR data (it is less successful at 24 μm). The blackbody flux is consistent with a disk of radius $\sim 9\times10^{11}$ cm given the system's observed parameters (see Ch. 2). This corresponds to about 60 percent of the radius of the Roche lobe of the black hole; a very plausible size for a quiescent accretion disc. The flux of the optical flickering component falls at an intriguing location in the SED (Fig. 3.7). It is a little above a straight extrapolation of either the X-ray or radio power-laws. An extrapolation of the radio is plausible, as a flat-spectrum is expected to continue until a break to optically thin synchrotron at higher frequencies, but a straight extrapolation of the X-ray spectrum is not expected at all, and all models for the broad-band SED (e.g. Narayan et al. 1997a) involve curvature between X-ray and optical bands with humps primarily due to single and double Compton scattering of

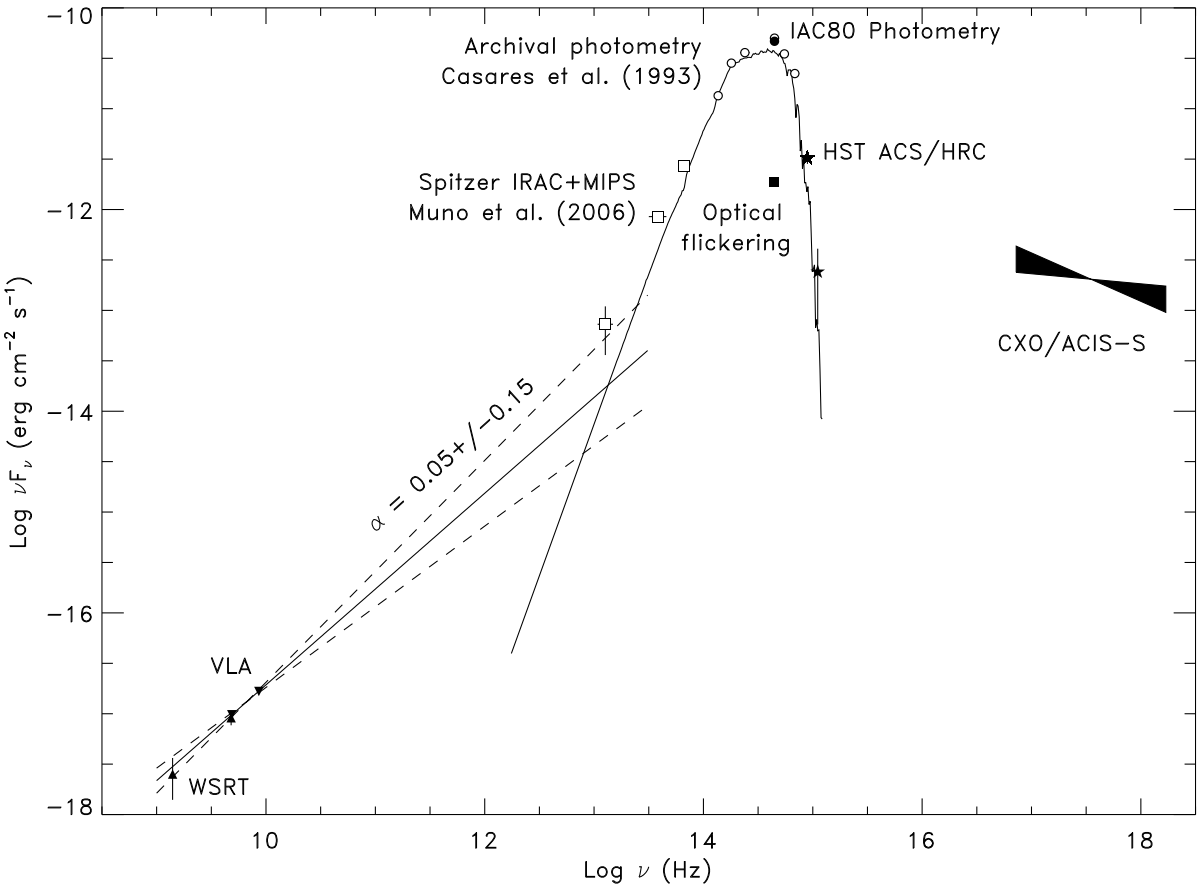

Figure 3.7: Broad band SED. Solid points are simultaneous data from our campaign, open points are non-simultaneous. Triangles are used for radio data, squares for *Spitzer*, circles for optical photometry, and stars for *HST* UV photometry. Solid lines indicate the stellar fit to the optical data and the power-law fit to the radio.

synchotron photons. Here correlations are more indicative than fluxes. We find an excellent correlation between X-ray and optical continuum (Fig. 3.5), but no clear correlation between X-ray and radio (and by extension optical). This suggests that the optical variability and the X-ray emission are closely connected, either by direct emission from the same region, as expected from early advection dominated accretion flow (ADAF) models, or indirectly through X-ray irradiation of the disc, as inferred for Hα emission (Hynes et al. 2004a).

3.3 XMM Newton Results

The *XMM-Newton X-ray Observatory* was launched by the European Space Agency in December 1999. The name comes from the type of X-ray multi-mirrors it contains. Over 170 wafer-thin mirrors are used in its 3 primary X-ray telescopes (EPIC-pn, EMOS1 & EMOS2) that are sensitive over the energy range 0.5 keV to 10 keV. Its primary advantage, compared to *Chandra* is its superior spectral coverage and resolution along with its larger effective area. While the EMOS cameras are similar to *Chandra* in spectral coverage, the EPIC-pn covers up to 10 keV with better energy sensitivity, meaning that we can investigate the presence of reflective features in the spectrum and also get full coverage of the 6-7 keV range that specifically shows the presence of the iron line.

In Bradley et al. (2007), we present more recent *XMM-Newton* observations of V404 Cyg in quiescence. Its quiescent spectrum can again be best fitted by a simple power-law with photon index $\Gamma \sim 2$. The spectra are consistent with those expected for the advection-dominated accretion flow, and are the highest quality quiescent spectra yet obtained. V404 Cyg was roughly equal in luminosity compared to the previous observation of *Chandra* in 2003. We saw variability of a factor of 4 during the observation. We saw no evidence for the presence of fluorescent or H-like(6.4)/He-like(6.7) iron emission, with upper limits of 52 eV and 110 eV respectively. The limit on the fluorescent emission was improved by a factor of 15 over the previous estimate, and the restriction on H-like/He-like emission is lower than predicted from models by a factor of 3.

3.3.1 XMM Observations and Data Reduction

V404 Cyg was observed by *XMM-Newton* on 2005 November 8-9. The observation lasted 40ks. The three EPIC cameras were all active during the observation: pn, EMOS1, and EMOS2. All were operated with a medium filter (which protects the CCD from other wavelengths it may be sensitive to) and full window mode. In this case the medium filter

was chosen to prevent contamination from point sources in the ranges of magnitudes from 6-9. Full window mode simply means that the entire CCD was read out, which is necessary for low-flux sources. Total background corrected counts from the three cameras are given in Table 3.2. For the paper (Bradley et al. 2007) we analyzed standard pipeline-processed event files with SAS v6.2.0. In order to study the temporal behavior of V404 Cyg we accumulated its pn lightcurve in the energy range 0.3-10 keV. The EMOS camera analysis is restricted to the 0.3-7 keV range. Corresponding backgrounds were taken from the same chip as the source but far enough away from it so as to not be affected by the wings of the point spread function, with an extraction radius of 16 pixels in pn and in MOS. These lightcurves show variability of a factor of 4 in count rate within 10ks, and a large amplitude flare is detected at the very beginning of the run with a duration of about thirty minutes. We measured a

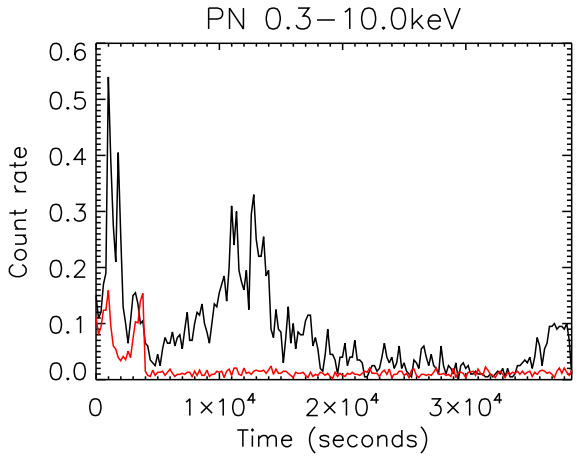

Figure 3.8: PN camera lightcurve, source and background, binned at 200s. Reproduced with permission of the AAS.

source count rate of 0.035 s^{-1} for pn and an average of 0.012 s^{-1} for the two EMOS. The spectra could be fit best by either a power law or bremsstrahlung spectrum, with results reported in Table 3.2.

3.3.2 Continuum Spectral Analysis: XMM-Newton

Spectra were extracted with XMMselect (a canned extraction program) and were analyzed with XSPEC v12.2 [1] and we report those results here. Bin sizes in extraction were 5 counts/channel for pn and 15 for the EMOS cameras, as suggested in the *XMM-Newton* Users Guide [2]for optimal use of the standard response matrices. Single and double events were included under extraction for pn, and all valid events were kept for EMOS. Response files were made using XMMSelect pipeline tools to check against the standard version, with consistent results for the spectral fits from both. Further spectral analysis was done between 0.3-10 keV for pn and 0.3-7 keV with MOS. As in Hynes et al. (2009) we have chosen to use

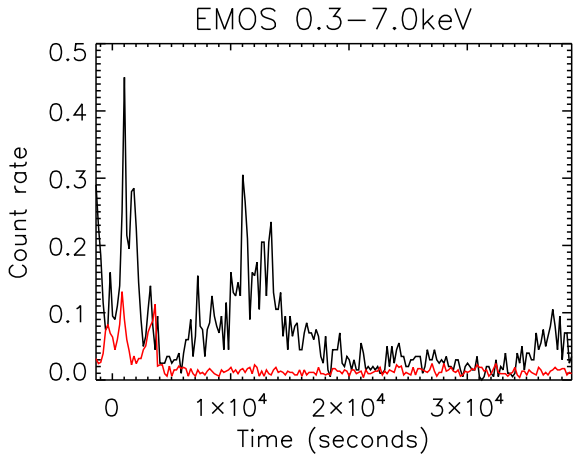

Figure 3.9: Summed EMOS lightcurves with background, binned at 200s. Reproduced with permission of the AAS.

χ^2 Churazov-weighted statistics (Churazov 1996) in our analysis, since we feel these to be more applicable when line diagnostics are to be done, because of the relatively low counts around the iron line energy. CASH statistics (Cash 1979) were used as a check. For this we used lightly binned data (5cts/bin) for χ^2 statistical fits. We then fit the data with many single-component spectral models such as power-law, thermal bremsstrahlung, Raymond-

[1]http://heasarc.gsfc.nasa.gov/docs/xanadu/xspec/index.html
[2]http://xmm.esac.esa.int/external/xmm_user_support/documentation/sas_usg/USG/USG.html

Table 3.2: Best–fit parameters for power–law and bremsstrahlung models

Instrument	Model	N_H ($\cdot 10^{22}$ cm^{-2})	Photon Index	kT	χ^2_ν/dof	f_X (0.3–10keV)^a (erg cm^{-2} s^{-1})	counts
pn	PL	0.86 ± 0.7	2.10 ± 0.10	–	0.75/115	1.04×10^{-12}	1404
	bremss	$0.69^{+0.05}_{-0.02}$	–	$4.88^{+0.73}_{-0.6}$	0.77/115	4.67×10^{-13}	
EMOS1	PL	0.859 ± 1.2	2.04 ± 0.18	–	0.96/48	1.06×10^{-12}	497
	bremss	$0.67^{+0.1}_{-0.08}$	–	$5.40^{+1.9}_{-1.25}$	1.01/48	4.33×10^{-13}	
EMOS2	PL	0.927 ± 1.3	2.06 ± 0.18	–	0.92/47	1.12×10^{-12}	519
	bremss	$0.75^{+0.1}_{-0.09}$	–	$4.91^{+1.72}_{-1.09}$	1.05/47	4.21×10^{-13}	

NOTE - Errors are at 90% c.l. for a single interesting parameter; ^{a}unabsorbed flux; flux is in 0.3-7 keV range for MOS

Smith (1977), and blackbody, including interstellar absorption. A broken power-law model was tried with data from the onboard pn camera, but fits were poor to EMOS1 and EMOS2 data. Fits to many other single and multiple component models within XSPEC were tried, but in those cases the error bars on fitted parameters were unreasonably large or the fit was too poor. The best-fit parameters for each of the three cameras used, by both CASH and χ^2 statistics, are consistent between the two fitting methods and only χ^2 results are reported herein. The quoted errors on the derived model parameters correspond to a 90% confidence level.

Only two of the models reported give statistically acceptable fits to the data ($\chi^2/\nu \lesssim 1$). The power-law model provides the best fit to the data, and yields parameters consistent with previous observations (e.g. $\Gamma \sim 2.0$; see Table 3.2), and was then used for line diagnostics. Bremsstrahlung is also acceptable, while Raymond-Smith and blackbody model fits are rejected. This best fitting model is shown in Figures 3.10 and 3.11.

The pn and EMOS spectra give consistent fit parameters with quoted uncertainties (see Table 3.2). Although the exact value of the absorption is still subject to some uncertainty, all our data point to a power-law spectrum with photon index $\Gamma \sim 2$. In the following analysis, we aim to constrain the possible presence of the iron line at 6.4-6.7 keV and consider only the pn spectra, due to the higher statistics at high energies.

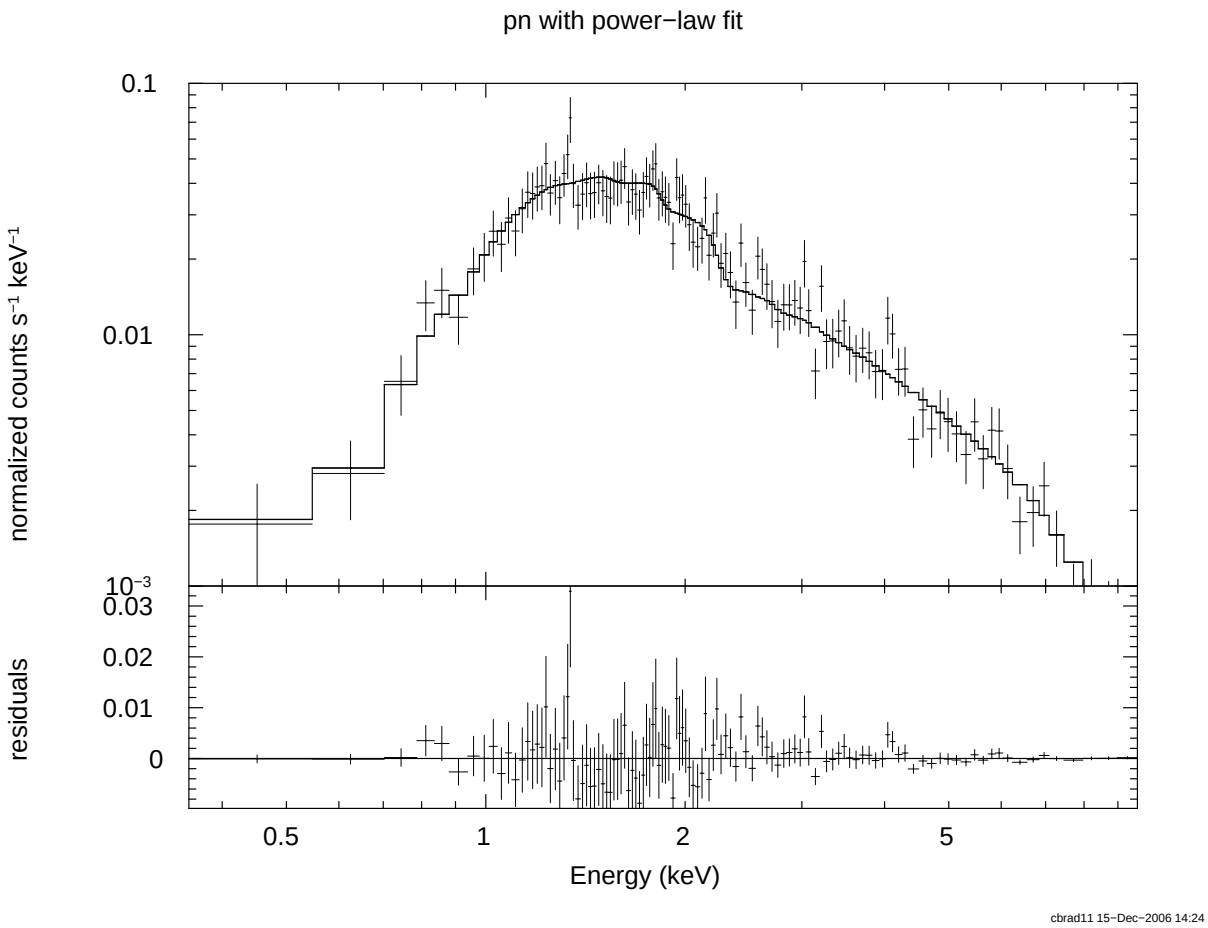

Figure 3.10: Comparison of the PN spectrum with the best–fit power–law model. In the lower panel the residuals between data and model are shown, binned for visual clarity

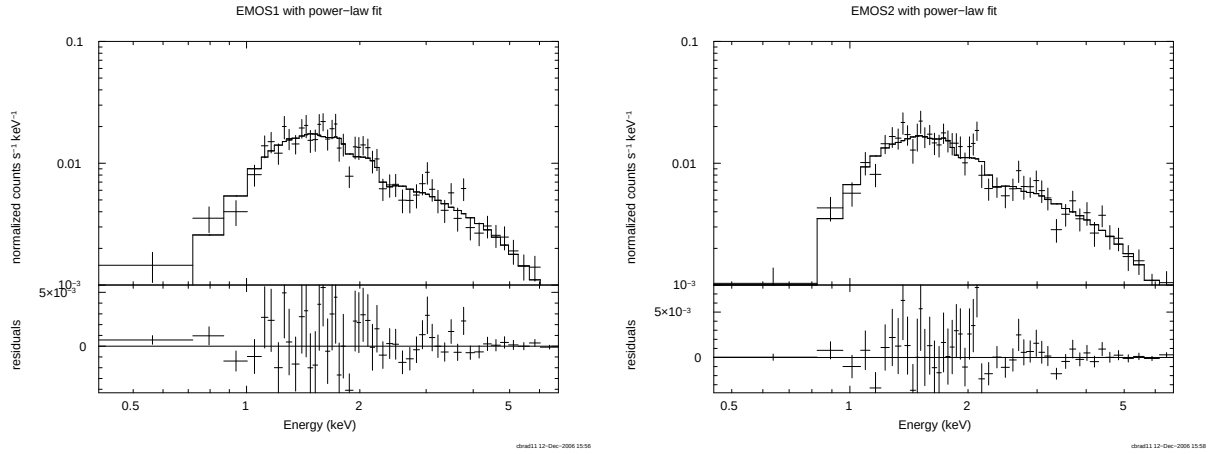

Figure 3.11: EMOS 1 and 2 spectrum, 0.3–7 keV

3.3.3 Line Diagnostics

The earliest examples of iron line emission studies pertain to AGN, where the 6.4 keV line profile is sometimes quite easily seen and very prominent. *ASCA* studies of MCG-6-30-15 (Tanaka et al. 1995) show a very prominent 6.4 emission line, while the work of Yaqoob & Weaver (1996) showcase prominent lines from six AGN, for example. More recent, higher resolution work using *Chandra* and *XMM-Newton* find them in many more systems (Yaqoob 2003).

The best studies of iron line emission in binaries before the launch of *Chandra* (July 1999) and *XMM-Newton* (Dec. 1999) were targeted at GRS 1915+105 (Hard/SPL state, with $\sim$ 250 eV; Martiocchia et al. 2002). Fits from *BeppoSax* data implied a truncated accretion disk, thus giving no evidence of black hole spin (consistent with later results from *XMM*; Martiocchia et al. 2006). The higher ionization state in the inner disk in this system may inhibit detection of any spin however. Similar features have been detected in other X-

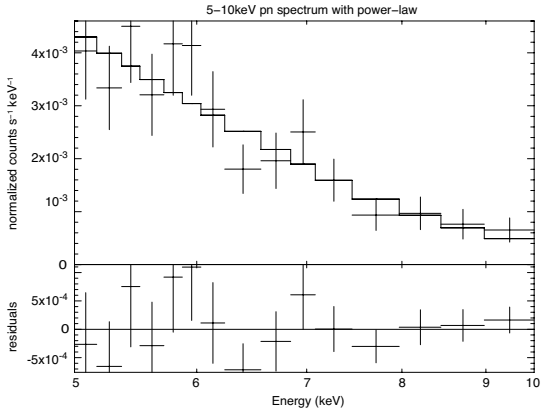

Figure 3.12: pn spectrum in the iron energy range of 5-10 keV, with powerlaw model overlaid

ray binaries, usually but not exclusively in BH transients (neutron star systems Ser X-1 and GX 3+1 were observed to contain iron lines at roughly 300eV equivalent width; Oosterbroek et al. 2001). A few recent examples of stellar-mass BH cases are XTE J1650-500 (SPL state, with $\sim$ 250 eV EW; Miller et al. 2002), SAX J1711.6-3808 (SPL state, with $\sim$ 2.6 keV

EW; In't Zand et al. 2002b), and XTE J2012+381 (Hard/SPL state, with $\sim$ 1.2 keV EW; Campana et al. 2002). See also Miller (2006) for a recent review.

For the line diagnostic work, only *XMM-Newton* data is used, since *XMM-Newton* has superior spectral resolution, much better energy sensitivity, and we have better statistics for this observation. Our spectral analysis of V404 Cyg using *XMM-Newton* data shows no evidence for a narrow 6.4 keV iron line. From adding a simple gaussian component to the best-fitting model, (fixed width 0.1 keV) we establish an upper limit of $\sim$ 52 eV for this line, well below all previous estimates ($\sim$ 800 eV, Kong et al. 2002). We then reran this using CASH statistics, and find the results to be consistent.

Prompted by predictions of emission in Narayan & Raymond (1999), we then test-fitted a 6.7 keV gaussian (from He-like Fe XXV) to the spectrum, and detect no significant emission there either with an upper limit of $\sim$ 110 eV (0.1 keV fixed width) on the feature. The total group of Fe XXV widths in Narayan & Raymond's paper sums to roughly 300 eV, a factor of about 3 above our results. A close-up of the 5-10 keV region of the spectrum is presented in Fig. 3.12.

There are some features seen in the spectrum of V404 Cyg in this result that may indicate the presence of line emission at just above 4 keV. This line corresponds to a line predicted from Ca XIX/XX in Narayan & Raymond (1999). We again added in a gaussian line component (allowing the energy to vary) to the power-law fit at an energy of 4.08 keV (Ca XX Lyα), and find a fitted equivalent width of $\sim$ 117 eV, well above the 2.7 eV equivalent width predicted in their paper, for a model with wind outflows. The 90% confidence error on the equivalent width is from 0.04-0.21 keV.

3.3.4 Discussion of Results

One would expect 6.4 keV fluorescent emission from the presence of cold material near the X-ray emitting region, or an extended emission region above the disk that illuminates cold material below. Also, the presence of a Compton reflection bump in the spectrum

at around 10 keV would indicate higher reflection of this extended region off the cold disk. *XMM-Newton* cannot adequately constrain the presence of a 10 keV feature, but no evidence has been seen for either of these reflective features. This constrains the reflection fraction considerably and could indicate that there is no cold matter near the X-ray emission region. George and Fabian (1991) proposed a model in which the X-ray source was located at a height above the central region of a standard disk, for a semi-isotropically and isotropically illuminated cold slab (without rotation), and calculated equivalent widths of the Kα line for varying inclinations (relative to the observer) and incident power-law indices. In this context, semi-isotropic is meant to represent numerous scattered "clouds" or "blobs" of gas orbiting the hole instead of a normal thin disk, whereas an isotropically illuminated disk is exactly that. Their predicted width for the 6.4 keV feature was $\sim 110 - 120$ eV, a factor of 2 higher than our restriction on the upper limit (see Figure 14 of their paper). The lack of the 6.4 keV line at any width forces us to abandon this particular simple geometry of an X-ray source above a cold slab. In this context, the X-ray emitting region must be more compact and close to the black hole. The lack of neutral Kα would also seem to disfavor the Nayakshin & Svensson model (2001) for this system because their emission comes from large radii, where there should be a cold thin disk present, so we would expect a narrow line to be present. The Nayakshin & Svensson model has other difficulties as well, such as higher luminosity predictions than what are observed for quiescent BH systems. At these luminosities we would expect some signature of 6.4 keV emission.

We would expect Fe XXV Kα emission at an energy of 6.7 keV from a hot coronal/ADAF flow with high collisional rates. The lack of any such 6.7 keV line emission may point back to earlier ADAF models of Comptonized thermal synchotron emission within a small region close to the black hole. Such a small emitting region would also fail to properly illuminate the disk surface to achieve significant 6.4 keV emission.

In particular, one of the ADAF models with moderately strong outflows presented in Narayan & Raymond (1999) is ruled out. This model consisted of what is basically a

Raymond-Smith plasma with a Compton component added in. In that paper it was suggested that the equivalent width of lines correspond to the size of the ADAF region, and that for a given size the widths increase with outflow strength. Lower accretion rates would lead to increased bremsstrahlung emission, and equivalent widths increase. A bremsstrahlung model fit to the data is statistically acceptable, but we see no lines, the most prominent of which should have been at 6.7 keV. Based on this paper, our results would indicate that V404 Cyg is a Compton-dominated system with a weak outflow, if one is present, or that the electrons are not recieving a significant fraction of the dissipated heat in the flow. The strongest X-ray line emission occurs for $T_e \sim 10^7 - 10^8$ K, suggesting that the source of the X-ray emission is above this temperature. A model of hot optically-thin plasma emission in ionization equilibrium (Raymond & Smith 1977) is also ruled out by the combination of our results with those previously published (Kong et al. 2002).

Absence of any iron line emission whatsoever may instead indicate that the system is underabundant in iron, all the material present in the X-ray emitting region is completely ionized, or perhaps that resonant trapping is efficiently eliminating any line emission (Matt et al. 1993, 1996). The absence of any Fe line is not likely to be caused by underabundance because a strong Fe line feature with an equivalent width of 130-150 eV was detected in outburst (Oosterbroek et al. 1996). There is little evidence for peculiarity of abundances in V404 Cyg aside from a higher than expected lithium abundance in the companion (Casares et al. 1993, Casares & Charles 1994, Martin et al. 1992) which may be associated with the ADAF (Yi & Narayan 1997), although other Li production scenarios have also been proposed (e.g. Martin et al. 1992). A hole in the disk filled with an ADAF would explain the absence of cold material, but we may still expect reflection. The presence of a central ADAF should diminish the strength of any reflective feature (Gierlinski et al. 1997) but not necessarily push it to zero (Miller et al. 2002).

The possible calcium line at 4.08 keV is intriguing, although this is not a secure detection. Ca-44 could be produced as a secondary decay product of Ti-44 (half life of $\sim$ 86

years), which is produced in a supernova explosion (Theiling & Leising 2006), however this system's supernova could not have been recent enough for an overabundance to remain, and no overabundance is seen in optical spectra. Other explanations for higher abundances of calcium have been proposed in the context of nucleosynthesis within thick accretion disks with very low viscosity (Arai & Hashimoto 1992, note Fig. 4; Mukhopadhyay & Chakrabarti 2000, Jin, Arnett & Chakrabarti 1989).

V404 Cyg remains a prime candidate for the ADAF model, and our results argue against models of a corona above a thin disk or the presence of any standard thin disk close to the black hole. We place stringent new upper limits (52 eV) on the presence of a 6.4 keV line from neutral iron. Previous upper limits on the equivalent width of the 6.4 keV iron line emission were found to be $\sim$ 800 eV (Kong et al. 2002), an improvement by a factor of 15. The lack of reflective components in the spectrum shows that the emitting region is not illuminating the inner disk efficiently, or that it simply is not present. This result statistically rejects all fitting models considered with the exception of power-law and bremmstrahlung emission. Our results are consistent with the interpretation of a truncated accretion disk, within which a diffuse quasi-spherical coronal/ADAF flow exists and attempts to cool itself by optically-thin emission. We also place a strong limit on ionized iron emission at 6.7 keV. The lack of strong lines argues against strong outflow/wind in the framework of the ADAF model, where lower accretion rates corresponds to an enhancement on the bremsstrahlung emission and lines' widths. We know however from radio observations that V404 Cyg does power a synchotron emitting outflow (whether this comes from the innermost region or not is not known)(Gallo, Fender, & Hynes 2005). Models like the adiabatic inflow/outflow (Blandford & Begelman 1999) allow for a significant fraction of the outer material to be lost to an outflow at large radii. Unfortunately though, they do not make exact predictions of the spectral energy distribution to compare the spectra with. In fact, comparison with the Narayan & Raymond model (1999) seems to favor a spectrum produced by Comptonized synchrotron emission without winds.

4. Theoretical Background

In this chapter, highlights of the theoretical picture of the different observational states along with various relevant models will be given. First I will define a key concept called the Eddington limit, then highlight some of the problems with the standard disk model when applied to these systems, particularly in quiescence, and the motivation of the advection-dominated accretion flow model (ADAF; see Narayan 1998 for a review). Afterwards the process behind formation of the ADAF flow will be discussed, and this leads into the published work for this dissertation.

Different solutions of accretion onto compact objects have been investigated in the past for various disk geometries. The description of an optically-thick, geometrically thin disk, now called the "standard thin disk model," dates to work of Shakura & Sunyaev (1973). A much hotter self-consistent solution of optically thin gas was discovered by Shapiro et al. (1976), but found to be thermally unstable by Piran (1978). Solutions where the large optical depth of the inflowing gas prevents the escape of radiation have been studied by Abramowicz et al. (1988). This is actually a subset of the advection-dominated accretion model. Another solution concerns accretion at very low rates also proposed first by Shapiro et al. (1976; Ichimaru 1977; Rees et al. 1982). Detailed work on this solution began again with Narayan & Yi (1994, 1995a,b) and others (Abramowicz et al. 1995; Chen et al. 1995; Narayan et al. 1997) that is relevant for accretion in many cases, but was specifically applied to X-ray binaries. In this chapter, I will highlight some of these solutions as applied to BHB systems.

The large diversity of light curve features for black hole binaries has been covered extensively by Chen et al. (1997) and McClintock & Remillard (2006), with only a few sources showing the "fast rise - exponential decay" pattern predicted from the standard thin disk model. The diversity of spectral observations drives the appearance of new, more compli-

cated models to explain them and the transitions between them. Most show a very complex pattern (Gierlinski & Newton 2006). Two issues are believed to create this variety of luminosity and spectral states: (1) The outburst is probably caused by the ionization instability (See Section 4.3; Cannizzo & Reiff 1982; Canizzo et al. 1995), like the dwarf novae outbursts (Osaki 1974). The mass flow in the disk in this disk instability model (DIM) is related to the spread of heating and cooling waves initiating changes in the disk structure between hot and cold states. The larger disks in BHBs together with the effect of X-irradiation lead to a more complex flow pattern in mass flow and outburst light curve. (2) The mass flow rate in the disk resulting from the outburst behavior is the key parameter that determines the mode of accretion, high flow rates via an accretion disk everywhere (thermal state), and for lower rates a truncated disk and inner ADAF (hard state).

4.1 The Eddington Limit

The basic idea behind accretion is the following: When a mass (M) falls from infinity to distance (R), in the gravitational field of a massive compact object, (M_c), it gains the kinetic energy $E = (GM_cM/R)$. If this is converted into radiation with some efficiency ϵ, then the luminosity of the system will be $L = \epsilon(dE/dt)$. In the context of neutron stars we expect a mass range of (1.4-3 $M_\odot$) with black hole masses covering the range above that. For material accreting onto a compact object, the accretion luminosity will be proportional to the accretion rate, $\dot{M}$.

$$L_{\rm acc} = \epsilon \frac{GM_c\dot{M}}{R} \tag{4.1}$$

There is, however, a natural bound to the luminosity generated by accretion. The photons emitted as the gas heats up will be continuously interacting with in-falling particles and will exert a force on ionized gas. When that force becomes equal to the gravitational force towards the compact remnant, the accretion will effectively stop. The number density $n(r)$ of photons crossing a sphere of radius r, centered at the accreting object of luminosity L is,

$(L/4\pi r^2)(h\nu)^{-1}$ where ν is some average frequency of the photons and h is Planck's Constant. The rate of collisions will be $n\sigma_T$ (where σ_T is the Thomson scattering cross-section), and each collision transfers momentum, $(h\nu/c)$. Because of the Coulomb coupling, this energy will transfer to protons which will effectively push away the accreting gas.

The force balance between radiation and gravitation is

$$\frac{L\sigma_T}{4\pi c r^2} = \frac{GM_c m_p}{r^2} \tag{4.2}$$

so the radiation force will exceed gravity if the luminosity reaches a level $L_{\rm Edd}$:

$$L_{\rm Edd} = \frac{4\pi G M_c m_p c}{\sigma_T} \tag{4.3}$$

Note that this derivation assumes spherical and steady accretion, so it is only best to use as an order of magnitude estimate for the limit of accretion (see e.g., Heinzeller & Duschl 2007). In general σ may be higher for partially ionized gas coupling to lines. Also, this derivation assumes pure hydrogen as the accreting matter (one electron per nucleon). Heavy elements would raise this to one electron per two nucleons, and taken together this raises the luminosity limit.

4.2 Theoretical Picture of the Different X-ray States

4.2.1 Thermal State

For the thermal state we have a satisfactory paradigm, thermal emission from a geometrically-thin accretion disk. Observations and magnetohydrodynamic (MHD) simulations continue to improve our understanding of the physics involved.

The best known hydrodynamic model of radiating gas in the gravitational well of an object is the steady-state thin disk model (Shakura & Sunyaev 1973; Lynden-Bell & Pringle, 1974; Pringle 1981). The primary feature of this model is a prescription for the viscosity that transports material inwards and angular momentum outwards. The Shakura-Sunyaev model made an ad hoc scaling assumption for the relationship between viscous stress and

pressure (the so-called α-prescription).

$$\tau_{R,\phi} = \alpha P \tag{4.4}$$

This allows us to describe the viscosity, ν, in relation to the sound speed (c_s) and vertical thickness (H) of the disk:

$$\nu = \alpha c_s H \tag{4.5}$$

where $\alpha < 1$ because hydrodynamic turbulence must be subsonic. This is just a parameterization, and we have folded all our ignorance of the relevant physics into α, which in general could be a function of disk height, accretion rate, primary mass, and radial distance from the compact object.

In the simplest approximation, this accretion disk model leads to a temperature profile, $T_{\rm eff} \sim R^{-3/4}$, independent of disk viscosity, that forces the conclusion that the disk dominates the observed spectrum (compared to optically-thin emission), which will be thermal in nature.

Observationally, systems in the thermal state are fit best by a classical multitemperature disk model (Mitsuda 1984), which essentially is a sum of each ring of material's own blackbody spectrum, assuming a constant accretion rate throughout. However, this model ignores several key effects and the spectral parameters derived cannot be interpreted literally. It neglects the physically-motivated torque free inner boundary condition at the ISCO (Gierlinski et al. 2001). It also ignores the sizable effects due to GR and radiative transfer (Zhang et al. 1997). Newer models for Kerr black holes are now available (Li et al. 2005; Davis et al. 2005), which have fully-relativistic treatments.

MHD simulations are now extremely important in understanding the viscosity in accretion disks, and this applies to all states of accretion seen in X-ray binaries, not solely the thermal state. The magnetorotational instability (MRI) is now a prime source of turbulent viscosity (Balbus & Hawley 1991), and is confirmed in GR MHD simulations (McKinney & Gammie 2004). The MRI is a fluid instability that comes about when the angular velocity

(rather than the angular momentum) of a magnetized fluid element decreases as the distance from the rotation axis increases. This criterion is met in most accretion disks, and so a torque is created which transports angular momentum outwards, while supplying matter inwards. It is also referred to as the Velikhov-Chandrasekhar instability (Velikhov 1959; Chandrasekhar 1960) or the Balbus-Hawley instability in the astrophysical literature.

A rather simple model will illustrate the main effect. Consider, for example, a rotating disk in the presence of a weak poloidal magnetic field. Two radially neighboring fluid elements would behave as two mass points connected by a spring, with the tension in the spring playing the role of the magnetic tension. In a simple disk described above, the innermost radial element orbits the compact object faster than the outer, which causes that spring to stretch. This tension forces the inner element to slow down, which reduces its angular momentum, and then it can move to a lower orbit (closer to the compact object). The outer element has its angular momentum increased by the amount the inner element lost, speeds up, and moves to a higher orbit. The spring tension increases as they move apart further, and the process runs away.

Hopefully with the inclusion of radiation the groups working on the subject can connect more directly with observations. Their simulations have now produced refined values of α appropriate to simulate the effects of MHD in this work and others (see Balbus 2003 for a complete review).

4.2.2 Hard State

XTE J1118+480 is a peculiar system in that it is never seen to go through a hysteresis of states, and it stays in the canonical hard state (optically-thin emission dominates, usually as a power-law), and only its luminosity and spectral index varies. This source gives the best determination of the temperature and radius of the accretion disk because of its very low interstellar attentuation (only 30% at 0.3 keV). Using simultaneous *HST*, *EUVE*, and *Chandra* observations (McClintock et al. 2001), the inner edge of the disk in source XTE

J1118+480 was found to be very large ($\sim 100\ R_g$) and cool (~ 0.024 keV) in the hard state. Though the blackbody emission seems truncated, due to fits of a multicolor disk model to the data, the nature of the gas within that radius is uncertain. Observations of this system and others like it led to the formation of the advection-dominated accretion flow model in the mid 90's (ADAF; Narayan & Yi 1994, 1995; Esin et al. 1997), as well as models of optically-thin jet emission (Markoff et al. 2001), and radiative transitions in a Compton corona (Frontera et al. 2003). The last of which would need to be optically thick enough to mask the ~ 1 keV thermal emission from the disk, however. Such a corona could also be a hot wind leaving the disk (Blandford & Begelman 1999, 2004). Currently, the application of the ADAF model to the hard state is the most commonly cited explanation for the accretion behavior in the system (Esin et al. 2001), and this model proposes that the material (which would intuitively be within a disk) is still present, but at densities so low that it cannot radiate efficiently (see Section 4.4).

The fact that black holes have an event horizon makes the inner boundary condition different from that of a normal star, and allows a family of mathematical solutions where a significant amount of material can be transported through the event horizon without radiating away all its energy. In a neutron star system, this material would hit the surface and would have to be reprocessed and its energy radiated. Thus, a system with an ADAF flow would have a lower luminosity for a given accretion rate with a black hole primary than with a neutron star primary.

These low radiative efficiencies could occur either because the gas has low density and is unable to cool, or because the accretion rate and density are so high that the radiation is effectively trapped in the gas. The former is sometimes called an ion-supported accretion flow (ISAF) and the latter a radiation-supported accretion flow (RSAF). ISAFs are the case of interest in the hard state, as it is suspected that these have very sub-Eddington accretion rates, so the energy could remain in the ions because the coupling between electrons and ions is weak at low densities, leading to a two temperature plasma. The disk would be truncated

at a radius beyond the ISCO, in agreement with the ADAF model. The RSAF case could have an Eddington accretion rate, but the radiation would be efficiently trapped so as to produce a sub-Eddington luminosity, this case does not appear to be relevant for LMXBs but could be applicable to AGN. Treatment of "slim disk" solutions like the RSAF flow was best done by Abramowicz et al. (1988).

The adiabatic inflow/outflow solution (ADIOS) proposed originally by Blandford & Begelman (1999) points out flaws in the original ADAF models, namely that as a result of the assumptions made, the gas has a positive Bernoulli parameter (sum of internal energy, enthalpy, and gravitational energy) and so is unbound. They propose that ADAF solutions be modified to include large scale wind outflows that carry away mass, angular momentum and energy from the accreting hot gas. Thus, the amount of matter actually transported through the event horizon is far smaller than that which is supplied through the L_1 point. The ADAF solution, in its simplest self-similar form has some other problems as pointed out by Blandford & Begelman (1999). The case of $\gamma \sim 5/3$ (where γ is the specific heat) is a singular case and forces the solution to be non-rotating, which Narayan & Yi (1994) avoid by saying that the magnetic energy density is comparable to the ion energy density so that the true value of γ is between 5/3 and 4/3 (the case where magnetic energy is dominant). However simulations by Balbus & Hawley (1998) show that the magnetic energy density should be maintained below equipartition values, and in this case $\gamma \sim 5/3$. This forces Ω to be well below the Keplerian values, meaning the ADAF flow should be slowly rotating. For weakly magnetized flows to work with ADAF solutions, the gas would have to lose much of its angular momentum at large radii, which would be likely to unbind the gas. Blandford & Begelman found that lowering γ from 5/3 only exacerbates the problem with the Bernoulli parameter because torque transports both angular momentum and energy, and in steady state those must be conserved. At present, the conclusions of the basic ADAF models with the ADIOS model seem incompatible. More advanced models will be required to clear up the ambiguities within them.

4.2.3 Steep Power Law State

In a simplistic sense, it is best to think of this state as being an amalgam of both the hard and thermal states. This means that this state must involve both disk and coronal emission, but is not covered by our published work. Here, the PL component steepens and strengthens, while the disk luminosity remains soft (but at high temperature) and is always apparent. To gain understanding of this state, models must account for high-frequency QPOs, extremely high luminosity, and hard spectra that extend up to 1 MeV. Most of them contend that inverse Compton scattering is the radiating mechanism (Zdziarski & Gierlinski 2004). MeV photons suggest that the scattering occurs in a nonthermal corona, which has been modeled as a slab using seed photons from an underlying disk (Zdiarski et al. 2005). Bulk motion Comptonization has been proposed for material converging on the black hole (Titarchuk & Shrader 2002), along with models with more complicated geometry with feedback mechanisms like flares that erupt from magnetic instabilities in the disk (Poutanen & Fabian 1999).

Analysis of *RXTE* observations of GRO J1655-40 and XTE J1550-564 show that as the PL component steepens and strengthens, the disk luminosity and inner radius decrease while maintaining a high temperature. This could be interpreted as observational confirmation of strong Comptonization of disk photons in this state (Kubota & Makishima 2004). At this time, however, a good theoretical model of the behavior seen in this state does not exist.

4.3 Possible Root Cause of State Changes

While each state is studied on its own and has several key characteristics to differentiate it from the rest, the root cause of the (sometimes rapid) state changes is generally assumed to be related to the conclusions of the Disk Instability Model (DIM), although the hysteresis of states itself points to another parameter being involved (possibly the size of the disk, yet we believe this is ultimately defined by the accretion rate as well). The pertinent reviews of

the model as applied to cataclysmic variables and X-ray transients have been compiled by Lasota (2001) and Done, Gierlinski, & Kubota (2007) respectively.

A Shakura-Sunyaev disk is unstable thermally and viscously for temperatures near that associated with the ionization of hydrogen, $10^{4-5}K$. The opacity is low for nearly neutral, cold material, much lower than predicted by free-free processes as the electrons are bound (Cannizzo & Reiff 1982). However in this temperature range it increases steeply, so that a very small temperature increase of the accreting gas produces a huge increase in opacity as the highest energy photons on the Wien tail of the thermal distribution are able to ionize some of the hydrogen in the disk. This means that these photons are absorbed, so their energy remains in the disk, increasing its temperature. More photons ionize more hydrogen, causing a thermal runaway which only stops when all the hydrogen is almost completely ionized.

This thermal instability triggers a viscous instability, as the increased temperature means an increased accretion rate, because the viscous stress is proportional to pressure in this prescription (see Eq. 4.4). This new accretion rate is larger than the input rate (from the neighboring outer annulus), so the material in the disk is eaten away at this radius. The pressure will decrease, so the heating will decrease, and the temperature decreases until hydrogen can recombine. This triggers another thermal instability, with the cooling now becoming a runaway process until almost all the hydrogen is neutral again. This forms a cycle of instabilities that can change the accretion rate.

This description of the limit cycle of hydrogen is a purely local description (in a given radial zone), however, the discontinuous jump in temperature (and accretion rate) means that it affects the neighboring annulus of the disk. This has a global impact on the disk structure if the difference between the accretion rates between ionized and neutral annuli are large. The entire disk could then undergo a limit cycle instability, varying between a Shakura-Sunyaev disk with large accretion rates (e.g., the thermal state), to a quiescent disk where H is neutral almost everywhere, but with an accretion rate that decreases as the

radius decreases (because it has constant temperature) similar to the hard state quiescent outer disk.

Lasota (2001) explains the DIM as follows, specifically applied to white dwarf systems. The quiescent disk builds up from steady mass transfer from the companion. Eventually this material becomes hot enough to trigger the thermal instability at some radius. The increased accretion rate continues through the next inner annulus, increasing its temperature and causing the thermal instability to continue within it. This results in a heating wave that propagates through the entire disk (inwards and outwards) and the increased accretion rate is maintained until the temperature of the outer disk drops below the ionization temperature. This then causes a cooling wave to form and propagate, switching the disk back to a quiescent state after a (surprisingly small) fraction of the total mass of the disk has been accreted.

The DIM as applied to black hole and neutron star binaries gives very different behaviour to that of white dwarfs. While the quiesent disk and fast rise can be modelled by the same codes, they cannot produce the quasi-exponential decay that we observe. This is likely because the luminous inner regions of the disk in more compact systems are larger, and thus irradiation is important, so the outer disk cannot cool as quickly (van Paradijs 1996). If that irradiation of the outer disk is strong enough, hydrogen can be prevented from recombination. This process eats away the disk, decreasing the temperature and lowering the accretion rate until irradiation dies down to the point where thermal emission dominates (thermal state) again. Eventually the outer disk temperature drops below the ionization temperature, and the disk switches back to the cool branch (as the outer disks in quiescent and hard state LMXBs), but is prevented from reaching all the way to the ISCO because of the irradiation in the inner regions (King & Ritter 1998).

This can explain some differences between black hole and neutron star primaries in LMXBs. A neutron star will have a smaller mass, so for a given companion mass to overflow its Roche lobe, the orbital separation must be smaller. This means that the disk is smaller, due to the smaller tidal truncation radius, and so the outer disk is more likely to be kept in a

hot state and becomes stable. In that case it would not undergo this limit cycle. More neutron LMXB are known to be persistent sources, while all known BH LMXBs are transients (Dubus et al. 1999).

While this process is believed to occur in BH LMXBs, the difficulty of computations (due to the many different timescales and lengthscales in the whole disk, and the additional physics needed) are prohibitive for an all-inclusive description.

4.4 Describing the Coronal/ADAF Flow

Many authors have addressed the thermal and physical states of the accretion flow in these systems. Much of the work has concentrated on what is required of the thermal and physical states of the flows in order to explain the (X-ray) spectra. In these works, the system is usually assumed to be in a steady configuration, and efforts are directed towards computation of the spectrum. There has also been substantial work on the interactions of two-phase flows which are briefly summarized below.

Shapiro, Lightman & Eardley (1976) introduced the concept of a two-phase (cold disk + hot corona) accretion model. Their disk consisted of a hot, optically thin and geometrically thick corona, and an outer standard (Shakura-Sunyaev) disk. The major aim of their model was to explain the observations of Cyg X-1, but later authors showed it to be thermally unstable (Piran 1978), so the hot solution would always rapidly cool down. This model was the direct forerunner of the current ADAF model, the key difference is that the new model explicitly includes advection, and the Shapiro et al. model did not. It turns out that the inclusion of advection makes it a stable solution, but this was not explicitly included until Narayan & Yi (1994).

Wandel & Urry (1991) and Wandel & Liang (1991) constructed models of Seyfert galaxies given three different assumptions in the flow geometry. They discuss a 'sandwich' geometry where the disk and corona literally form a sandwich, either separated radially or vertically.

Models like this were then developed more by Haardt & Maraschi (1991, 1993). The Nayakshin & Svensson model discussed in Ch. 3 is of this type.

Witt, Czerny & Zycki (1997) presented a two-phase model where the two phases interact by Compton cooling of the hot corona by cool disk photons and the heating of the disk by illumination of the corona, respectively. They also included a parameterization of mass loss of the disk due to wind outflows.

Begelman & McKee (1990) began the work which this dissertation is based on, namely the effects of thermal conduction on two-phase media. They considered the thermal interaction of hot and cold phases under isobaric conditions and developed criteria to determine which phase shrinks or grows as a result.

Rozanska & Czerny (2000a) took this a step further and discussed radiative and conductive equilibrium for two-phase models. They find stability/instability to be dependent on the assumed coronal heating mechanism. In a later paper (2000b), they considered the mass loss/gain of both phases due to conduction for stationary disk models following the considerations of Begelman & McKee (1990).

The formulation of current advection-dominated accretion model was in the context of boundary layer accretion onto cataclysmic variables (Narayan & Popham 1993) and was then developed as a new stable mode of accretion (Narayan & Yi 1994; see Narayan 1998 for a review). Hot flows with similar properties were studied before (Ichimaru 1977; Shapiro, Lightman & Eardley 1976; Rees et al. 1982), but were largely abandoned as an active subject of research until the mid-1990s. Under the influence of the thermal instability described previously, the disk switches to an advection-dominated flow where only a fraction of the energy released is radiated away. The change from a geometrically thin disk to the hot flow is an essential feature in this picture, and exactly how this is accomplished is the primary focus of many researchers, including ourselves (see Ch. 5). The "strong ADAF principle," formulated by Narayan & Yi (1995b), suggests that, whenever the accreting gas has a choice between a standard thin disk and an ADAF flow, the ADAF configuration is chosen, due to

its lower entropy generation rate. Thus, the bulk of the liberated thermal energy is carried in by the accreting gas as entropy rather then being radiated. Another way of expressing it is that the cooling timescale of the material is longer than the accretion timescale. This type of accretion would give a natural explanation for low luminosities of black hole accretors in quiescence, where the hot gas could simply be swallowed up by the hole without ever radiating its energy away, whereas in the neutron star case the hot gas would hit the surface and the energy would have to be reprocessed.

The key equation in the ADAF flow model is a reexamination of the energy equation,

$$\Sigma v T \frac{ds}{dR} = Q^+ - Q^- \tag{4.6}$$

where $\Sigma = 2\rho H$ is the surface density of the gas, and H is the scale height of the disk. The left hand side of this equation is the advected entropy, with T as the temperature and s as the entropy per unit mass, while the right hand side is the difference between viscous heating, Q^+, and radiative loss, Q^- (per unit area). It should be pointed out that since all the energy is assumed to be in the protons, that the temperature above is assumed to be that of a single temperature fluid, and the electron temperature is estimated to be at least 2-3 orders of magnitude lower. Substituting a viscous dissipation rate for Q^+, we obtain,

$$Q^+ - Q^- = \frac{3}{2}\alpha P \Omega - Q^- = f\frac{3}{2}\alpha P \Omega \tag{4.7}$$

with f as the parameter measuring the degree to which the flow is advection-dominated. In the case of no radiative cooling f=1, and for efficient cooling f=0.

The sound speed in advection-dominated flows is comparable to the Keplerian speed, meaning their temperatures are nearly virial. This is expected because the gas is assumed to be unable to cool. A further consequence is that the scale height of the disk ($H \sim Rc_s/v_K$) is comparable to its radius, meaning the flow is quasi-spherical. Since $v_R \sim \alpha c_s^2/v_K$, the radial velocity in these flows is much larger than in thin disks, and the rotational speed would be significantly sub-Keplerian (Narayan & Yi, 1994; 1995a,b).

The heating in the corona is distributed, in reality, on to the electrons and protons. The fraction of heat going into the electrons directly is not very well understood though. Gruzinov (1999) shows that if the magnetic fields are near equipartition, higher radiative efficiencies are achieved and so most of the viscous heat goes into the electrons, while for low magnetic fields it goes into the protons, as assumed by the ADAF models. Quataert (1998) argued that there is damping at the protons Larmor radius and so most viscous heat goes into the protons. This was reconciled by both authors together (Quataert & Gruzinov 1999), who show that for equipartition magnetic fields most energy goes into the electrons.

4.5 Formation of the Coronal/ADAF Flow

Initial work on the formation of the hot corona was done in the context of cataclysmic variables (Meyer & Meyer-Hofmeister, 1994) and found that a "siphon flow" can lead to evaporation of the disk, powered by electron thermal conduction. Later works extended this process to neutron stars and black holes (Meyer-Hofmeister & Meyer, 1999; Meyer et al., 2000; Różańska & Czerny, 2000a,b) and found that a hot corona is always built up on top of the cool disk. In these models, the coronal temperature is kept up by friction, which heats the protons, since they have all the mass. Coulomb interactions transfer this energy to the electrons, which can then release it through radiation. The electron temperature gradient between the corona and disk causes conductive heat transport into the disk. The density of the corona adjusts itself by evaporating the disk underneath so that the net heat flow is balanced by advection, evaporation, and radiation. The equilibrium density in the corona gives us a mass accretion rate fed by the disk, and determines the disk's evaporation rate. Later calculations (Liu et al., 2002) showed that this vertical evaporation rate reached a maximum at a few hundred Schwarzschild radii. This mechanism naturally provides an explanation for the transition between the observed states: if the mass flow rate in the cold disk is below the the maximal evaporation rate, the disk truncates. If it is above this maximum, the disk continues all the way to the innermost stable orbit. A corona would

still exist on top of the disk and below it in a "sandwich" structure, capable of producing a weaker but steep power-law component seen in systems in the thermal state (it has been proposed that the mechanism behind the spectra seen remains the same in all states; Malzac & Belmont 2008). The theoretical picture that arises from these processes is as follows from Meyer et al. (2000). Heat released by viscosity in the corona flows downwards into cooler and denser layers. If the density is high, it gets radiated away (radiation in the optically-thin regime goes as $\sim \rho^2$). If it is not dense, the cooler matter gets heated up and evaporates into the corona until an equilibrium density is created. Mass drained from the corona by the inward movement is steadily replaced by material evaporating off the disk. This mass evaporation rate increases steeply with decreasing distance in the outer disk, but reaches a maximum at some radius (e.g., 100 R_g), caused by the change in the physical process that removes the heat released by friction. For large radii, the frictional heating in the corona is balanced by inward advection and wind loss. Downward heat conduction and subsequent radiation in the lower region play a minor role for the energy loss at large radii. Here, wind loss and conservation of angular momentum force some extension of the corona outwards, where the material can condense back onto the disk. The evaporation at large radii leads to an inner + outer disk configuration, and only recent works have touched on the existence of this remnant inner disk.

As an example, let us consider a system declining from the thermal state through lower intermediate state on the path to quiescence. The above explanation tells us that the disk will truncate first at the radius where the maximal evaporation rate equals the total accretion rate in the system, leaving a gap filled by an ADAF. The remaining inner disk should disappear within a viscous time ($\sim$ a few days), however observational results show that this lower intermediate state can last up to two weeks, telling us that somehow the inner disk is being replenished. Kalemci et al. (2004) studied several sources and analyzed the spectral and temporal properties during outburst decay. Spectral analyses show a decrease of the thermal component until it becomes unobservable with RXTE within 15 days of

the transition. Similar results were found by Zycki et al. (1998); Smith et al. (2001) and Pottschmidt et al. (2006).

When the evaporation rate exceeds the mass flow rate in the disk, a hole forms up to the distance where both rates are equal, and inside only a hot coronal/ADAF flow exists.

$$\dot{M}_{\rm evap}(R) \gg \dot{M}(R) \tag{4.8}$$

If the mass flow rate increases to the maximum evaporation rate, as in the rise to outburst, the truncation radius moves in closer to the black hole.

$$\dot{M}_{\rm evap} \geq \dot{M} \tag{4.9}$$

Finally, when the flow rate crosses over this maximum, the disk should extend all the way to the ISCO, and the spectrum produced will be thermal.

$$\dot{M}_{\rm evap} < \dot{M} \tag{4.10}$$

In decline, the opposite happens, and the disk inner radius moves away from the ISCO (Esin et al. 1997).

Liu et al. (2006) first addressed the lower intermediate state in response to these observations. In their one-zone radially-uncoupled approximation they show that for specific values of gas pressure and densities, the net result could be that the gas in the ADAF would recondense back onto a cool inner disk underneath, allowing the inner disk to persist until the accretion rate dropped sufficiently. They solve a simple expression for the optically-thin radiative layer above the disk, whose energy comes from conductive flux from the coronal flow, that we also solve in Ch.5 (and see Appendix). The mathematical formulation of this paper only allowed for condensation and evaporation without the effects of vertical advection on the conductive flux between the disk and corona, but this was subsequently corrected and expanded in Meyer et al. (2007). A third paper adding the effect of local Comptonization above the inner accretion disk soon followed (Liu et al., 2007) and applied the model to

observations suggesting the existence of an inner accretion disk in the hard state (Miller, 2006; Tomsick et al., 2008) and which made predictions of the luminosity of such systems at state transition. Another recent publication by their group took things slightly further, melding Comptonization with conduction above the inner disk alone (Taam et al., 2008). A closely related two-phase (low resolution) time-dependent model of the same effects over an entire accretion disk was carried out by Mayer & Pringle (2007).

The work by this group attempts to show that for certain accretion rates on the decline from outburst, the disk will truncate at the radius where the evaporation rate becomes a maximum, and a gap forms, filled by an ADAF. Diffusion causes the inner disk to spread inwards and outwards, decreasing the amount of disk matter due to accretion on the compact object (inwards) and evaporation (outwards). Only if the matter in the ADAF flow can condense, can the inner disk survive longer than a viscous time (a few days) and explain the observations of $\sim$ 15 day transitions. If this inner disk survives, it would show up as an additional soft and/or reflective component in the spectrum. From their analysis, the recondensation becomes complete for mass accretion rates as high as the evaporation rate at a few hundred Schwarzchild radii.

The five equations used in the one-zone approximation are: (1) the continuity equation, (2) z-component of angular momentum, (3) and (4) are the two energy equations for ions and electrons, and a prescription for thermal conduction (5). The dependent variables are pressure, ion and electron temperature, vertical mass flow rate, and heat flux. Boundary conditions are taken (a) the bottom of the corona, temperatures given, no heat inflow, and (b) at some height, a sonic point, and no influx of heat.

If we want to extract detailed results, we have to remember that a number of simplifications are used in the one-zone description that will lead to uncertainties in computational results. Two free parameters (α and the chemical abundance) enter into the evaluation of the mass evaporation rate. Note that α parameterizes both the frictional heat release and the radial flow of mass and angular momentum. The value we use in our study, 0.2, is

that suggested by observations and is not directly comparable to the α used by Shakura & Sunyaev (1973). For a comparison in the context of MHD, see a discussion by Hawley & Krolik (2001).

Heat conduction is an essential element; otherwise coronal gas would not lose energy and would continue upwards in temperature to virial, as it is in advection-dominated flows. Meyer-Hofmeister & Meyer (2006) investigated how conduction affected the interaction between disk and corona. Since it is connected with the evaporation efficiency, this means a possible change in the truncation radius of the disk. Motivation came from the fact that numerical simulations by Meyer-Hofmeister et al. (2005) and Liu et al. (2005) suggested that irradiation of the outer disk lead to larger truncation radii than are indicated by observations (Yuan & Narayan 2004). The question they asked in their work was whether reduced conduction could bring the truncation radii back in to fit the observations.

They found that, when including hard irradiation from the central source, reducing heat conduction changes the vertical structure of the corona. For a reduced value of conduction the electron temperature is lower and the ion temperature is higher than for effective heat conduction, and the radius where evaporation is most efficient moves inward by a factor of 7 for a reduction to 20% conduction.

4.6 Conclusion

The current paradigms for the different states have been presented as well as work being done currently by the Meyer, Meyer-Hofmeister, and Liu group on state transitions along the lower branch of the hysteresis curve. The next chapter will spell out our research on expanding the model, still in a one-zone approximation.

5. Theoretical Modeling of State Transitions

5.1 Introduction

In this chapter, we investigate a evaporation/condensation model of disk/coronal accretion into a black hole. We show that the inner regions of an accretion disk in X-ray binaries can transform from a cool standard Shakura-Sunyaev disk to an advection-dominated flow through the known properties of Coulomb interaction in a two-temperature plasma, viscous heating, radiative processes, and thermal conduction. We illustrate how a hot, diffuse corona covering the disk is powered by accretion, and that it exchanges mass with the underlying cold disk. If the accretion rate in the system is low enough, we show that the corona evaporates the disk away, leaving an advective flow to continue towards the hole. In the soft/hard transition commonly seen in X-ray binaries, we show that this advective flow can recondense back onto the underlying disk if the change in the system's accretion rate is slow enough, so we can use a steady-state approximation, due to thermal conduction.

Ultimately, unabsorbed spectra are produced to test against observations as well as empirical predictions of the location of truncation radii of the accretion disk. This includes bremsstrahlung from the corona, as well as blackbody emission from the underlying accretion disk.

In the previous chapter most of the relevant background information as well as the prior work by the Meyer group on the formation of an ADAF/coronal flow was highlighted. The prior work was done for constant accretion rates, whereas here we allow the accretion rate in the ADAF to vary self-consistently using the same basic formulae as the prior works of the Meyer group (Meyer et al. 2007, hereafter MLMH) and then building on these formulae to create a model distinct from those published before.

The work presented here uses virtually the same machinery as MLMH but expands it

to cover larger radii, up to $\sim 1000R_g$. We remove some minor inconsistencies and improve the treatment in the following way: in the prior work, the accretion rate in the ADAF was assumed to be a given and held constant; we allow the accretion rate to grow, starting from an assumed seed value that may evaporate the disk leading to truncation. For a limited range of accretion rates, the coronal flow may recondense back onto the remnant inner disk. We find that we can achieve behavior analogous to the hysteresis observed in the X-ray spectra in BHXBs and the theoretical behavior proposed in Esin et al. (1997) if we adopt a few simplifying assumptions, and assume that the inner disk ($\leq 1000R_g$) evolves through a sequence of steady states as we vary the total supply rate coming from the outer disk. We further find that if we adopt a value for the critical supply rate at which the system transitions from the hard to the soft state, or equivalently fixing a seed coronal or ADAF transfer rate at some outer boundary, then we can make a semi-empirical prediction of the location of the truncation radius and condensation radius in the accretion disk for any supply rate. We then use these results to compute example spectra for various modes of accretion, assuming the corona and the ADAF radiate only as bremsstrahlung and the disk underneath as a blackbody.

5.2 Model Structure

The model constructed below builds on the model of MLMH and uses the same vertical structure. At the outer boundary of our flow, there is assumed to be a two-temperature corona with a specified seed accretion rate, sitting above the cold thin disk of a larger accretion rate. At the base of the corona is a thin transition layer where the temperatures of the ions and electrons merge, below which is another radiating layer that radiates the downwards conducted energy from the corona. The energy balance in this layer then determines whether evaporation or condensation occurs from or onto the disk underneath.

We assume that our structure is in steady state. Later, as we consider how this structure changes as the mass supply arriving to the outer boundary of our disk-corona sandwich

varies, we assume that the structure follows a sequence of steady states. The mass supply is presumed to vary, for example, as a result of the standard disk instability in an outer disk beyond $\sim 10^3 R_g$ which is not modeled here (see Ch.4, Section 3).

5.2.1 Conservation of Mass in the Disk and Corona

As in MLMH, all accretion rates are normalized to the critical Eddington rate $\dot{M}_{\rm Edd}$ (see Ch. 4) and radial distances are in units of the Schwarzchild radius, R_g. The equations we use have various dependences on $\dot{m}_{\rm ADAF}$ and r, and the addition of the cumulative effects of a variable vertical evaporation/condensation rate means that the accretion rates in the ADAF and the underlying disk are varying with radius. If we assume a total accretion rate for the system, or "supply" rate $\dot{m}_{\rm s}$, and a seed value for the accretion rate in the ADAF at the outer boundary of the model, $\dot{m}_0$, (with $R_{\rm out} \sim 1000 R_g$), we can estimate the truncation and recondensation radii for any state of the system. We assume first that the system is in steady state and that the total mass supply rate at any radius is a constant and is equal to the amount in the disk plus that in the corona

$$\dot{m}_{\rm s} = \dot{m}_{\rm d} + \dot{m}_{\rm ADAF} \tag{5.1}$$

while the net change in either $\dot{m}_{\rm d}$ or $\dot{m}_{\rm ADAF}$ is equal to the vertical evaporation/condensation rate $\dot{m}_z$ (per unit area for one side of the disk as in MLMH), which can have either sign. Taking $\dot{m}_z$ as positive for evaporation,

$$\frac{d\dot{m}_{\rm d}}{dr} = 4\pi r \dot{m}_z \tag{5.2}$$

$$\frac{d\dot{m}_{\rm ADAF}}{dr} = -4\pi r \dot{m}_z \tag{5.3}$$

giving us conservation of mass

$$\frac{d}{dr}(\dot{m}_{\rm d} + \dot{m}_{\rm ADAF}) = 0 \tag{5.4}$$

We have neglected the possibility of wind/outflow throughout our calculations. Physically, given the large ratio of H/R for the corona, the corona is only marginally bound within the

gravitational potential (see Blandford & Begelman 1999). It may well be that mass, energy and angular momentum are carried away in an outflow, jet or wind. This would likely lead to a reduction of H/R until a stable state is found, and be an additional cooling mechanism for the corona. Observations of low-luminosity AGN and X-ray binaries in their hard state indicate they could harbor large-scale outflows (Fender et al. 2004), which could be driven magnetically and/or by radiation pressure.

We assume that there is no (vertical) torque arising from the exchange of mass between the disk and the corona. This is a reasonable assumption as long as the specific angular momentum of the material in the disk and the corona at a given radius is the same.

5.2.2 Advective Flow Above the Thin Disk

We assume that the corona above the disk follows the self-similar formulation for ADAFs derived in Narayan & Yi (1995a), which assumed $\dot{m}_{\rm ADAF}$ to be constant. We allow $\dot{m}_{\rm ADAF}$ to vary as evaporation and condensation augment it or diminish it respectively. The self-similar solution we use should remain valid if the coronal flow has roughly the same radial velocity throughout and its temperature is given by the virial form (Eq. 5.16). Our treatment is very similar to that of MLMH and for convenience we will duplicate the results in the following sections. However, in contrast to their work, which derived the equations using $f \sim 1$, we make no assumptions on the value of the advection parameter, f (defined in the range from 0 to 1, Eq. 4.7) or the other constants below *a priori*, and all differences between our results are highlighted. In general, f depends on the details of the heating and cooling which will vary with R. The assumption of a constant f, which we make later on, is therefore still an oversimplification. However, when the flow is advection-dominated, $f \sim 1$ througout the flow, and f can be well approximated by a constant.

$$c_1 = \frac{(5+2\epsilon')}{3\alpha^2} g(\alpha, \epsilon') \tag{5.5}$$

$$c_2 = \left[\frac{2\epsilon(5+2\epsilon')}{9\alpha^2} g(\alpha,\epsilon')\right]^{1/2} \tag{5.6}$$

$$c_{\rm s}^2(R) = \frac{2(5+2\epsilon')}{9\alpha^2} g(\alpha,\epsilon') v_{ff}^2 \equiv c_3 v_{ff}^2, \tag{5.7}$$

where

$$v_{ff} \equiv \left(\frac{GM}{R}\right)^{1/2}, \tag{5.8}$$

$$\epsilon' \equiv \frac{\epsilon}{f} = \frac{1}{f}\left(\frac{5/3-\gamma}{\gamma-1}\right), \tag{5.9}$$

$$g(\alpha,\epsilon') \equiv \left[1 + \frac{18\alpha^2}{(5+2\epsilon')^2}\right]^{1/2} - 1 \tag{5.10}$$

where α represents the standard viscosity parameter (Shakura & Sunyaev, 1973). The magnetic pressure in our solution is given by

$$p_{\rm m} = (1-\beta)\rho {c_{\rm s}}^2 \tag{5.11}$$

with β as the ratio of gas pressure to total pressure, ρ density and $c_{\rm s}$ isothermal sound speed. As the ratio of specific heats of the magnetized plasma we take $\gamma = (8-3\beta)/(6-3\beta)$ (Esin, 1997). γ is likely to remain in the range of 4/3 to 5/3, with the two limits corresponding to a radiation pressure-dominant and gas pressure-dominant flow, respectively (a derivation of γ is provided in Appendix B).

A few interesting features are immediately revealed by this self-similar solution. Observational data suggests that ADAFs have relatively large values of the viscosity parameter, which means that the radial velocity of the gas is comparable to the free-fall velocity. The gas thus accretes quite rapidly. Also, the gas rotates with a sub-Keplerian angular velocity and is only partially supported by centrifugal forces. The rest of the support comes from the radial pressure gradient, and in the extreme case of $\gamma = 5/3$, has no rotation at all.

For the chemical abundance a hydrogen mass fraction of X=0.75 was used. The solutions for pressure, electron number density, viscous dissipation of energy per unit volume q^+ and isothermal sound speed are (from Narayan & Yi 1995a)

$$p = 1.71 \times 10^{16} \alpha^{-1} c_1^{-1} c_3^{1/2} m^{-1} \dot{m}_{\rm ADAF} r^{-5/2} {\rm gcm}^{-1}{\rm s}^{-2}, \tag{5.12}$$

$$n_e = 2.00 \times 10^{19} \alpha^{-1} c_1^{-1} c_3^{-1/2} m^{-1} \dot{m}_{\rm ADAF} r^{-3/2} {\rm cm}^{-3}, \tag{5.13}$$

$$q^+ = 1.84 \times 10^{21} \epsilon' c_3^{1/2} m^{-2} \dot{m}_{\rm ADAF} r^{-4} {\rm ergcm}^{-3}{\rm s}^{-1} \tag{5.14}$$

$$c_s^2 = 4.50 \times 10^{20} c_3 r^{-1} \ {\rm cm}^2{\rm s}^{-2} \tag{5.15}$$

where m the black hole mass in units of solar mass $M_\odot$, $\dot{m}_{\rm ADAF}$ the mass flow rate in the ADAF in units of the Eddington accretion rate $\dot{M}_{\rm Edd} = 1.39 \times 10^{18} m \, {\rm g/s}$, and r the radius in units of the Schwarzschild radius $R_g = 2.95 \times 10^5 m \, {\rm cm}$.

With the assumed chemical composition for the accreting plasma, the ion number density is $n_i = n_e/1.077$ (Appendix A.1). In a two-temperature ADAF, ion and electron temperatures T_i and T_e closely follow

$$T_i + 1.077 T_e = 6.66 \times 10^{12} c_3 \beta r^{-1} {\rm K} \tag{5.16}$$

and, if T_e is much smaller than T_i this value can be taken for T_i alone. This comes from the assumption that the plasma in ADAFs is coupled only by Coulomb collisions, and with the ions having the larger mass, they will become hotter due to viscous friction. This important assumption could be challenged on the grounds that magnetized collisionless plasmas have many modes of interaction and it would seem that the plasma might be able to find a more efficient means than Coulomb coupling to exchange energy between the two components (Phinney 1981). Only one mechanism has been identified by Begelman & Chiueh (1988), which was argued by Narayan & Yi (1995b) to not apply to ADAF models because of their weakly magnetized flows.

In addition to q^+, compressive heating $q^c = \frac{1}{(1-\beta)} q^+$ (Esin, 1997) can be important and hence we include it in our formulation.

5.2.3 Coupling Layer

Due to the large mass difference between the ions and electrons, we assume that q^+ acts only on the ions, which transfer their energy by Coulomb interactions to the electrons, neglecting direct viscous heating of the electrons.The electron temperature is limited, in general, by bremsstrahlung, synchrotron (-self-Compton), (inverse) Compton emission and vertical conduction. We treat the underlying accretion disk as a cold sink, allowing mass exchange between disk and corona through a vertical flow but neglecting energy advection to and from the disk, and in subsequent spectral calculations, its effect on the blackbody spectrum.

For the Coulomb interaction we take (from Liu et al. 2002), with the assumption that T_i is much greater than T_e,

$$q_{ie} = 3.59 \times 10^{-32} \mathrm{gcm^5 s^{-3} deg^{-1}}\, n_e n_i T_i (\frac{kT_e}{m_e c^2})^{-\frac{3}{2}} \tag{5.17}$$

$$= 4.06 \times 10^{34} \mathrm{gcm^{-1} s^{-3} deg^{3/2}} c_1^{-2} \alpha^{-2} \beta m^{-2} \dot{m}^2_{\mathrm{ADAF}} \; T_e^{-3/2} r^{-4} \tag{5.18}$$

which is a decent approximation, although not valid everywhere in the vertical structure in general (see Dermer, Liang, & Canfield 1991; Stepney & Guilbert 1983).

The energy from viscous friction in the ADAF is transferred both radially and vertically. The fraction that is not advected to the next radial zone is assumed to completely transfer to the electrons in a coupling layer, at the bottom of which the temperatures of ions and electrons become equal. Within the vertical structure for one radial zone, the ions are able to transfer their energy to the coupling layer, and any loss due to advection inwards is considered to be replenished by the next outward radial zone.

To solve for this coupling temperature in the conduction-only case, we assume that the viscous heating of ions and compression is balanced by the Coulomb transfer, assuming that

the ion temperature remains nearly virial for most of the extent of the coupling layer.

$$q^+ + q^c = q_{ie} \tag{5.19}$$

which gives

$$\begin{aligned} T_{\rm cpl} &= 7.865 \times 10^8 c_1^{-4/3} c_3^{-1/3} \epsilon'^{-2/3} \times \\ &\left(\frac{2-\beta}{1-\beta}\right)^{-2/3} \alpha^{-4/3} \beta^{2/3} \dot{m}_{\rm ADAF}^{2/3} \end{aligned} \tag{5.20}$$

at some height $z_{\rm cpl}$ to be determined later. The above value is then appropriately scaled using a vertically averaged $n_e n_i$, assuming an exponential atmosphere of the form $n = n_0 \exp(\frac{-z^2}{H^2})$. The numerical expression we use for the vertical scaleheight $H = c_s/\Omega_K$ is defined in Eq. (5.24).

Above $z_{\rm cpl}$ the energy input to electrons is balanced by downward conduction and radiation. Most of the radiative losses occur at low heights since their rates are proportional to n_e^2 typically. As in MLMH we assume that thermal conduction is the primary means of energy transport in the vertical direction, neglecting the radiative losses in the coupling layer, giving us the temperature profile of the electrons as a function of z. The downward heat flux begins at large height $F_{\rm c} = 0$ and increases to some value at the bottom of the coupling layer where the ion and electron temperatures are equal. At this height we set the change in conductive flux to the total transfer rate to find the total flux from the ADAF above

$$F_{\rm c} = -\kappa_0 T_e^{5/2} dT_e/dz, \tag{5.21}$$

$$\frac{dF_{\rm c}}{dz} = -q_{ie}(T_e). \tag{5.22}$$

by integration over the temperature interval (Spitzer, 1962). The result is

$$F_{\rm c}^2 = \kappa_0 (K n_i n_e T_i)(T_{\rm m}^2 - {T_e}^2) \tag{5.23}$$

with the constant $K = 1.64 \times 10^{-17} {\rm gcm^5 s^{-3} deg^{1/2}}$. Further integration of z gives us a relationship between the maximum electron temperature $T_{\rm m}$ and the height at which it is

reached z_m. Assuming that this height is the vertical scaleheight for $n_e n_i$, which is $\frac{1}{\sqrt{2}}$ of the density scaleheight, $H = c_s/\Omega_K$, we get

$$z_{\rm m} = 3.5 \times 10^5 c_3 \, m \, r \text{ cm}. \tag{5.24}$$

and the integral is

$$z_{\rm m} - z = \sqrt{\frac{\kappa_0}{K n_i n_e T_i}} {T_{\rm m}}^{3/2} \int_{T_e/T_{\rm m}}^{1} \frac{x^{5/2}}{\sqrt{1-x^2}} \, dx. \tag{5.25}$$

where $x = \frac{T_e}{T_{\rm m}}$. The work of MLMH makes the assumption that $T_{\rm cpl} \ll T_{\rm m}$, allowing them to extend the integral from zero to one. We relax this assumption, as this formulation forces the temperature curves to cross at a few hundred Schwarzschild radii. Instead, we continue to assume that $z_{\rm cpl}$ is small compared to $z_{\rm m}$, and use an approximation for the integral when the temperatures are close to one another of the form

$$\int_{T_e/T_{\rm m}}^{1} \frac{x^{5/2}}{\sqrt{1-x^2}} \, dx = 0.71889 \sqrt{(1 - \frac{T_e}{T_{\rm m}})} \tag{5.26}$$

which is valid in both limits. This assumption allows us to solve numerically for $T_{\rm m}$ and $F_{\rm c}$ as functions of radius and $\dot{m}_{\rm ADAF}$.

There is no independent prescription for $z_{\rm cpl}$ other than the above coupling through electron conduction to $z_{\rm m}$, which itself is only known to an order of magnitude. We have relaxed the assumption that $z_{\rm cpl}$ is small by giving it arbitrary values ranging from 0.5-0.9$z_{\rm m}$ and performing our integrations anew. We find that the results are qualitatively the same and quantitatively not very sensitive to the assumed value of $z_{\rm cpl}$.

5.2.4 Coupling Interface with Radiating Layer

In the case of no mass exchange between the corona and the disk, Eq.5.23 gives the conductive flux entering the radiating layer from the ADAF above, originally considered by Liu et al. (2006). When vertical advection is included, and radiative losses in the coupling layer are neglected, the total energy flux from the corona at the top must equal the total energy flux

through the bottom into the radiating layer

$$F_{\rm cpl} + \dot{m}_z \frac{\gamma}{\gamma - 1} \frac{1}{\beta} \left(\frac{\Re T_{\rm cpl}}{\mu} \right) = F_{\rm c}^{\rm ADAF} + \dot{m}_z \frac{\gamma}{\gamma - 1} \frac{1}{\beta} \left(\frac{\Re T_i}{\mu_i} \right) \tag{5.27}$$

Here $F_{\rm cpl}$ is the advected conductive heat flux leaving the interface on the lower side into the radiating layer, and $\Re$ is the ideal gas constant.

The terms containing the vertical mass flow rate per unit area, $\dot{m}_z$, represent the advected heat flow at the top and bottom of the coupling layer. Note that the conductive fluxes are in general negative (downward) and $\dot{m}_z$ is defined negative for condensation. MLMH introduce the ratio

$$\epsilon = \frac{\mu_i T_{\rm cpl}}{\mu T_i} \tag{5.28}$$

which is always small for the condensation-only case they consider, and is subsequently neglected. We do not make this simplification, as this ratio gets closer to 1 at the outer boundary of our integrations (Note that this quantity is different from the ϵ used in Eq. 5.29).

Defining a convenient normalization for the mass flow rate,

$$\dot{m}_z^* = \frac{\gamma - 1}{\gamma} \beta \frac{-F_{\rm c}^{\rm ADAF}}{\frac{\Re T_i}{\mu_i}(1 - \epsilon)} \tag{5.29}$$

we obtain for the heat flow $F_{\rm cpl}$ entering the radiating layer from above the following expression

$$F_{\rm cpl} = F_{\rm c}^{\rm ADAF} \left[1 - \frac{\dot{m}_z}{\dot{m}_z^*} \right] . \tag{5.30}$$

We note that $\dot{m}_z^* > 0$, and thus the net conductive flux into the radiating layer can be greater or smaller than $F_{\rm c}^{\rm ADAF}$ depending on whether there is condensation or evaporation. This also allows us interpret physically $\dot{m}_z^*$ as the critical evaporation rate which would result in zero conductive flux into the radiating layer.

5.2.5 Evaporation of the Cold Disk

While the formulation at the coupling interface is strictly only valid in the condensation case, we assume that the in the case of evaporation, the evaporated ions, initially at a

temperature $\sim T_{\rm cpl}$, are heated up to the local near virial temperature primarily by viscosity and compression and also by interactions with the hot ions already present in the existing two-temperature corona. This is supported by the results obtained by Spruit & Deufel (2002), who showed that the ions would tend to be heated to near virial temperature. They also have shown that viscous heating dominates over heating of warm ($\sim T_{\rm cpl}$) ions by hot ($\sim T_{\rm vir}$) ions while leaving the electrons at a temperature $\sim T_{\rm cpl}$, which they kept constant in their simulations. Within our approximations, if one considers an energy equation for the warm ions consisting only of viscous heating and Coulomb losses to the electrons, while allowing the electrons to conduct downward this heat dumped by ions into the radiative layer, then a structure just like what is described in previous sections is set up, except that the mass flow is in the opposite sense than in the condensation case. We find that heating dominates Coulomb losses always if the density of the warm layer is allowed to adjust downward as the ion temperature increases, while keeping the vertically integrated density $\Sigma \propto n_i H \propto n_i T_i^{1/2}$ constant. In Appendix A.2 we present the time evolution equations governing the electron and ion temperatures under the processes mentioned above. Our treatment is similar to that of Spruit & Deufel (2002), but we include electron conduction and allow the electron temperature to evolve as well. We find also that once the ions reach the ADAF temperature, and the electrons set up the gradient from $T_{\rm m}$ down to $\sim T_{\rm cpl}$, advection is required to make the fluid stable, otherwise viscosity keeps increasing the ion temperature without limit. Because the local (annulus) model we consider in this paper does not include explicitly the effects of advection, we limit artificially the growth of the ion temperature and do not allow it to exceed the local virial temperature. See the appendix for more detail and a few results of the integration of these evolution equations at several radial distances from the black hole. Under the above assumptions, having shown that even in evaporation the ion temperature rises to the local virial temperature while the electron temperature rises to $\sim T_{\rm m}$, we conclude that the equations developed in the previous sections are valid for both condensation and evaporation and that $\dot{m}_z$ in the above treatment can have either positive or negative sign.

In a given radial annulus, most of the energy is advected inward to smaller radii ($f \approx 1$) but is replaced by advection from the adjacent outer annulus. Therefore, when considering the vertical energy and mass flows and the exchanges between ions and electrons, all of the energy in the ADAF is available for conduction downwards, and the effects of a radial flow are not considered. Most of the energy released by viscosity remains locked in the flow itself and is carried into the black hole.

5.2.6 Radiating Layer

In this section we study the behavior of the radiating layer beneath the ADAF and above the thin disk. As in MLMH, we begin by writing down the energy equation, keeping only the terms from internal heat, pressure work, thermal conduction, and bremsstrahlung cooling.

$$\frac{d}{dz}\left[\dot{m}_z \frac{\gamma}{\gamma-1}\frac{\Re T}{\beta\mu} + F_c\right] = -n_e n_i \Lambda(T). \tag{5.31}$$

Assuming free-free radiation dominates for $T_e \geq 10^{7.5}$K, $n_e n_i \Lambda(T)$ becomes $\frac{0.25}{k^2}(\beta\, p)^2 b T^{-3/2}$ with $b = 10^{-26.56}\mathrm{g\,cm^5 s^{-3} deg^{-1/2}}$ (Sutherland & Dopita, 1993). Contributions from gravitational energy release, viscous heating, and side-wise advection are neglected for the small vertical extent of the layer.

We follow MLMH to solve the differential equation for the radiative layer, subject to the boundary conditions $F_{\rm c} = F_{\rm cpl}$ at the upper boundary, and $F_{\rm c} = 0$ at the lower boundary where we take $T = 0$. Defining

$$C = \kappa_0 b \left(\frac{0.25\beta^2 p_0^2}{k^2}\right)\left(\frac{T_{\rm cpl}}{F_c^{\rm ADAF}}\right)^2 \tag{5.32}$$

where $p_0 = \frac{2}{\pi}p$, one finally arrives at the following expression for the vertical evaporation/condensation rate per unit surface of the disk,

$$\frac{\dot{m}_z}{\dot{m}_z^*} = 1 - \frac{\epsilon}{2} - \sqrt{\frac{\epsilon^2}{4} + C(1-\epsilon)} \tag{5.33}$$

See MLMH and Appendix A.3 for details.

The quantity C compares the radiative losses with the heat inflow from the ADAF. For $C = 1$ there is no vertical mass flow, as discussed in Liu et al. (2006). For $C < 1$, the density is so low that the heat inflow is used to heat up the gas underneath, causing evaporation. If $C > 1$ radiation is so strong that the gas in the ADAF cools and condenses onto the disk. The value we obtain for C and the critical condensation radius r_c where $C = 1$ are the same as those published previously but with the explicit inclusion of β:

$$C = 1.48\beta^2\alpha^{-28/15}\dot{m}_{\rm ADAF}^{8/15}r^{-1/5} \tag{5.34}$$

and

$$r_c = 7.10\beta^{10}\alpha^{-28/3}\dot{m}_{\rm ADAF}^{8/3} \tag{5.35}$$

valid only if $T_{\rm cpl} \ll T_m$ and $\dot{m}_{\rm ADAF} = const$, as in the case considered in MLMH. In our work this is not the case, and integrations show the function C to be considerably smoother because $\dot{m}_z$ is much smaller in the outer disk, and as such the condensation radius does not move further out than $\sim 100R_g$ in our prescription, for a reasonable choice of parameters.

5.3 Outer Boundary Condition

Long-term study of many black hole systems shows that they follow a peculiar 'q'-track in the HID (see Figs 2.4 and 2.8). In the hard state, they appear to be dominated by a hard power-law component, commonly interpreted as the signature of the advective flow (however jets could be making a significant contribution). In this state, the disk is believed to truncate at some large radius. As the system evolves towards the thermal state in outburst, a soft component begins to show as the inner edge of the disk moves inwards (Esin et al., 1997; McClintock & Remillard, 2006).

Some observations show that the accretion rate in such systems is roughly 10 % of the Eddington value at this hard-to-thermal intermediate transition, while other systems suggest a lower total accretion rate (1-4%, Maccarone 2003). Since we are interested in testing against the observations, we assume three values of the total accretion rate at the transition

between the hard and thermal states, $\dot{m}_{\rm s} = \dot{m}_{\rm tr} = 0.1, 0.04, 0.01$. At these rates, the disk continues all the way to the ISCO with no truncation. The prescription we have adopted here does not let us predict a value for the seed ADAF at the outer boundary, nor the rate at which the state transition occurs. However, picking one of these allows a calculation of the other. In practice, fixing the total accretion rate at state transition $\dot{m}_{\rm s} = \dot{m}_{\rm tr}$ allows us to calculate the the required seed ADAF at any arbitrarily chosen outer boundary $r_{\rm out}$. Each curve of $\dot{m}_{\rm ADAF}$ is then a unique solution depending on the assumed value of $\dot{m}_{\rm tr}$. This procedure allows us to fix the outer boundary value for the seed ADAF at $r_{\rm out} = 1000$ to be $\dot{m}_0 = 0.00925, 0.00743, 0.00376$ for the three representative total transition accretion rates chosen above. For example, we fix the total supply rate to be $\dot{m}_{\rm s} = 0.1$. If this is to be the transition rate between the hard and thermal state, then above this rate, the outer disk would continue all the way to the ISCO. We then vary the seed accretion rate in the ADAF until we find a unique solution which marginally does not truncate at any radius, and this seed value is $\dot{m}_0 = 0.00925$ at $r_{\rm out} = 1000$. Fixing this seed value, we then change the total supply rate to show how the steady state structure of the disk and corona changes for different values of $\dot{m}_{\rm s}$. There is nothing in our model that restricts us from choosing the outer boundary to be at any particular radius, and we could just as easily choose $r_{\rm out} = 2000$, however nearly all published results begin their calculations at $r \sim 1000$ and we choose to match those for ease of comparison. Observational evidence also lends support to the maximum truncation radius in quiescent systems being at around this radius.

Throughout the literature there have been several attempts to find a critical accretion rate below which advection-dominated flows can occur (Rees et al., 1982; Narayan & Yi, 1995b; Abramowicz et al., 1995; Yuan, 2001). These formulations assume a one-temperature ADAF heated by viscous friction and cooled entirely by bremsstrahlung. While the estimates given by these formulae for the maximal and seed ADAF accretion rate are very similar to that obtained by our method, our flow is not one-temperature at the outer boundary, so using them would not be entirely self-consistent.

5.4 Results: Conduction Model

In this section we present the results of our numerical calculations obtained by solving the equations given above for a black hole mass $m = 10$. We set the viscosity parameter $\alpha = 0.2$, the ratio of gas to total pressure $\beta = 0.8$, and the advection factor $f = 0.99$, except where otherwise stated, in all results herein for comparison to other models.

For example, let us say we want the state transition to occur at a supply rate $\dot{m}_{\rm s} = \dot{m}_{\rm tr} = 0.1$. Fig. 5.1 shows a plot of $\dot{m}_{\rm ADAF}$ versus radius (in units of R_g), for a given fixed seed accretion rate $\dot{m}_0 = 0.00925$ at $r_{\rm out} = 1000$ and different supply rates $\dot{m}_{\rm s}$. Given $\dot{m}_0$ and $r_{\rm out}$, and assuming the underlying disk is present at all radii, our equations allow us to calculate $\dot{m}_{\rm ADAF}$ everywhere. This solution is the topmost curve in Fig. 5.1. This curve exhibits a maximum at $r_{\rm c}$, where $C = 1$ and $\dot{m}_z$ changes sign. Thus if a disk is present at all radii, evaporation feeds the corona at $r > r_{\rm c}$ and the corona condenses back on to the disk at $r < r_{\rm c}$. The seed coronal accretion rate is determined by choosing an arbitrary outer boundary $r_{\rm out}$, picking a value for the seed and iterating until we get a maximum $\dot{m}_{\rm ADAF}(r_{\rm c})$ equal to the desired accretion rate $\dot{m}_{\rm tr}$ at state transition of 0.1. With this seed rate determined, we then vary the total supply rate of the system (e.g. $\dot{m}_{\rm s} = 0.02$, 0.05, 0.075, 0.085, and 0.1) and integrate inward from $r_{\rm out}$. As we integrate inward, $\dot{m}_{\rm ADAF}$ at first increases and $\dot{m}_{\rm d}$ decreases. When $\dot{m}_{\rm d} = 0$ is reached, all of the disk has been evaporated into the corona and the disk truncates. The radius at which this occurs us the transition or truncation radius $r_{\rm tr}$ for the assumed supply rate $\dot{m}_{\rm s}$. For $r < r_{\rm tr}$ we have an ADAF. As one increases the supply rate, $r_{\rm tr}$ moves inward until $r_{\rm tr} = r_{\rm c}$, when $\dot{m}_{\rm s} = \dot{m}_{\rm tr}$, and now a disk solution extending all the way down to the ISCO becomes possible for any supply rate $\dot{m}_{\rm s} \geq \dot{m}_{\rm tr}$. Note that the accretion rate carried by the disk varies with radius and formally vanishes at $r_{\rm c}$ if $\dot{m}_{\rm s} = \dot{m}_{\rm tr}$. For some values $\dot{m}_{\rm s} \leq \dot{m}_{\rm tr}$, if the disk was present previously, the corona can condense and maintain an inner disk for $r < r_{\rm c}(\dot{m}_{\rm s})$, with $r_{\rm c}(\dot{m}_{\rm s}) \leq r_{\rm c}(\dot{m}_{\rm tr})$. For example, looking at Fig. 5.1, one sees that the condensation radius moves inwards from

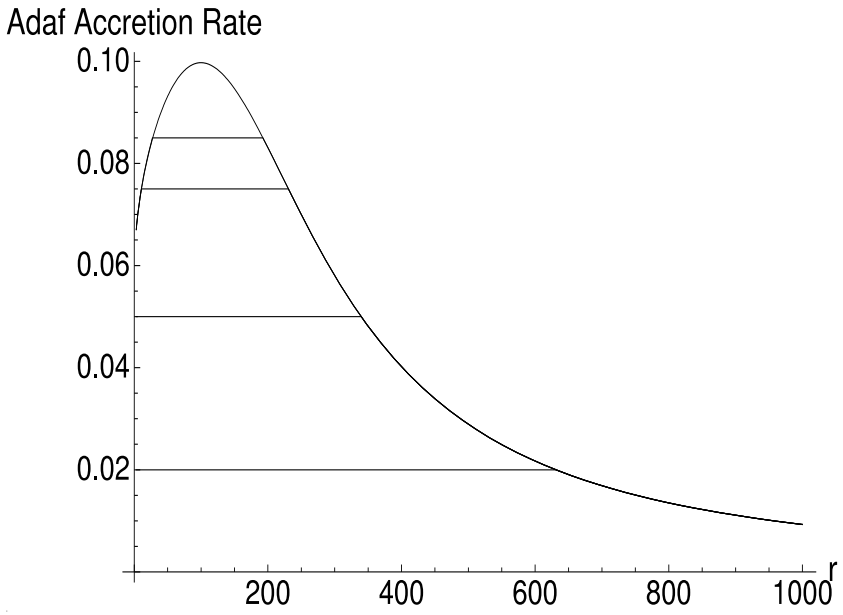

Figure 5.1: Plot of $\dot{m}_{\rm ADAF}$ vs radius in units of the Schwarzschild radius, given a seed coronal (ADAF) accretion rate $\dot{m}_{\rm ADAF}(r_{\rm out}) = 0.00925$, assuming an accretion rate at state transition $\dot{m}_{\rm tr} = 0.1$. The total supply rate of the system $\dot{m}_{\rm s}$ is varied through 0.1, 0.085, 0.075, 0.05, and 0.02, giving us the 5 curves shown. Notice that the truncation radius $r_{\rm tr}$ of the outer disk increases for lower accretion rates, while the radius where recondensation occurs moves inwards.

its largest possible value, $r \sim 100$ for $\dot{m}_{\rm s} = \dot{m}_{\rm tr} = 0.1$ to $r \sim 11$ for $\dot{m}_{\rm s} = 0.075$. Figs. 5.2 and 5.3 illustrate these same effects for $\dot{m}_{\rm tr} = 0.04$ and $\dot{m}_{\rm tr} = 0.01$ respectively for different total supply rates. The corresponding seed coronal rates at $r_{\rm out} = 1000$ also determined by iteration are $\dot{m}_0 = 0.00743$ and 0.00376 respectively.

Fig. 5.4 shows the dependence of the temperatures used in our model, the ion temperature T_i, the maximum electron temperature $T_{\rm m}$, and the coupling temperatures $T_{\rm cpl}$ on radius. For this we fixed the transition rate to be 0.1, and set the total supply rate $\dot{m}_s = 0.075$. The condensation radius is calculated to be $r \sim 11$ in this model, while the truncation radius is $r \sim 230$. From this figure we can see that $T_{\rm m}$ continues to large radii above $T_{\rm cpl}$, and its r-dependence forces it to increase inside the disk gap between r_c and $r_{\rm tr}$. However, its meaning is, strictly speaking, ambiguous in this region. $T_{\rm cpl}$ follows the plot of $\dot{m}_{\rm ADAF}$ in shape, increasing and decreasing as $\dot{m}_{\rm ADAF}$ does. In the disk gap, it has no meaning as there

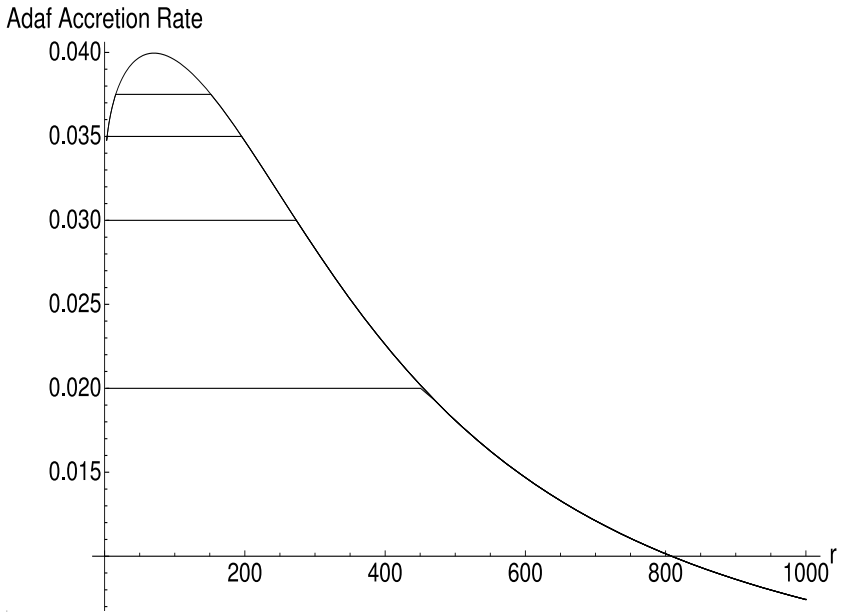

Figure 5.2: Plot of $\dot{m}_{\rm ADAF}$ vs radius in units of the Schwarzschild radius, given a seed accretion rate of 0.00743, assuming an accretion rate at state transition $\dot{m}_{\rm tr} = 0.04$. The total supply rate of the system $\dot{m}_{\rm s}$ is varied through 0.04, 0.0375, 0.035, 0.03, and 0.02, giving us the 5 curves shown. Notice that the truncation radius of the outer disk increases for lower accretion rates, while the radius where recondensation occurs moves inwards.

is no thin disk to exchange mass with, and a two-temperature flow is assumed to exist here as in the corona above the disk elsewhere so the temperatures cannot couple.

5.5 Spectra

5.5.1 Disk Emission

In order to facilitate comparisons to observations, we have constructed example spectra from the various disk structures this model creates. We assume that the outer and inner thin disk are best described by a standard thin disk, with a variable accretion rate that takes into account the cumulative effects of evaporation and condensation as defined in Eq. (5.1). We then use Eq. (5.36) below, and integrate over the two sets of radii to get the radially-integrated flux from each. We neglect the effects of irradiation of the disk by the adjoining radiating layer or any heat transport from above.

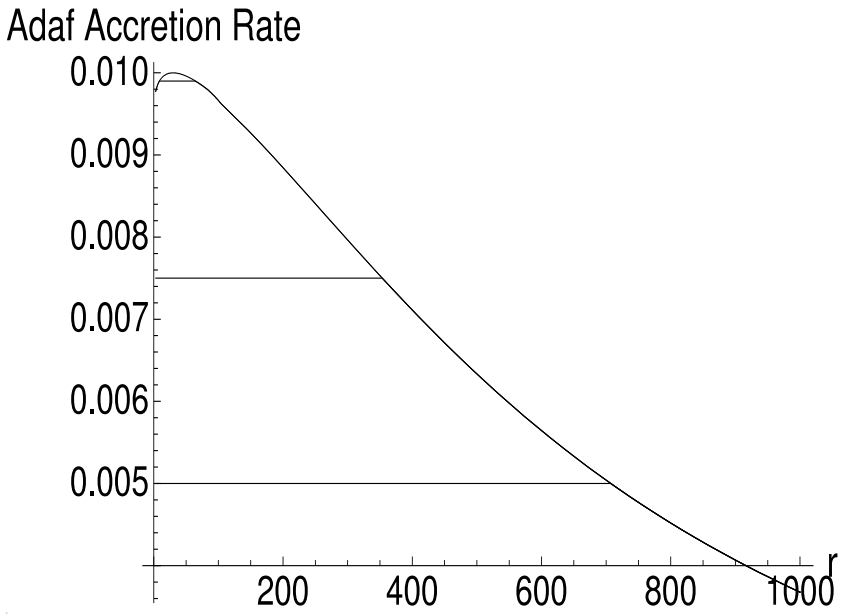

Figure 5.3: Plot of $\dot{m}_{\rm ADAF}$ vs radius in units of the Schwarzschild radius, given a seed $\dot{m}_{\rm ADAF} = 0.00376$, assuming an accretion rate at state transition $\dot{m}_{\rm tr} = .01$. The total supply rate of the system is varied through 0.01, 0.0098, 0.0075, and 0.005 giving us the 4 curves shown. Notice that the truncation radius of the outer disk increases for lower accretion rates, while the radius where recondensation occurs moves inwards.

With the above assumptions, the effective temperature taken is given by the standard result for thin disks,

$$\sigma T_{\rm eff}^4 = \frac{3GM\dot{m}_{\rm d}\dot{M}_{\rm Edd}}{8\pi(rR_g)^3}\left(1-\sqrt{\frac{3}{r}}\right) \tag{5.36}$$

which reaches a maximum $T_{\rm eff,max}$ at approximately $r = 49/12$. This is appropriately scaled and then inserted into the blackbody function, $B_\nu(T_{\rm eff})$, for calculation of the disk spectrum. Fig. 5.10 shows the spectral components due to the two separate disks as logarithmic plots of flux vs. frequency, given a supply rate of 0.075 for a transition rate of 0.1. We find, as one would expect, that the inner disk is the only observable contribution to the X-ray band seen by most detectors. Fig. 5.5 shows a comparison between the effective temperature for a truncated disk with supply rate of $m_s = 0.075$ and one where the truncation is marginal ($m_s = 0.1$).

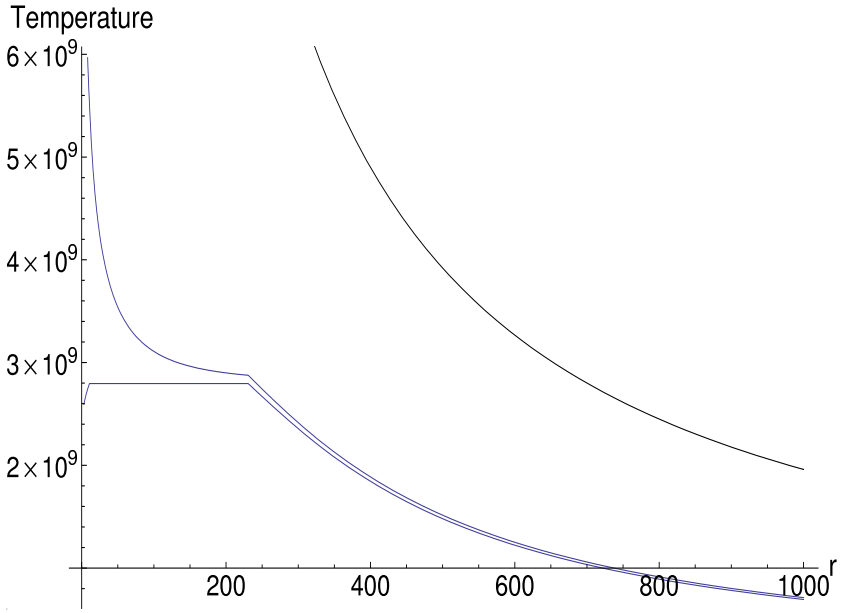

Figure 5.4: The dependence on radius of the three key temperatures used in the model. The total supply rate for the system is fixed at $\dot{m}_{\rm s} = 0.075$, with a seed coronal rate of $\dot{m}_{\rm ADAF} = 0.00925$, which yields an accretion rate at state transition $\dot{m}_{\rm tr} = 0.1$. For these choices, the condensation radius is $r \approx 11$. The uppermost curve is the ion temperature, assumed to follow the virial relation in Eq. (5.16). $T_{\rm m}$ and $T_{\rm cpl}$ are plotted below with $T_{\rm m} > T_{\rm cpl}$ throughout. Notice that $T_{\rm m}$ continues to increase within the transition radius of the outer disk-to-ADAF flow because of its r-dependence, while $T_{\rm cpl}$ closely follows the curve of $\dot{m}_{\rm ADAF}$.

5.5.2 Bremsstrahlung

Whenever an underlying disk is present, we assume the only radiation from the corona is thermal bremsstrahlung from the radiating layer, neglecting Comptonization of the disk photons. The frequency-integrated flux is given by

$$F_{\rm brem}(\dot{m}_{\rm ADAF}, r) = \int n_e n_i \Lambda(T) dz \tag{5.37}$$

This integral cannot be done explicitly since we do not know the vertical extent of the radiating layer, but we do know the total energy flux into the radiating layer from solving Eq. (A.15), with $\dot{m}_z$ given by Eq. (5.33). We can thus show that for all radii the flux is

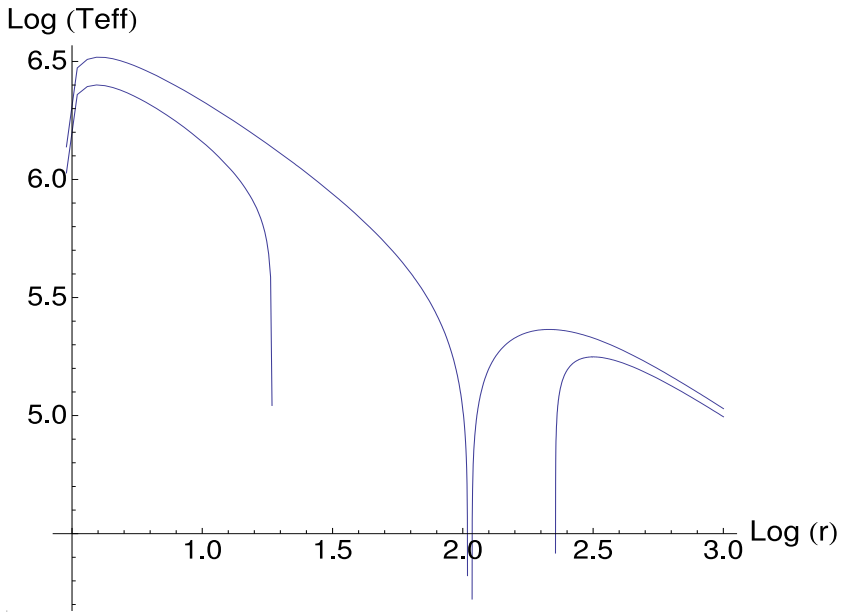

Figure 5.5: Logarithmic plot of $T_{\rm eff}$ vs. radius in Schwarzschild units, with a variable accretion rate in the underlying disk. Upper curve is for a supply rate of 0.1, while the lower truncated curve is for a supply rate of 0.075. This assumes the rate of state transition to be 0.1.

given by:

$$F_{\rm brem}(\dot{m}_{\rm ADAF}, r) = -F_c^{\rm ADAF}\left(1 - \frac{1 - \frac{\epsilon}{2} - \sqrt{\frac{\epsilon^2}{4} + C(1-\epsilon)}}{1-\epsilon}\right) \tag{5.38}$$

where all the variables on the RHS themselves depend on both $\dot{m}_{\rm ADAF}$ and r in general. This function differs from that of Liu et al. (2007) because we are taking the entire disk into account and ϵ cannot be always neglected. However our result does reduce into their formula in the limit of $\epsilon \ll 1$. We take the spectral volume emissivity to be

$$j_\nu = 6.8 \times 10^{-38} Z^2 n_e n_i T^{-1/2} \overline{g}_{\rm ff}(\nu, T) e^{-h\nu/kT} \tag{5.39}$$

where $\overline{g}_{\rm ff}$ is the velocity-averaged Gaunt factor. Within the X-ray band, the Gaunt factor can change form due to temperature increases. Thus the next step is to accurately determine the correct Gaunt factor to use everywhere. The Gaunt factor we use is

$$\overline{g}_{\rm ff}(\nu, T) = \frac{\sqrt{3}}{\pi} \ln \frac{kT}{h\nu} \tag{5.40}$$

so long as $\nu \ll kT/h$ (Tucker 1975; summarizing results from Karzas & Latter 1961). Beyond this limit, which does occur in the upper X-ray band, the factor changes with additional constraints. If $kT/h \sim \nu$ the factor must become 1, and if $\nu > kT/h$ it takes the value of

$$\overline{g}_{\rm ff}(\nu, T) = \left(\frac{kT}{h\nu}\right)^{0.4} \tag{5.41}$$

(Gorenstein et al., 1968). Since $T_{\rm cpl}$ is the temperature at the top of the radiating layer, we have used it in the calculations of the spectrum for bremsstrahlung over the disk.

To plot the bremsstrahlung and blackbody results together, we must determine the proper normalization to use. This can be deduced again from the constraint that locally the frequency-integrated bremsstrahlung flux must equal $F_{\rm brem}$. For the local specific bremsstrahlung flux we take $F_\nu^{\rm brem} = \pi j_\nu z_{\rm cpl}$, and express frequency in terms of the variable $x = h\nu/kT_{\rm cpl}(r, \dot{m}_{\rm ADAF})$, where k and h are Boltzmann's and Planck's constants, respectively. Thus,

$$F_\nu^{\rm brem} = \pi f(r, \dot{m}_{\rm ADAF}) \overline{g}_{\rm ff} {\rm e}^{-x}, \tag{5.42}$$

where $f(r, \dot{m}_{\rm ADAF}) = 6.8 \times 10^{-38} Z^2 n_e n_i T^{-1/2} z_{\rm cpl}$ is a function of r and the local rate carried by the corona. Finally, the frequency-integrated flux condition, is

$$F_{\rm brem} = \pi f(r, \dot{m}_{\rm ADAF}) \frac{kT_{\rm cpl}}{h} \int_0^\infty \overline{g}_{\rm ff} {\rm e}^{-x} {\rm d}x. \tag{5.43}$$

The above integral is evaluated once for all, and this finally allows us to solve for $f(r, \dot{m}_{\rm ADAF})$ bypassing our lack of explicit expression for $z_{\rm cpl}$

$$f(r, \dot{m}_{\rm ADAF}) = \frac{0.92954 h F_{\rm brem}}{\pi k T_{\rm cpl}} \tag{5.44}$$

With this normalization, we can obtain the local bremsstrahlung spectral flux in a form where all variables are known functions of $\dot{m}_{\rm ADAF}$ and r:

$$F_\nu^{\rm brem} = f(r, \dot{m}_{\rm ADAF}) \overline{g}_{\rm ff}(\nu, T_{\rm cpl}) e^{-h\nu/kT_{\rm cpl}} \tag{5.45}$$

We then integrate over the regions where a disk is present to find the radially-integrated flux from the radiating layers above the entire disk. For example, with a supply accretion

rate $\dot{m}_{\rm s}$ marginally above the transition rate $\dot{m}_{\rm tr} = 0.1$, the disk extends inward all the way. The spectrum in this case and any rate above that, will only have two components: the blackbody emission from the whole disk plus the bremsstrahlung emission from the radiating layer covering also the whole disk. This is depicted in Fig. 5.6 together with an example spectrum for $\dot{m}_{\rm s} = 0.2$ corresponding to the thermal state (see Ch. 4, Section 2.1). For a truncated disk, the shape of the bremsstrahlung spectrum is the same, but it is the outer disk that emits the dominant portion of the spectrum, this is depicted in Fig. 5.9.

Within the disk gap, however, we have chosen to use instead a separate description. In this region there is no disk below, and strictly speaking, the coupling temperature has no meaning. Only $T_{\rm m}$ continues to vary with radius in this region, because the density continues to increase in the ADAF, thus we have chosen to use it because it seems the most physically plausible situation. In the gap, we can see both sides of the disk and hence the scaleheight, z_m, carries a factor of 2:

$$F_\nu^{\rm ADAF} = R_g^2 \int 4\pi r z_m j_\nu(T_{\rm m}, \dot{m}_s, r)(1-f)dr \tag{5.46}$$

is the radially-integrated flux from the ADAF in the gap. A factor of $(1-f)$ is introduced because this is the amount that is radiated away by the ADAF in the gap between the inner and outer disk. Also, since the total supply rate has been evaporated into the ADAF, the correct accretion rate to use in calculations of the emissivity is this rate. For a supply rate of 0.075, the flux generated by the ADAF in the gap (where $r = 11 - 230$) is smaller than the bremsstrahlung emission above the outer disk, but larger in magnitude than the inner disk emission in bremsstrahlung. The total spectrum with each individual component plotted separately is depicted in Fig. 5.10. As the supply rate drops further, and the radial extent of the ADAF increases, the ADAF emission increases over the outer bremsstrahlung emission.

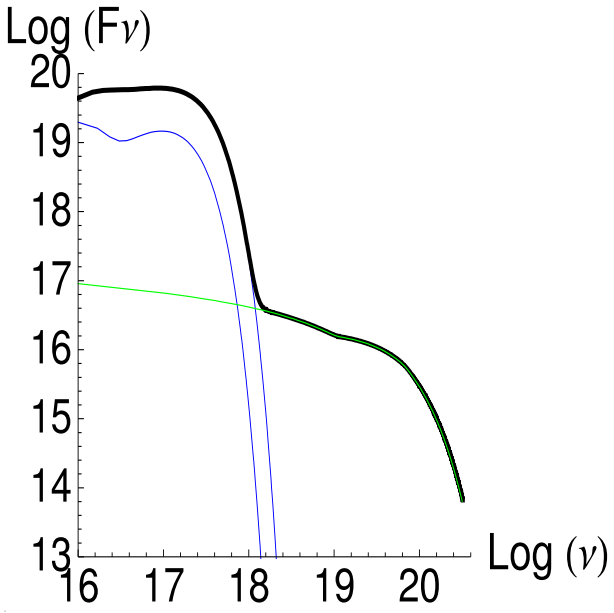

Figure 5.6: Bremsstrahlung (green) and blackbody (middle, blue) spectrum over a marginally whole disk of accretion rate $\dot{m}_{\rm s} = 0.1$, in the X-ray range. The dip in the blackbody spectrum is caused by the dip in temperature around $r_{\rm tr}$ visible on Fig. 5.5. This corresponds to the state labeled 4 on the hardness-intensity diagram (HID) shown on Fig. 5.11. The upper (blue) line shows the blackbody spectrum for $\dot{m}_{\rm s} = 0.2$ which looks more like the spectrum of a standard accretion disk since $\dot{m}_{\rm d}$ does not vanish anywhere. The corresponding bremsstrahlung component remains the same as for $\dot{m}_{\rm s} = 0.1$. The topmost solid curve is the total spectrum for the high or soft state calculated for a supply rate of $\dot{m}_{\rm s} = 0.2$. This corresponds to the state labeled 5 on the HID shown on Fig. 5.11.

5.6 Hysteresis

This model naturally produces a series of different structures as $\dot{m}_{\rm s}$ changes as stated in Section 5 and depicted in Figs. (5.1-5.3). In Fig. 5.11 we have set the supply rate of state transition to be $\dot{m}_{\rm tr} = 0.1$, allowing us to fix the seed value for the ADAF accretion rate, and then calculate the total luminosity from 1-60 keV, as well as luminosities in the 15-20 and 1-5 keV bands from our 3 spectral components (bremsstrahlung of ADAF, corona, and disk thermal). We define the hardness ratio with the luminosities in the (15-20 keV)/(1-5 keV) bands. These bands were chosen because many observed hysteresis curves use similar, and the two bands pick out separate components in the spectrum, i.e., the 15-20 band tracks

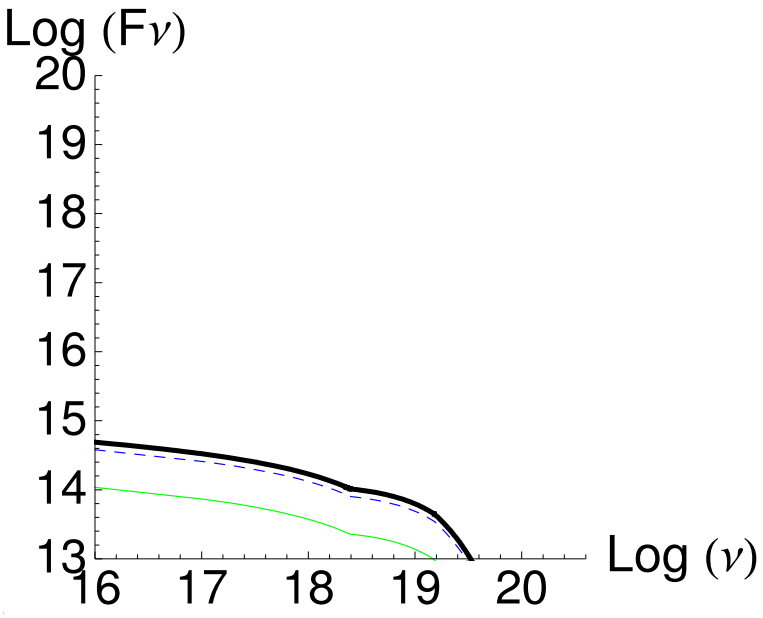

Figure 5.7: Bremsstrahlung spectrum in the X-ray range for the low/hard state, integrated over a truncated disk (green) along with emission from the ADAF itself (blue dashed). The thick solid line is the sum. The total supply rate for this case is $m_s = 0.01$. This corresponds to the state labeled 1 on the HID shown on Fig. 5.11.

solely the hard component, while the 1-5 band will show the importance of disk emission. Note that these figures should not be directly compared to observed count rates and we have not included the effects of interstellar absorption, geometric corrections for distance to the object and inclination, or taken into account the individual properties of the detectors.

To illustrate the possible hysteresis, let us follow one particular track on the hardness-intensity diagram, starting from the quiescent state represented by the lowest point in Fig. 5.11 (Compare Fig. 2.4). Here, the truncation of the outer disk occurs at $r_{\rm tr} \sim 956$ for $\dot{m}_{\rm s} = 0.01$. The emission we calculate is a combination of the bremsstrahlung above the outer disk, the ADAF, and the blackbody emission from the outer disk. If the supply rate is increased, $r_{\rm tr}$ moves inwards, and the spectrum at first becomes slightly softer because the bremsstrahlung spectrum gets slightly steeper until $\dot{m}_{\rm s} = 0.02$. For further increases of $\dot{m}_{\rm s}$, the spectrum gets harder until we reach $\dot{m}_{\rm s} = 0.095$. This is because the bremsstrahlung components elevate the 15-20 keV emission, particularly the bremsstrahlung emission of the

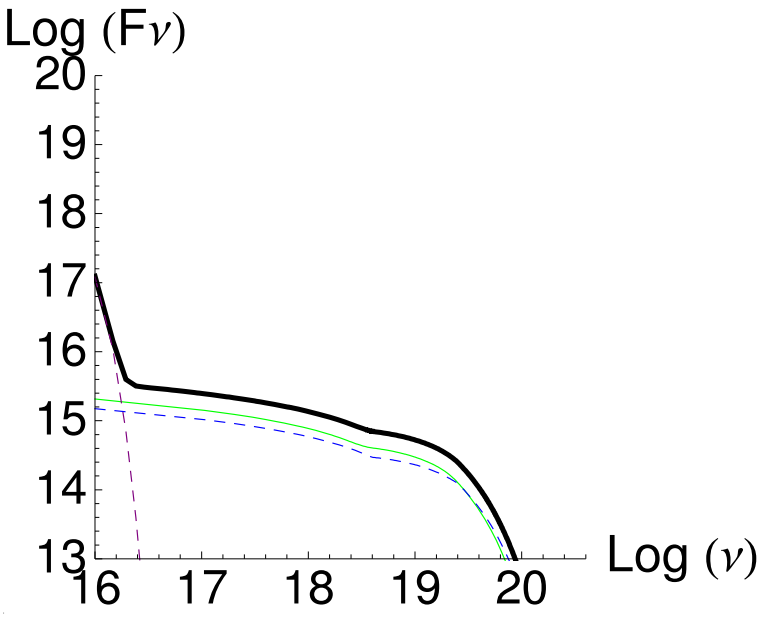

Figure 5.8: Spectrum in the EUV to X-ray range for a total supply rate of $m_s = 0.02$. This corresponds to the state labeled 2 on the HID shown on Fig. 5.11. The dashed curves represent the ADAF (blue) and outer disk (purple) contributions. Bremsstrahlung over the outer disk is depicted in the green curve. The uppermost curve is the sum.

inner ADAF. At this rate the inner radius of the outer accretion disk becomes $r_{\rm tr} \sim 148$. If the accretion rate is increased to 0.1, which we have defined above to be the rate of state transition, this inner hole disappears. The system is now in the thermal state and jumps to the left side of the figure. At this point, the bremsstrahlung emission from the radiative layer at the base of the corona reaches a constant, and that from the ADAF disappears. This indicates there is no steady-state solution within this radius, within the context of this model. The blackbody emission continues to rise in intensity and peaks in the lower X-ray band. Increasing the supply rate further will merely intensify the thermal emission, and push the system further to the left on the HID, in the context of this model. The corona will continue to exist above and below, and its energy content remains the same even as the supply rate is increased, because we have fixed the seed value. This corresponds to a saturated corona under the assumptions of the evaporation-condensation model. This was done in order to partially decouple the evolution of the disk beyond $r_{\rm out}$ from the inner disk

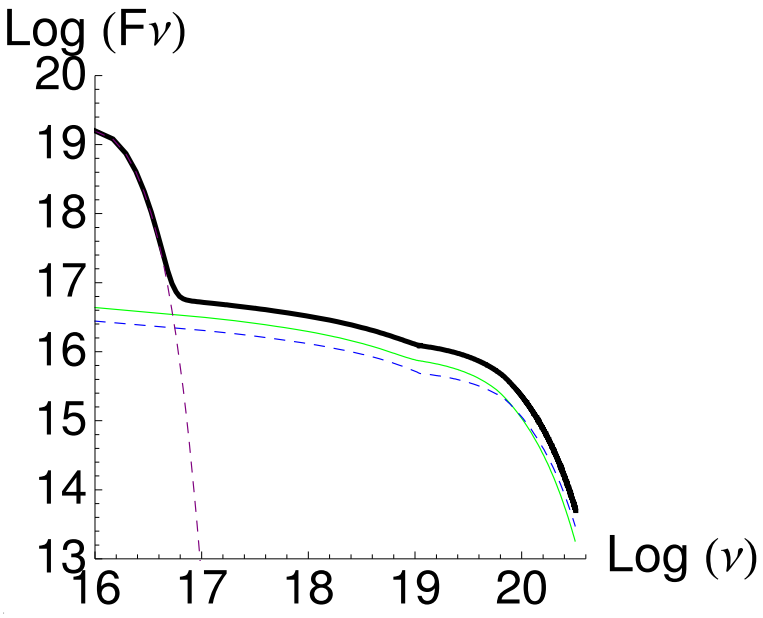

Figure 5.9: Spectrum in the EUV to X-ray range for a total supply rate of $m_s = 0.095$. This corresponds to the state labeled 3 on the HID shown on Fig. 5.11. The dashed curves represent the ADAF (dashed blue) and outer disk (purple) contributions.

considered here. The only coupling we are allowing is through the supply rate $\dot{m}_{\rm s}$. In reality, the seed value may well change as a system makes its transition from one state to another but to treat this would require the consideration of viscous evolution coupled to the physics of the corona and this is beyond the scope of the present treatment.

As the supply rate drops below the state transition rate, a disk gap forms first where the evaporation rate reaches a maximum (in this particular case, $r_{\rm evap,max} \sim 120$). The system is now in what we believe is the lower intermediate state, and we begin calculating emission from the ADAF again as it moves to the right in the HID. The outer and inner disks have coronae and radiative layers above and below, and the space between the two disks is an ADAF of increasing radial extent (as the supply rate falls). Dropping the supply rate further moves the truncation radius outwards, but the presence of an inner disk inside the gap allows significant recondensation to occur if the drop of the supply rate is not so rapid that the disk falls into the black hole. This means that the timescale for recondensation must be shorter

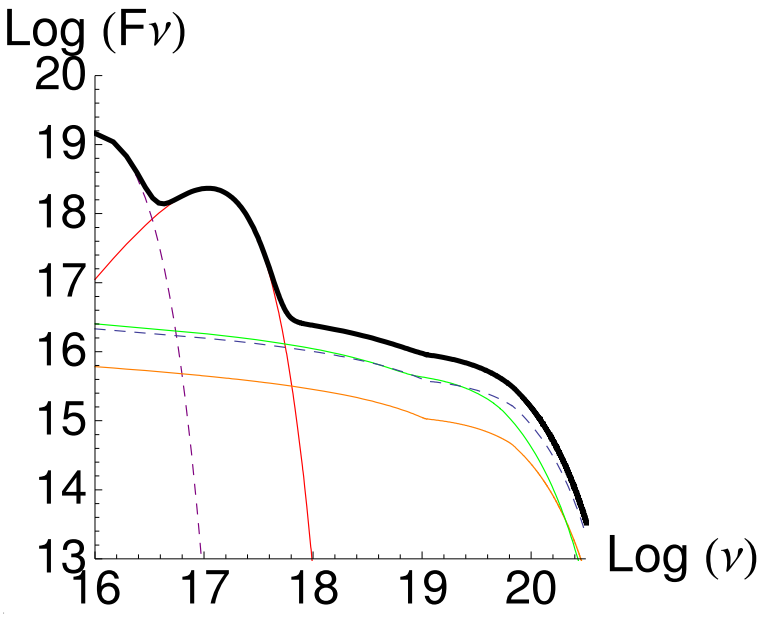

Figure 5.10: Bremsstrahlung spectrum over a truncated disk of accretion rate $m_s = 0.075$, in the X-ray range, along with emission from the ADAF itself (dashed). The upper bremsstrahlung spectral curve (green) is the outer disk, the lowest (orange) is that of the inner disk, with the dashed curve as the ADAF (blue) in between. The thickest solid curve is the sum of all components. Also plotted are the two components from blackbody emission above the outer (purple) and inner (red) disks. This corresponds to the intermediate state labeled 6 on the descending branch of the HID shown on Fig. 5.11.

than the viscous timescale of the inner disk. The condensation radius depends on the supply rate, and so it will continue to decrease until it reaches the ISCO, at which point there is only an outer disk remaining, with an ADAF extending radially from $r_{\rm tr}$ to the black hole. In Fig. 5.11 this disappearance of the inner disk occurs at $\dot{m}_{\rm s} \lesssim 0.05$, where the descending branch joins the near vertical branch of hard states at the point labeled 7.

Note that our model consists of a sequence of assumed steady states; there is no consideration of viscous timescales in this HID. Therefore accurate sampling of the upper intermediate state cannot be done, for example. We point out that there are other physical effects that go into the hard-thermal state transition that we have not included in this paper, e.g., the effects of bulk motion Comptonization (Titarchuk & Schrader, 2002) or inverse Comptoniza-

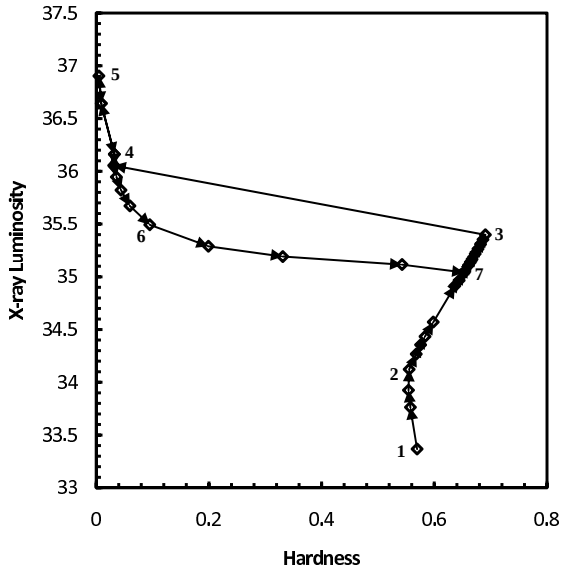

Figure 5.11: Hardness-Intensity diagram generated by this model. Intensity is defined as the total luminosity in the 1-60 keV range, depicted logarithmically. Hardness is defined as the luminosity in the 15-20 keV range divided by that in the 1-5 keV range. The supply rate at state transition is set to $\dot{m}_{\rm s} = 0.1$.

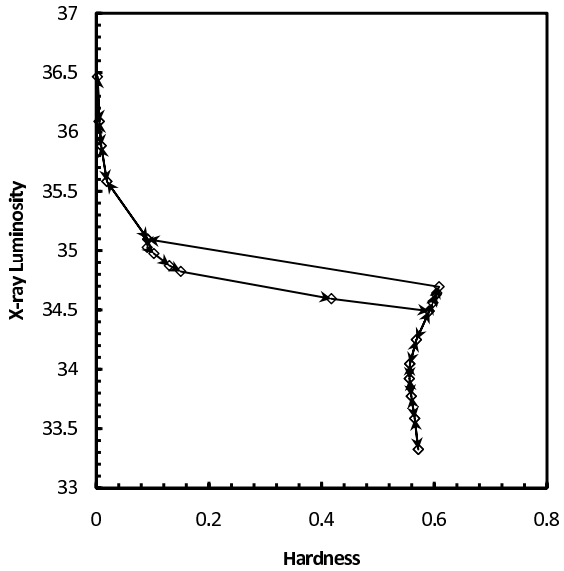

Figure 5.12: Same as Fig. 5.11 for a supply rate at state transition set to $\dot{m}_{\rm s} = 0.04$.

tion (Zdziarski & Gierlinski, 2004; Zdziarski et al., 2005), so this simple model should not be applied for this transition.

5.7 Conclusions

We have presented numerical calculations for a two-phase accretion flow around a black hole. We extend the one zone approximation of MLMH to all radii, and allow these radii to be coupled using the self-similar formulae and a variable accretion rate. Starting with a flow that is initially composed of a cool geometrically-thin but optically-thick disk, sandwiched by a hot, geometrically-thick and optically-thin corona assumed to behave as a self-similar ADAF, we show that the sandwich structure disappears at a certain radius. A gap develops in the disk structure due to evaporation, and the inner disk can persist until the accretion rate of the system drops low enough that condensation is no longer efficient and it is accreted. We then are left with an ADAF flow at inner radii and a sandwich flow outside. We calculate spectra from the various disk structures assuming the only radiation emitted is bremsstrahlung and blackbody emission from the corona/ADAF and disk respectively.

Another important question to be answered is the production of the corona. The model presented here, as well as those which it is based upon, begin with an assumption that the corona is already in place. How it initially came to be is unclear. In this work, once we start with a tiny corona and consider conduction, the corona is produced by the outer disk.

Throughout the course of this project, we have assumed that the specific angular momentum of the evaporating/condensing material at any radius remains constant, and this is likely our most questionable assumption. Mayer & Pringle (2007) argue that at most this assumption augments the results (which are conceptually similar to our own) by factors of unity. It will, however, be important to include these effects in future computations. Since the corona is geometrically thick, radial pressure gradients lead to a deviation from Keplerian rotation. The corona and the disk will rotate at different speeds. At their boundary, torques arise which lead to angular momentum exchange between the two phases (e.g., by

the poloidal component of the magnetic field in the disk that extends into the corona). The work done by these torques will lead to an additional heating of the corona, in particular the ions. Further momentum exchange will arise from the mass transfer due to thermal conduction as both layers rotate at different speeds. This could drive the overlying corona outwards, where it would influence the spectrum and could condense into the disk.

At low densities and high temperatures seen in ADAFs, Compton-cooling will become important over bremsstrahlung. In the canonical ADAF this is done by Comptonization of synchrotron photons (SSC) in the tangled magnetic field of the corona. If there is a relatively cool accretion disk below, however, cooling can proceed through inverse Compton scattering of the soft photons emitted by the disk and could become more useful in cooling the electrons in the corona than conduction. We have not considered the addition of irradiation of the outer disk by the inner regions. Although we believe the qualitative nature of the results will not change, the energy put into the outer disk would likely be significant enough to raise the temperatures and push the truncation radius outwards, while the Compton-cooling will move the condensation radii outwards.

Note that in our formulation, the cold thin disk underneath does not exchange energy with the overlying corona, only mass. It merely serves as a "cold conducting plate" that allows an electron temperature gradient to form, giving us vertical conduction, and as a mass reservoir (sink) for the evaporating (condensing) corona.

Finally, it is worth emphasizing that while the treatment presented here suffers from various shortcomings that have already been mentioned, we think it does show that in principle this mechanism, when augmented and improved by consideration of the viscous evolution, global Comptonization, and a more refined treatment of couplings between the vertical and radial flows, may account for the diversity of behavior observed in low-mass X-ray binaries.

Bibliography

Abramowicz, M.A., Kluźniak, W., 2001, A&ALett, 374, L19

Abramowicz, M.A., Czerny, B., Lasota, J.P., Szuskiewicz, E., 1988, ApJ, 332, 646

Abramowicz, M.A., Chen, X., Kato, S., Lasota, J.P., Regev, O., 1995, ApJ, 438L, 37

Abramowicz, M.A., Karas, V., Kluźniak, W., Lee, W.H., Rebusco, P., 2003,PASJ, 55, 467

Arai, K., Hashimoto, M., 1992, A&A, 254, 191

Arnaud, K.A., 1996, Astronomical Data Analysis Software and Systems V, eds. Jacoby G. and Barnes J., p17, ASP Conf. Series, vol. 101.

Balbus, S., Hawley, J., 1991, ApJ, 376, 214

Balbus, S., Hawley, J., 1998, RvMP, 70, 1

Barr, P., White, N.E., Page, C.G., 1985, MNRAS, 216, 65

Beckwith, K., Done, C., 2004, MNRAS, 352, 353

Begelman, M.C., Chiueh, T., 1988, ApJ, 332, 872

Belloni, T., 2004, NuPhS, 132, 337

Belloni, T., Mendez, M., van der Klis, M., Lewin, W., Dieters, S., 1999, ApJ, 519, 159

Belloni, T., Homan, J., Casella, P., van der Klis, M., Nespoli, E., et al. 2005, A&A, 440, 207

Belloni, T., Parolin, I., Del Santo, M, et al., 2006, MNRAS, 367, 1113

Blaauw, A., 1961, *Bulletin of the Astronomical Institutes of the Netherlands*, 15, 265

Blandford, R.D., Begelman, M.C., 1999, MNRAS, 303, L1

Blandford, R.D., Begelman, M.C., 2004, MNRAS, 349, 68

Blondin, J.M., Kallman, T.R., Fryxell, B.A., Taam, R.E., 1990, ApJ, 356, 591

Bolton, C.T., 1972, *Nature*, 235, 271

Bradley, C.K., Hynes, R.I., Kong, A.K.H., Haswell, C.A., et al., 2007, ApJ, 667, 427

Brown, G.E., Lee, C.H., Wijers, R.A.M., Lee, H.K., Israelian, G., Bethe, H.A., 2000, *New Astron*, 5, 191

Buxton, M.M., Bailyn, C.D., 2004, ApJ, 615, 880

Buxton, M.M., Gallo, E., Fender, R., Bailyn, C.D., 2004, ATel, 230

Campana, S., Stella, L., Belloni, T., Israel, G.L., Santangelo, A., Frontera, F., Orlandini, M., Dal Fiume, D., 2002, A&A, 384, 163

Cannizzo, J.K., Chen, W., Livio, M., 1995, ApJ, 454, 880

Cannizzo, J.K., Reiff, C.M., 1992, ApJ, 385, 87

Casares, J., Charles, P.A., Naylor, T., 1992, *Nature*, 355, 614

Casares, J., Charles, P.A., Naylor, T., Pavlenko, E.P., 1993, MNRAS, 365, 834

Casares, J., & Charles, P.A. 1994, MNRAS, 271, L5

Casares, J., Zurita, C., Shahbaz, T., Charles, P.A., Fender, R.P., 2004, ApJ, 613L, 133

Casella, P., Belloni, T., Stella, L., 2005, ApJ, 629, 403

Cash, W. 1979, ApJ, 228, 939

Chakrabarti, S.K., Manickam, S.G., 2000, ApJ, 531, L41

Chandrasekhar, S., 1960, PNAS, 46, 253

Chen, X., Abramowicz, M.A., Lasota, J.P., Narayan, R., Yi, I., 1995, ApJ, 443L 61

Chen, W., Shrader, C.R., Livio, M., 1997, ApJ, 491, 312

Churazov, E., Gilfanov, M., Forman, W., Jones, C., 1996, ApJ, 471, 673

Coe, M.J., Engel, A.R., Quenby, J.J., 1976, *Nature*, 259, 544

Coppi, P.S., 1999, ASPC, 161, 375

Corbel, S., Fender, R.P., Tzioumis, A.K., Tomsick, J.A., Orosz, J.A., Miller, J.M., Wijnands, R., Kaaret, P., 2003, NewAR, 47, 477

Corbel, S., Koerding, E., Kaaret, P., 2008, MNRAS, 389, 1697

Cowley, A.P., Crampton, D,, Hutchings, J.B., Remillard, R., Penfold, J.E., 1983,ApJ, 272, 118

Cui, W., Shrader, C.R., Haswell, C.A., Hynes, R.I., 2000, ApJ, 535, L123

Cui, W., Schulz, N.S., Baganoff, F.K., et al. 2001, ApJ, 548, 394

Davis, S.W., Blaes, O.M., Hubeny, I., Turner, N.J., 2005, ApJ, 621 372

Dermer, C.D., Liang, E.P., Canfield, E. 1991, ApJ, 369, 410

Dhawan, V., Mirabel, I. F., Rodrguez, L. F., 2000, ApJ, 543, 373

Done, C., Nayakshin, S., 2001,MNRAS, 328, 616

Done, C., Gierlinski, A.A., Kubota, A., 2007, A&ARv, 15, 1

Dovčiak, M., Karas, V., Yaqoob, T., 2004, ApJS, 153, 205

Dubus, G., Long, K.S., Charles, P.A., 1999, MNRAS, 519L, 135

Dubus, G., Hameury, J-M., Lasota, J-P., 2001, A&A, 373:251–71

Eggleton, P.P., 1983, ApJ, 268, 368

Elvis, M., Page, C. G., Pounds, K. A., Ricketts, M. J., Turner, M. J. L., 1975, *Nature*, 257, 656

Esin, A.A., 1997, ApJ, 482, 400

Esin, A.A., McClintock, J.E., Narayan, R., 1997, ApJ, 489, 865

Fabian, A.C., Rees, M. J., Stella, L., White, N. E., 1989, MNRAS, 238, 729

Fabian, A.C., Miniutti, G., 2005, in Wiltshire, D.L., Visser, M., Scott, S.M., eds, *Kerr Spacetime: Rotating Black Holes in General Relativity*, Cambridge University Press, Cambridge (astro-ph/0507409)

Fender, R.P., 2006, In *Compact Stellar X-ray Sources*, ed. W.H.G. Lewin, M. van der Klis, pp. 381–420. Cambridge: Cambridge University Press. (astro-ph/0303339).

Fender, R.P., Corbel, S., Tzioumis, T., McIntyre, V., Campbell-Wilson, D., et al., 1999, ApJ, 519, L165

Fender, R.P., Belloni, T., Gallo, E., 2004, MNRAS, 355, 1105

Flannery, B.P., van den Heuvel, E.P.J., 1975, A&A, 39, 61

Frank, J., King, A., Raine, D., 2002, *Accretion Power in Astrophysics* , Third Edition, Cambridge University Press, Cambridge UK

Frontera, F., Amati, L., Zdziarski, A.A., Belloni, T., Del Sordo, S., Masetti, N., Orlandini, M., Palazzi, E., 2003, ApJ, 592, 1110

Gallo, E., Fender, R.P., Pooley, G.G., 2003, MNRAS, 344, 60

Gallo, E., Corbel, S., Fender, R.P., Maccarone, T.J., Tzioumis, A.K., 2004, MNRAS, 347, 52

Gallo, E., Fender, R.P., Hynes, R.I., 2005, MNRAS, 356, 1017

Gallo, E., Fender, R.P., Miller-Jones, J.C., Merloni, A., Jonker, P.G., Heinz, S., Maccarone, T.J., van der Klis, M., 2006, MNRAS, 370, 1351

Garcia, M.R., Callanan, P.J., McClintock, J.E., Zhao, P., 1996, ApJ, 460, 932

Garcia, M.R., McClintock, J.E., Narayan, R., Callanan, P., Barret, D., & Murray, S.S., 2001, 553, L47

George, I.M., Fabian, A.C., 1991, MNRAS, 249, 352

Gierlinski, M., Newton, J., 2006, MNRAS, 370, 837

Gierlinski, M., Zdziarski, A.A., Done, C., Johnson, W.N., Ebisawa, K., Ueda, Y., Haardt, F., Phlips, B.F., 1997, MNRAS, 288, 958

Gorenstein, P., Gursky, H., Garmire, G. 1968, ApJ, 153, 885

Haardt, F., Maraschi, L., 1991, ApJ, 380L, 51

Haardt, F., Maraschi, L,, 1993, ApJ, 413, 507

Hawley, & J.F. Krolik, J.H. 2001, ApJ, 548, 348

Heinzeller, D., & Duschl, W.J., 2007, MNRAS, 374, 1146

Homan, J., Belloni, T., 2005, Ap & SS, 300, 107

Homan, J., Wijnands, R., van der Klis, M., Belloni, T., van Paradijs, J., Klein-Wolt, M., Fender, R.P., Mendez, M., 2001, ApJS, 132, 377

Homan, J., Klein–Wolt M., Rossi, S., Miller, J.M., Wijnands, R., Belloni, T., van der Klis, M., Lewin, W.H.G., 2003, ApJ, 586, 1262

Homan, J., Miller, J.M., Wijnands, R., Lewin, W.H.G., 2005a, *BAAS* 207, 1331

Homan, J., Buxton, M., Markoff, S., Bailyn, C.D., Nespoli, E., Belloni, T., 2005b, ApJ, 624, 295

House, L.L., 1969, ApJS, 18, 21

Hynes, R.I., Steeghs, D., Casares, J., Charles, P.A., O'Brien, K., 2003,ApJ, 583L, 95

Hynes, R.I., Charles, P.A., Garcia, M.R., et al., 2004, ApJL, 611L, 125

Hynes, R. I., Robinson, E. L., & Bitner, M. 2005, ApJ, 630, 405

Hynes, R.I., Bradley, C.K., Rupen, M., Gallo, E., et al., 2009, MNRASsubmitted

Ichimaru, S., 1997, ApJ, 214, 840

In't Zand, J.J.M., Markwardt, C.B., Bazzano, A., et al., 2002, A&A, 390, 597

Israelian, G., Rebolo, R., Basri, G. 1999, *Nature*, 401, 142

Jin, L., Arnett, W.D., Chakrabarti, S.K., 1989, ApJ, 336, 572

Kalemci, E., Tomsick, J.A., Rothschild, R.E., Pottschmidt, K, Kaaret, P., 2004, ApJ, 603, 231

Kalogera, V., Baym, G., 1996,ApJ, 470, L61

Karzas, W.J., Latter, R. 1961, ApJS, 6, 167

Kato, Y., 2004,PASJ, 56, 931

King, A., 1993, MNRAS, 260L, 5

King. A., 2003, *From X-ray Binaries to Gamma-Ray Bursts: Proceedings of the van Paradijs symposium*, ed. E.P. van den Heuvel, L. Kaper, E. Rol, R.A.M.J. Wijers, ASP Conf. Series, Vol. 308, (astro-ph/0108364)

King, A., Ritter, H., 1998, MNRAS, 293L, 42

Kippenhahn, R., Weigert, A., 1990, *Stellar Structure and Evolution*, Springer-Verlag, New York

Kluzniak, W., 2001, ApSSS, 276, 237

Kluzniak, W., Abramowicz, M.A., Lee, W.H., 2004, AIPC, 714, 379

Kong, A.K.H., Kuulkers, E., Charles, P.A., Homer, L., 2000, MNRAS, 312, 49

Kong, A.K., McClintock, J.E., Garcia, M.R., Murray, S.S., Barret, D., 2002, ApJ, 570, 277

Kubota, A., Makishima, K., 2004, ApJ, 601, 428

Kurucz, R.L., 1991, In: *Stellar Atmospheres: Beyond Classical Models, Proceedings of the Advanced Research Workshop*, NATO ASIC Proc., 341, 441, D. Reidel Publishing

Kuulkers, E., 1998, NewAR, 42, 1

Lasota, J-P., 2001, *New Astron Rev*, 45, 449

Laor, A., 1991,ApJ, 376, 90

Laurent, P., Titarchuk, L., 2001, ApJ, 562, 67

Li, L., Zimmerman, E.R., Narayan, R., McClintock, J.E., 2005, ApJS, 157, 335

Liu, B.F., Mineshige, S., Meyer, F., et al. 2002, ApJ, 575, 117

Liu, B.F., Meyer, F., & Meyer-Hofmeister, 2005, A&A, 442, 555

Liu, B.F., Meyer, F., & Meyer-Hofmeister, 2006, A&A, 454, 9L

Liu, B.F., Taam, R.E., Meyer-Hofmeister, E., Meyer, F., 2007, ApJ, 671, 695L

Leahy, D.A., Darbro, W,, Elsner, R.F., Weisskopf, M.C., Sutherland, P.G., Grindlay, J.E., 1983, ApJ, 266, 160

Lewin, W., van Paradijs, J., van den Heuvel, E.P.J., 1995, *X-ray Binaries*, Cambridge University Press, Cambridge UK

Lynden-Bell, D., Pringle, J.E., 1974, MNRAS, 168, 603

Maccarone, T.J., 2003, A&A, 409, 697

Makino, F., Wagner, R.M., Starrfield, S., Buie, M.W., Bond, H.E., Johnson, J., Harrison, T., Gehrz, R.D., 1989, IAUC, 4786

Makishima, K., 1986, LNP, 266, 249

Malzac, J., Belmont, R., 2008, *Proceedings of the VII Microquasar Workshop: Microquasars and Beyond*, ed. E. Kalemci, PoS (MQW7), (astro-ph/0810.4589)

Markert, T.H., Canizares, C.R., Clark, G.W., Lewin, W.H.G., Schnopper, H.W., Sprott, G.F., 1973, ApJ, 184L, 67

Markoff, S., Falcke, H., Fender, R.P., 2001, A&A, 372, 25

Markoff, S., Nowak, M., Corbel, S., Fender, R.P., Falcke, H., 2003, *New Astron Rev*, 47, 491

Martin, E.L., Rebolo, R., Casares, J., Charles, P.A., 1992, *Nature*, 358, 129

Martocchia, A., Matt, G., Karas, V., Belloni, T., Feroci, M., 2002, A&A, 387, 215

Martocchia, A., Matt, G., Belloni, T., Feroci, M., Karas, V., Ponti, G., 2006, A&A, 448, 677

Marsh, T.R., Robinson, E.L., Wood, J.H., 1994, MNRAS, 266, 137

Mayer, M., Pringle, J.E. 2007, MNRAS, 376, 435

McClintock, J.E., Remillard, R.A., 2006, In *Compact Stellar X-ray Sources*, ed. W.H.G. Lewin, M. van der Klis, p.157. Cambridge: Cambridge University Press.

McClintock, J.E., Horne, K., Remillard, R.A., 1995, ApJ, 442, 358

McClintock, J.E., Haswell, C.A., Garcia, M.R., Drake, J.J., Hynes, R.I., et al., 2001, ApJ555, 477

McKinney, J.C., Gammie, C.F., 2004, ApJ, 611, 977

Merloni, A., Vietri, M., Stella, L., Bini, D., 1999, MNRAS, 304, 155

Meyer, F., & Meyer-Hofmeister, E. 1994, A&A, 288, 175

Meyer-Hofmeister, E., & Meyer, F. 1999, A&A, 348, 154 739

Meyer-Hofmeister, E., & Meyer, F., 2006, A&A, 449, 443

Meyer, F., Liu, B.F., & Meyer-Hofmeister, E. 2000, A&A, 361, 175

Meyer, F., Liu, B.F., Meyer-Hofmeister, E., 2007, A&A, 463, 1

Meyer-Hofmeister, E., Liu, B.F., & Meyer, F. 2005, A&A, 432, 181

Miller, J.M., Fabian, A.C., Wijnands, R., et al., 2002, ApJ, 570, 69

Miller, J.M., Fabian, A.C., Reynolds, C.S., Nowak, M.A., Homan J, et al., 2004a, ApJ, 606: L131–34

Miller, J.M., Raymond, J., Fabian, A.C., Homan, J., et al., 2004b, ApJ, 601, 450

Miller, J.M., Fabian, A.C., Nowak, M.A., Lewin, W.H.G., 2005, *Proc. 10th Annual Marcel Grossman Meeting, General Relativity*, eds. M. Novello, S.P. Bergliaffa, R. Ruffini. Rio de Janeiro, Brazil. World Scientific Publishing, Singapore. p. 1296 (astro-ph/0402101)

Miller, J.M., 2006, Astron. Nachr., 327, 997

Miller-Jones, J.C.A., Gallo, E., Rupen, M.P., Mioduszewski, A.J., Brisken, W., Fender, R.P., Jonker, P.G., Maccarone, T.J., 2008, MNRAS, 388, 1751

Mirabel, I.F., Mignani, R., Rodrigues, I., Combi, J.A., Rodriguez,L.F., Guglielmetti, F., 2002, A&A, 395, 595

Mitsuda, K., Inoue, H., Koyama, K., Makishima, K., et al., 1984, PASJ, 36, 741

Miyamoto, S., Kimura, K., Kitamoto, S., Dotani, T., Ebisawa, K., 1991, ApJ, 383, 784

Miyamoto, S., Kitamoto, S., Iga, S., Hayashida, K., Terada, K., 1994, ApJ, 435, 398

Morgan, E.H., Remillard, R.A., Greiner, J., 1997,ApJ, 482, 993

Mukhopadhyay, B., Chakrabarti, S.K., 2000, MNRAS, 353, 1029

Muno, M. P., & Mauerhan, J. 2006, ApJL, 648, L135

Muno, M.P., Morgan, E.H., Remillard, R.A., 1999, ApJ, 527, 321

Muno, M.P., Remillard, R.A, Morgan, E.H., Waltman, E.B., Dhawan, V., Hjellming, R.M., Pooley, G., 2001,ApJ, 556, 515

Narayan, R., McClintock, J.E., 2008, NewAR, 51, 733

Narayan, R., Popham, R., 1993, *Nature*, 362, 820

Narayan, R., & Raymond, J. 1999, ApJ, 515L, 69

Narayan, R., Yi, I., 1994, ApJ, 428L, 13

Narayan, R., & Yi, I. 1995a, ApJ, 452, 710

Narayan, R., Yi, I., 1995b, ApJ, 444, 231

Narayan, R., Barret, D., & McClintock, J.E. 1997, ApJ, 482, 448

Narayan, R., Garcia, M.R., McClintock, J.E., 1997, ApJ, 478, 79

Narayan, R., Mahadevan, R., Quataert, E., 1998, In *Theory of Black Hole Accretion Disks*, ed. M.A. Abramowicz, G. Bjornsson, J.E. Pringle, p. 148. Cambridge: Cambridge University Press.

Narayan, R., Garcia, M., McClintock, J.E., 2002, in Gurzadyan V., Jantzen R., Ruffini R., eds, Proc. IX Marcel Grossmann Meeting. World Scientific, Singapore, 405

Nayakshin, S., Svensson, R., 2001, ApJ, 551L, 67

Nelemans, G., Tauris, T.M., van den Heuvel, E.P.J., 1999, A&A, 352L, 87

Nespoli, E., Belloni, T, Homan, J., Miller, J., Lewin, W.H.G., Mendez, M., van der Klis, M., 2003, A&A, 412, 235

Nobili, L., Turolla, R., Zampieri, L., Belloni, T., 2000, ApJ, 538, L137

Nowak, M.A., Wilms, J., Vaughan, B.A., Dove, J.B., Begelman, M.C., 1999, ApJ, 515, 726

Oosterbroek, T., Parmar, A.N., Sidoli, L., In't Zand, J.J.M., Heise, J., 2001, A&A, 376, 532

Orosz, J.A., 2003, Proc. IAU Symposium, 212, 365

Orosz, J.A., Kuulkers, E., van der Klis, M., McClintock, J.E., Garcia, M.R., et al., 2001, ApJ, 555, 489

Orosz, J.A., Groot, P.J., van der Klis, M., McClintock, J.E., et al. 2002, ApJ, 568, 845

Orosz, J.A., McClintock, J.E., Remillard, R.A., Corbel, S., 2004, ApJ, 616, 376

Osaki, Y., 1974, PASJ, 26, 429

Pacynski, B., 1971, ARA&A, 9, 183

Patterson, J., 1984, ApJS, 54, 443

Phinney, E.S., 1981, in *Plasma Astrophysics*, ed. T.D. Guyen & G. Levy, (ESA SP-161; Noordwijk:ESA), 337

Piran, T., 1978, ApJ, 221, 652

Pottschmidt, K., Chernyakova, M., Zdziarski, A.A., Lubinski, P., Smith, D.M., Bezayiff, N., 2006, A&A, 452, 285

Poutanen, J., Fabian, A.C., 1999, MNRAS, 306, 31

Pringle, J.E., 1981, Annu. Rev. Astron. Astrophys. , 19, 137

Psaltis, D., 2006, In *Compact Stellar X-ray Sources*, ed. W.H.G. Lewin, M. van der Klis, pp. 1–38. Cambridge: Cambridge University Press. (astro-ph/0410536).

Quataert, E., 1998, ApJ, 500, 978

Quataert, E., Gruzinov, A., 1999, ApJ, 520, 248

Raymond, J.C., Smith, B.W., 1977, ApJS, 35, 419

Rees, M.J., Phinney, E.S., Begelman, M.C., Blandford, R.D., 1982, *Nature*, 295, 17

Remillard, R.A., 2004, *AIPC*, 714, 13

Remillard, R.A., McClintock, J.E., 2006, ARA&A, 44, 49

Remillard, R.A., Morgan, E.H., McClintock, J.E., Bailyn, C.D., Orosz, J.A., 1999, ApJ, 522, 397

Remillard, R.A., Muno, M.P., McClintock, J.E., Orosz, J.A., 2002, ApJ, 580,1030

Revnivtsev, M., Sunyaev, R., Borozdin, K., 2000, A&A, 361L, 37

Reynolds, C.S., Nowak, M.A., 2003, *PhysRept*, 377, 389

Rodriguez, J., Durouchoux, P., Mirabel, I.F., Ueda, Y., Tagger, M., Yamaoka, K., 2002, A&A, 386, 271

Rodriguez, J., Hannikainen, D.C., Shaw, S.E., et al., 2008, ApJ, 675, 1436

Rossi, S., Homan, J., Miller, J.M., Belloni, T., 2004,*NuPhS*, 132, 416

Rothstein, D.M., Eikenberry, S.S., Matthews, K., 2005, ApJ, 626, 991

Różańska, A., & Czerny, B. 2000a, MNRAS, 316, 473

Różańska, A., & Czerny, B. 2000b, A&A, 360, 1170

Schnittman, J.D., Bertschinger, E., 2004, ApJ, 606, 1098

Shahbaz, T., Naylor, T., Charles, P.A., 1993, MNRAS, 265, 655

Shahbaz, T., Ringwald, F.A., Bunn, J.C., Naylor, T., Charles, P.A., Casares, J., 1994b, MNRAS, 271, L10

Shahbaz, T., Sansom, A.E., Naylor, T., Dotani, T., 1994a, MNRAS, 268, 763

Shahbaz, T., van der Hooft, F., Casares, J., Charles, P.A., van Paradijs, J., 1999, MNRAS, 306, 89

Shahbaz, T., Fender, R.P., Charles, P.A., 2001, A&A, 376L, 17

Shakura, N.I., Sunyaev, R.A., 1973, A&A, 24, 337

Shapiro, S.L., Teukolsky, S.A., 1983, *Black Holes White Dwarfs and Neutron Stars: The Physics of Compact Objects*. New York: Wiley. 645 pp.

Shapiro, S.L., Lightman, A.P., Eardley, D.M., 1976, ApJ, 204, 187

Smak, J., 1971, *Acta Astron*, 21, 15

Smith, D.M., Heindl, W.A., Markwardt, C.B., Swank, J.H. 2001, ApJ, 554L, 41

Smith. D.M., Heindl, W.A., Swank, J.H., 2002, ApJ, 569, 362

Sobczak, G.J., McClintock, J.E., Remillard, R.A., Cui, W., Levine, A.M., et al., 2000,ApJ, 531, 537

Spitzer, L., 1962, In *Physics of Fully Ionized Gases*, NY, Interscience, 2nd Ed.

Stepney, S., Guilbert, P.W. 1983, MNRAS, 204, 1269

Stirling, A.M., Spencer, R.E., de la Force, C.J., Garrett, M.A., Fender, R.P., Ogley, R.N., 2001,MNRAS, 327, 1273

Strohmayer, T.E. 2001b, ApJ, 554, L169

Sutherland, R.S., Dopita, M.A. 1993, ApJS, 88, 253

Taam, R., Liu, B.F., Meyer, F., Meyer-Hofmeister, E. 2008, ApJ, 688, 527

Tagger, M., Pellat, R., 1999, A&A, 349, 1003

Tanaka, Y., Nandra, K., Fabian, A.C., et al., 1995, *Nature*, 375, 659

Tananbaum, H., Gursky, H., Kellogg, E., Giacconi, R., Jones, C., 1972, ApJ, 177L, 5

Tauris, T.M., van den Heuvel, E.P.J., 2003, In *Compact Stellar X-ray Sources*, ed. W.H.G. Lewin, M. van der Klis, p.46. Cambridge: Cambridge University Press. (astro-ph/0303456).

Theiling, M.F., Leising, M.D., 2006, *New Astron Rev*, 50, 544

Titarchuk, L., Osherovich, V., 2000, ApJ, 542, 111

Titarchuk, L., Shrader, C.R., 2002, ApJ, 567, 1057

Tomsick, J.A., Kaaret, P., 2001., ApJ, 548, 401

Tomsick, J.A., Kalemci, E., Kaaret, P. et al. 2008, ApJ, 680, 593

Tucker, W. 1975, In *Radiation processes in astrophysics*, MIT Press.

van Paradijs, J., 1996, ApJ, 464L, 139

Vaughan, B.A., Nowak, M.A., 1997, ApJ, 474, L43

Velikhov, E., 1959, Sov. Phys. JETP, 36, 995

Wade, R.A., & Horne, K., 1988, ApJ, 324, 411

Wagner, R.M., Howell, S.B., Kreidl, T.J., Starrfield, S.G., 1992, AAS, 180, 2801

Wandel, A., Liang, E.P., 1991, ApJ, 380, 84

Wandel, A., Urry, C.M., 1991, ApJ, 367, 78

Weaver, K.A., Yaqoob, T., Mushotsky, R.F., et al., 1996, AAS, 188, 1601

Webster, B.L., Murdin, P., 1972, *Nature*, 235, 37

White, N.E., Nagase, F., Parmar, A.N., In *X-ray Binaries*, ed. W.H.G. Lewin, J. van Paradijs, & E.P.J. van den Heuvel. Cambridge: Cambridge Univ. Press. p. 1

Witt, H.J., Czerny, B., Zycki, P.T., 1997, MNRAS, 286, 848

Woosley, S.E., Heger, A., Weaver, T.A., 2002, *RvMP*, 74, 1015

Yaqoob, T., George, I.M., Kallman, T.R., et al., 2003, ApJ, 596, 85

Yi, I., Narayan, R., 1997, ApJ, 486, 363

Young, A.J., Ross, R.R, Fabian, A.C., 1998, MNRAS, 300, 11

Yuan, F. 2001, MNRAS, 324, 119

Yuan, F., & Narayan, R. 2004, ApJ, 612, 724

Yuan, F., Cui, W., Narayan, R., 2005, ApJ, 620, 905

Zdziarski, A.A., & Gierlinski, M. 2004, Prog. Theor. Phys. Suppl., 155, 99

Zdziarski, A.A., Poutanen, J., Paciesas, W.S., Wen, L., 2002, ApJ, 578, 357

Zdziarski, A.A., Gierliński, M., Mikolajewska, J. et al. 2004, MNRAS, 351, 791

Zdziarski, A.A., Gierliński, M., Rao, A.R., et al., 2005, MNRAS, 360, 825

Zel'dovich, Y.B., Novikov, I.D. 1964, Dokl. Akad. Nauk. SSR, 158, 811; english translation 1965 Sov. Phys. Dokl., 9, 834

Zhang, S.N., Cui, W., Harmon, B.A., et al., 1997, ApJ, 477L, 95

Zycki, P.T., Done, C., Smith, D.A., 1998, ApJ, 496, 25

A. Appendix A: Derivations

A.1 Density

For the chemical abundance, hydrogen and helium mass fractions used are $X = 0.75$ and $Y = 0.25$. This leads to the relations between number density of protons and alpha particles with mass:

$$n_p = \frac{X\rho}{m_p} \tag{A.1}$$

$$n_\alpha = \frac{(1-X)\rho}{4m_p} \tag{A.2}$$

for the number densities of ions and electrons,

$$n_i = n_p + n_\alpha = \frac{1+3X}{4m_p}\rho \tag{A.3}$$

$$n_e = n_p + 2n_\alpha = \frac{1+X}{2m_p}\rho \tag{A.4}$$

giving a relation between ion and electron number density

$$n_i = \frac{n_e}{1.0769}. \tag{A.5}$$

A.2 Stability of the Two-Temperature Fluid Flow

In this section we investigate and discuss the stability of our two-temperature flow under the condition of constant surface density within a single radial zone. Any mass that flows out of this zone is assumed to flow inwards from the next outer zone.

We begin with the ion equation (Eq. 5.19) and define the net heating, including the compressive work:

$$q_i^+ = \frac{2-\beta}{1-\beta}\frac{9}{4}\alpha P_i \Omega \tag{A.6}$$

and the ions are cooled by Coulomb coupling to electrons. We have chosen to take a more complete form for the discussion here than in Eq. 5.16 (in which the ion temperature is assumed to be much greater than electrons).

$$q_{ie} = A_{ei} n_e n_i (T_i - T_e) \left(\frac{kT_e}{m_e c^2} \right)^{-3/2} \tag{A.7}$$

where $A_{ei} = 3.59 \times 10^{-32} \mathrm{gcm^5 s^{-3} deg^{-1}}$ as before.

In Section 5.2.3, Eq. 5.20 is the solution to the balance of the two equations above, using ADAF values for pressure, density, and virial temperature of the ions. Here, however, we will make the ion equation dimensionless first by dividing through by q^+_{ADAF} (Eq. A.6 using ADAF values). First, we look at the RHS:

$$\frac{q_i^+ - q_{ie}}{q^+_{i,ADAF}} = \frac{n_i T_i}{n_i^{ADAF} T_{\rm vir}} - \left(\frac{n_i}{n_i^{ADAF}} \right)^2 \left(\frac{T_i}{T_{\rm vir}} - \frac{T_e}{T_{\rm cpl}} \right) \left(1 - \frac{T_{\rm cpl}}{T_{\rm vir}} \right)^{-1} \left(\frac{T_e}{T_{\rm cpl}} \right)^{3/2} \tag{A.8}$$

Using the supposition that $\Sigma = n_i H = n_i T_i^{1/2} = const$, we also define $y = T_i/T_{\rm vir}$, $x = T_e/T_{\rm vir}$, and $e = T_{\rm cpl}/T_{\rm vir}$ as dimensionless constants. After some minor manipulation the result is:

$$\frac{q_i^+ - q_{ie}}{q^+_{i,ADAF}} = y^{1/2} - \frac{1}{y} \frac{y - x}{1 - e} \left(\frac{e}{x} \right)^{3/2} \tag{A.9}$$

The LHS, given that we use q defined as an energy loss or gain rate per unit volume, is a derivative of the ion pressure. We again suppose that Σ is a constant, and divide by the heating in the ADAF, then use the dimensionless scalings given above.

$$\frac{1}{q^+_{i,ADAF}} \frac{d}{dt} (n_i k_b T_i) = \frac{1 - \beta}{2 - \beta} \frac{4}{9\alpha} \frac{y^{-1/2}}{2\Omega_K} \frac{dy}{dt} \tag{A.10}$$

We then combine Ω_K into dt, making the variable of integration $d\tau$.

The full ion equation then becomes:

$$\frac{dy}{d\tau} = C^{-1} \left(y - \frac{y - x}{y^{1/2}(1 - e)} (\frac{e}{x})^{3/2} \right) \tag{A.11}$$

where the constant is

$$C = \frac{1 - \beta}{2 - \beta} \frac{2}{9\alpha} \tag{A.12}$$

For the electron equation, we consider their cooling to be from electron thermal conduction, and approximate the derivative in Eq. 5.21, assuming that $z_{\rm cpl}$ remains small compared to the scaleheight of the disk:

$$\frac{dF_{\rm c}}{dz} = \frac{F_{\rm c}}{z_{\rm m} - z_{\rm cpl}} = \frac{\kappa_0 T_e^{5/2}(T_e - T_{\rm cpl})}{z_{\rm m}^2} = 22863.71 r^{-3/2} \dot{m}_{\rm ADAF}^{-1} x^{5/2}(x - e) \tag{A.13}$$

and proceed as before, using the definitions above the result for the electrons

$$\frac{dx}{d\tau} = (1.077C)^{-1} \left(\left(\frac{e}{yx} \frac{y - x}{1 - e} \right) - 22863.71 x^3 \left(\frac{x - e}{e^{1/2}} \right) r^{-3/2} \dot{m}_{\rm ADAF}^{-1} \right) \tag{A.14}$$

To study the behavior of these two equations, we set both initial values for $x = x_0 = e$ and $y = y_0 = e = 0.001$, choose a characteristic radius and integrate with respect to τ. We limit the maximum value for the ion temperature to be that of virial ($y = 1$).

Integration shows, that given any reasonable value for $\dot{m}_{\rm ADAF}$, α, β and within the radii studied in this paper, that the ion and electron temperature always quickly diverge. At large radii, the electron temperature reaches a higher fraction of the virial temperature because of the different radial dependence, similar to the difference between $T_{\rm vir}$ and $T_{\rm m}$, and as we proceed inwards closer to the black hole, the difference becomes larger.

We then took the values of $T_{\rm vir}$, $\dot{m}_{\rm ADAF}$, and $T_{\rm cpl}$ from our integrations in the paper and studied the behavior of x with varying radii and compared it to $T_{\rm m}$ and find agreement with the numerical values of around 15 % between the two. This difference owes to the different formulation of the derivative we take for thermal conduction. Figures A.1-A.3 display the results of our integrations.

A.3 Energy Balance in Radiating Layer

We derive the condition for the different cases from the energy balance in the radiating layer based on MLMH. We use a simplified form of the energy equation, keeping only the dominant contribution of internal heat, pressure work, and thermal conduction, together

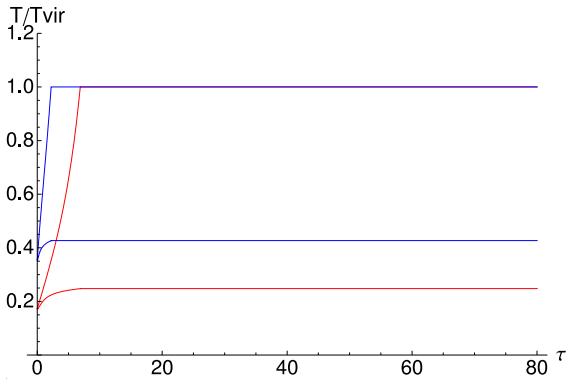

Figure A.1: Plot of the ion and electron temperatures against the variable of integration τ, for radii of 100 (red) and 1000 $R_{\rm S}$ (blue). Both temperatures are given the initial value of e from the actual integration in the paper, and then allowed to evolve. One sees that the ion and electron temperatures immediately diverge, with the ion temperature limited to a value of $y = 1.0$. The divergence is faster for the larger radius. The electron temperature is not limited directly but evolves to a value $\sim T_{\rm m}$ on its own within a fixed radius and using the correct value of $\dot{m}_{\rm ADAF}$ for that radius. Figures are calculated assuming a maximum total accretion rate of $\dot{m}_{\rm s} = 0.1$, where $\dot{m}_0 = 0.0092$.

with bremsstrahlung cooling $n_e n_i \Lambda(T)$,

$$\frac{d}{dz}\left[\dot{m}_z \frac{\gamma}{\gamma-1}\frac{\Re T}{\mu} + F_c\right] = -n_e n_i \Lambda(T). \tag{A.15}$$

We express density by temperature and (constant) gas pressure $\beta\, p$. This value is taken at the bottom of the ADAF region, and, as for the density, is slightly higher than the vertical mean pressure.

Assuming free-free radiation for $T_e \geq 10^{7.5}$K, $n_e n_i \Lambda(T)$ becomes $\frac{0.25}{k^2}(\beta\, p)^2 b T^{-3/2}$ with $b = 10^{-26.56}$g cm^{5}s^{-3}deg$^{-1/2}$ (Sutherland & Dopita 1993). For simplicity we use this law also for smaller T. The justification is that because of the very steep temperature profile below $10^{7.5}$K such regions contribute only a negligible amount to cooling of this layer (Liu et al. 1995). Contributions of gravitational energy release, frictional heating, and side-wise advection of mass and energy can be neglected for a small extent of this layer. Likewise, kinetic energy is negligible since at high density the flow is highly subsonic.

To solve the second-order differential equation Eq.(A.15), we use T as the independent variable and define a new dependent variable $g(T) \equiv \kappa_0 T^{3/2} dT/dz = -F_c/T$. We now obtain

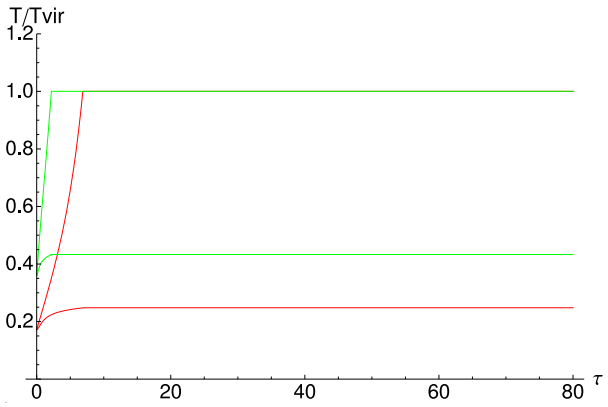

Figure A.2: Plot of the ion and electron temperatures against the variable of integration τ, for radii of 100 (red) and 300 $R_{\rm S}$ (green). Both temperatures are given the initial value of e from the actual integration in the paper, and then allowed to evolve. One sees that the ion and electron temperatures immediately diverge, with the ion temperature limited to a value of $y = 1.0$. The divergence is faster for the larger radius. The electron temperature is not limited directly but evolves to a value $\sim T_{\rm m}$ on its own within a fixed radius and using the correct value of $\dot{m}_{\rm ADAF}$ for that radius. Figures are calculated assuming a maximum total accretion rate of $\dot{m}_{\rm s} = 0.1$, where $\dot{m}_0 = 0.0092$.

the first-order differential equation

$$\begin{aligned} g\frac{dg}{d\ln T} &= \frac{0.25\beta^2 p^2}{k^2}\kappa_0 b + \dot{m}_z \frac{\gamma}{\gamma-1}\frac{\Re}{\mu} g - g^2 \\ &= -(g-g_1)(g-g_2), \end{aligned} \tag{A.16}$$

with

$$g_1 = \frac{\dot{m}_z}{2}\frac{\gamma}{\gamma-1}\frac{\Re}{\mu} + \sqrt{\left(\frac{\dot{m}_z}{2}\frac{\gamma}{\gamma-1}\frac{\Re}{\mu}\right)^2 + \frac{0.25\beta^2 p^2}{k^2}\kappa_0 b} \tag{A.17}$$

and g_2 differing from g_1 only by the sign of the square root.

This equation has to be solved with the upper and lower boundary conditions $g = \frac{-F_{\rm cpl}}{T_{\rm cpl}}$ at $T = T_{\rm cpl}$ and $F_{\rm c} = 0$ at $T = 0$. In reality, the temperature does not drop to zero at the disk surface but the solution is practically independent of the exact values at the lower boundary (except for a very narrow range in z at the bottom) as long as flux and temperature there become small compared to those at the upper boundary, with no consequence for our results. $\dot{m}_z$ is the Eigenvalue to be determined.

The only solution that fulfills the lower boundary condition is the singular solution $g(T) =$

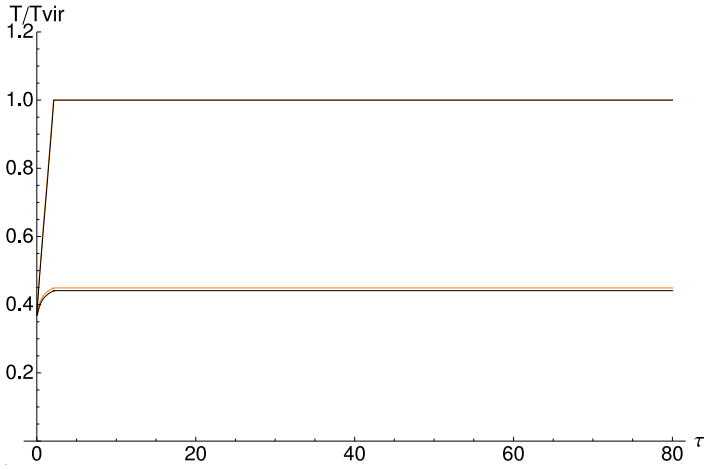

Figure A.3: Plot of the ion and electron temperatures against the variable of integration τ, for radii of 500 (orange) and 700 $R_{\rm S}$ (black). Both temperatures are given the initial value of e from the actual integration in the paper, and then allowed to evolve. One sees that the ion and electron temperatures immediately diverge, with the ion temperature limited to a value of $y = 1.0$. The divergence is faster for the larger radius, but the ion temperatures overlap in this case. The electron temperature is not limited directly but evolves to a value $\sim T_{\rm m}$ on its own within a fixed radius and using the correct value of $\dot{m}_{\rm ADAF}$ for that radius. Figures are calculated assuming a maximum total accretion rate of $\dot{m}_{\rm s} = 0.1$, where $\dot{m}_0 = 0.0092$.

$g_1 = const$, i.e. a linear relation between $-F_c$ and T. The ratio of these two quantities at the upper boundary determines the value of g_1. This requires

$$\dot{m}_z = \frac{\gamma - 1}{\gamma} \frac{-F_{\rm c}^{\rm ADAF}\left(1 - \frac{\dot{m}_z}{\dot{m}_z^*}\right)}{\frac{\Re T_{\rm cpl}}{\mu}} \left[1 - C\frac{1}{1 - (\frac{\dot{m}_z}{\dot{m}_z^*})^2}\right] \tag{A.18}$$

$$C = \kappa_0 b \left(\frac{0.25\beta^2 p^2}{k^2}\right) \left(\frac{T_{\rm cpl}}{F_c^{\rm ADAF}}\right)^2 . \tag{A.19}$$

Eqs.(A.18) and (5.28) yield a quadratic equation for $\dot{m}_z$,

$$\left(1 - \frac{\dot{m}_z}{\dot{m}_z^*}\right)^2 - \epsilon\left(1 - \frac{\dot{m}_z}{\dot{m}_z^*}\right) - (1 - \epsilon)C = 0\,, \tag{A.20}$$

with the solution

$$\frac{\dot{m}_z}{\dot{m}_z^*} = 1 - \frac{\epsilon}{2} - \sqrt{\frac{\epsilon 2}{4} + (1 - \epsilon)C}\,. \tag{A.21}$$

The quantity C of Eq.(A.19) compares the radiation loss in the thermal profile with the heat flux drained from the ADAF. For $C = 1$ Eq.(A.18) gives $m_z = 0$, the borderline case

discussed by Liu et al. (2006). For $C < 1$, the radiation losses are too weak, $\dot{m}_z$ is positive and the heat flow is used up to heat the evaporating gas to the (un-)coupling boundary temperature $T_{\rm cpl}$. If, on the other hand, $C > 1$, the gas in this layer is efficiently cooled, sinks down and condenses.

B. Appendix B: Equations

B.1 Derivation of Adiabatic Exponent

The following derivation is reproduced from Esin (1997) and is included for completeness.

One of the conditions that the physical parameters of the accretion flow must satisfy is the conservation of energy. Following Abramowicz et al. (1988) and Narayan & Yi (1994) we can write this condition as

$$\rho v T \frac{ds}{dR} = f q^+, \tag{B.1}$$

where s is the entropy per unit mass of the gas and other quantities are defined in §2.1.

To derive the expression for ds/dR we model the gas in the accreting flow as a combination of an ideal monatomic gas (a justified assumption since the accretion flow consists mainly of ionized hydrogen) and tangled magnetic fields. Radiation pressure was shown to be unimportant in one-temperature flows and since two-temperature solutions are even less luminous, the radiation pressure can safely be ignored. Then the total pressure in the gas is the sum of the thermal ideal gas pressure, and the pressure due to the magnetic field

$$p = p_g + p_m = \frac{\rho k T}{\mu m_u} + \frac{B^2}{24\pi} = \frac{\rho k T}{\beta \mu m_u}, \tag{B.2}$$

where we have defined $T = T_i$, $\mu = \mu_i \mu_e / (\mu_e + \mu_i T_e / T_i)$ and $\beta = p_g / p$. In general, μ is a function of both T_i and T_e; however, for simplicity we restrict ourselves to the two limiting cases when $T_i \gg T_e$ and $\mu = \mu_i$, or $T_i = T_e$ and $\mu = \mu_i \mu_e / (\mu_e + \mu_i)$.

The internal energy of the gas is the sum of the kinetic energy of the particles (since the gas is assumed to be monatomic) and the energy stored in the magnetic field. The total internal energy per unit mass is then

$$u = \frac{3}{2} \frac{kT}{\mu m_u} + \frac{1}{\rho} \frac{B^2}{8\pi} = \frac{3}{2} \frac{kT}{\mu m_u} + \frac{3(1-\beta)}{\beta} \frac{kT}{\mu m_u} = \frac{(6-3\beta)}{2\beta} \frac{kT}{\mu m_u} \tag{B.3}$$

In a quasistatic process, the first law of thermodynamics requires that

$$T ds = du + p\, dV = \left(\frac{\partial u}{\partial T}\right)_V dT + \left(\frac{\partial u}{\partial V}\right)_T dV + p\, dV, \tag{B.4}$$

where $V = 1/\rho$ is the volume per unit mass. But u is a function of T only, which means that the first term vanishes, $(\partial u/\partial V)_T = 0$. The second term we evaluate as

$$\left(\frac{\partial u}{\partial T}\right)_V = \frac{du}{dT} = \frac{(6-3\beta)}{2\beta}\frac{k}{\mu m_u}. \tag{B.5}$$

Finally, we divide both sides of Eq. (B.4) by T and obtain the following relation for the entropy

$$ds = \frac{(6-3\beta)}{2\beta}\frac{k}{\mu m_u}\frac{dT}{T} + \frac{\rho k}{\beta \mu m_u} d\left(\frac{1}{\rho}\right). \tag{B.6}$$

For an adiabatic process we set $ds = 0$. Following Clayton (1983, Eq. [2-121c]) we define the corresponding adiabatic exponent γ as

$$\gamma = \Gamma_3 = \frac{\left(\frac{1}{\beta}\frac{k}{\mu m_u}\right)}{\left(\frac{(6-3\beta)}{2\beta}\frac{k}{\mu m_u}\right)} + 1 = \frac{8-3\beta}{6-3\beta} \tag{B.7}$$

With this definition, we integrate Eq. (B.6) to obtain an expression for the entropy of the gas up to a constant factor:

$$s = \frac{k}{\beta \mu m_u}\frac{1}{\gamma - 1}\ln\left(c_s^2 \rho^{1-\gamma}\right) + \text{const.} \tag{B.8}$$

Now we are in a position to write down the final form for the energy conservation equation. Evaluating the derivative of s with respect to R and substituting it into Eq. (B.1), yields the same expression as given by Narayan & Yi (1994)

$$\frac{\rho v}{\beta(\gamma-1)}\frac{dc_s^2}{dR} - v c_s^2 \frac{d\rho}{dR} = f q^+, \tag{B.9}$$

but with a different value for γ, namely Eq. (B.7).

C. Appendix C: Permission to Reproduce Figures 2.1, 2.3, and 2.4

Hello,

I am a graduate student at the Louisiana State University Physics & Astronomy Department, and I would like to ask your permission to include a figure from one of your publications in my Dissertation titled, "Studies of States and State Transitions in Low Mass X-ray Binaries." The figures in question are Fig. 2 of Remillard & McClintock (2006, ARA&A) showing the spectra of GRO 1655-40 in the different states outlined in the paper. And the figure (fig. 1) displaying the many different systems observed in the galaxy, along with the figure on disk-jet coupling.

I would greatly appreciate your granting me the permission to include these illustrative figures of the PDS and spectra seen in the 3 states you outlined in your work, and the example of the different systems and hysteresis. It would greatly help the narrative.

Thanks, Charles Bradley

from: Ron Remillard rr@space.mit.edu

to: cbrad11@tigers.lsu.edu

date: Tue, Apr 28, 2009 at 2:01 PM

subject: Figure use request

Dear Charles,

Yes, I am very happy to grant you permission to include any figure from our paper in ARAA (2006, vol. 44, 49).

Best of luck finishing your thesis, and I am interested to learn of your conclusions when you are finished.

cheers, Ron Remillard

D. Appendix D: Permission to Reproduce Figure 2.2

from: Erik Kuulkers, Erik.Kuulkers@sciops.esa.int

to: Charles Bradley, cbrad11@tigers.lsu.edu

date: Thu, Apr 30, 2009 at 3:04 AM

subject:Re: Figure use request

Dear Charles,

Yes, you may use it if you want. I may even have the original data/files or plot, if you want. Also, if possible a copy or link to your thesis would be nice. Who's your supervisor; is it Rob Hynes?

Best regards,

Erik Kuulkers

E. Appendix E: Permission to Reproduce Figure 2.5

from: Jeroen Homan, jeroen@space.mit.edu to: Charles Bradley, cbrad11@tigers.lsu.edu date: Tue, Apr 28, 2009 at 4:06 PM subject: Re: Figure use request mailed-by: space.mit.edu

Hi Charles, Sure, no problem, as long as you provide the proper reference of course :) In case you don't have the figure yet, I'm attaching it for you. Just out of curiosity, what kind of work are you doing on state transitions? Cheers, Jeroen

On Apr 28, 2009, at 3:15 PM, Charles Bradley wrote:

Hello, I am a graduate student at the Louisiana State University Physics & Astronomy Department, and I would like to ask your permission to include a figure from one of your publications in my Dissertation titled, "States and State Transitions in Low Mass X-ray Binaries." The figure in question is Fig. 3 from Homan & Belloni (Ap&SS 2005) that shows examples of the PDS of GX339-4 in 4 different accretion states.

I would greatly appreciate your granting me the permission to include this illustrative figure of the PDS in the observed states outlined in the text of this paper, it would greatly help my narrative.

Thanks, Charles Bradley

F. Appendix F: Permission to Reproduce Figure 2.6

from Jon M Miller jonmm@umich.edu to Charles Bradley cbrad11@tigers.lsu.edu date Tue, Apr 28, 2009 at 2:40 PM subject Re: Figure use request

Hi Charles, Please be my guest. Congratulations on finishing your degree. Cheers, Jon

G. Appendix G: Permission to Reproduce Figure 2.7

from Andy Fabian, acf@ast.cam.ac.uk to Charles Bradley, cbrad11@tigers.lsu.edu date Wed, Apr 29, 2009 at 2:31 PM subject Re: Figure use request

Hi No problem. Please use the figure. yours Andy Fabian

H. Appendix H: Permission to Reproduce Figure 2.8

from Tomaso M Belloni,tomaso.belloni@brera.inaf.it

to Charles Bradley, cbrad11@tigers.lsu.edu

date Tue, Apr 28, 2009 at 3:42 PM

subject Re: Figure use request

Hi. Absolutely! No problem to use that figure. Tomaso

On 28 Apr 2009, at 21:08, Charles Bradley wrote:

Hello, I am a graduate student at the Louisiana State University Physics & Astronomy Department, and I would like to ask your permission to include a figure from one of your publications in my Dissertation titled, "States and State Transitions in Low Mass X-ray Binaries." The figure in question is Fig. 2 from Belloni et al. (A&A, 2005) that shows the hysteresis evolution of GX 339-4 for its 02/03 outburst.

I would greatly appreciate your granting me the permission to include this illustrative figure of the hysteresis. It would greatly help the narrative to have such a good example figure.

Thanks Charles Bradley

I. Appendix I: Letter of Permission

The following information is reproduced from the Institute of Physics website pertaining to the reproduction of material in Chapter 3 of this dissertation, of which I am the first and principal author. It confirms that I have permission to reproduce the contents of the article Bradley et al. (2007), as it is cited in the text.

Before your article can be published in an American Astronomical Society (AAS) journal, we require you to grant and assign the entire copyright in it to the AAS. The copyright consists of all rights protected by the copyright laws of the United States and of all foreign countries, in all languages and forms of communication, including the right to furnish the article or the abstracts to abstracting and indexing services, and the right to republish the entire article in any format or medium. *In return, the AAS grants to you the non-exclusive right of republication, subject only to your giving appropriate credit to the journal in which your article is published.* This non-exclusive right of republication includes your right to allow reproduction of parts of your article wherever you wish, and permits you to post the published (PDF) version of your article on your personal web site. To protect the copyright in your article, the original copyright notice as it appears in the journal should be included in the credit. To ensure the long-term access of the research community to its archives, the AAS holds the copyright on all copyrightable materials published in its journals, but the Society grants control of the right to reproduce the material to the original authors as long as they are alive. (http://www.iop.org/EJ/journal/-page=extra.3/APJ)

Vita

Charles Bradley was born in Spartanburg, South Carolina, in December 1980. He earned his bachelor's degree in physics and astronomy from Clemson University in May 2003. In August of that year, he enrolled at Louisiana State University. He received his master's degree in 2007, and expects to receive his doctoral degree in August 2009.